



Michigan Technological University  
*Create the Future* Digital Commons @ Michigan Tech

---

Dissertations, Master's Theses and Master's  
Reports - Open

Dissertations, Master's Theses and Master's  
Reports

---

2013

## DYNAMIC MODEL BASED STATE ESTIMATION IN A HEAVY DUTY DIESEL AFTERTREATMENT SYSTEM FOR ONBOARD DIAGNOSTICS AND CONTROLS

Harsha S. Surenahalli  
*Michigan Technological University*

Follow this and additional works at: <https://digitalcommons.mtu.edu/etds>



Part of the [Mechanical Engineering Commons](#)

Copyright 2013 Harsha S. Surenahalli

---

### Recommended Citation

Surenahalli, Harsha S., "DYNAMIC MODEL BASED STATE ESTIMATION IN A HEAVY DUTY DIESEL AFTERTREATMENT SYSTEM FOR ONBOARD DIAGNOSTICS AND CONTROLS", Dissertation, Michigan Technological University, 2013.  
<https://doi.org/10.37099/mtu.dc.etds/632>

Follow this and additional works at: <https://digitalcommons.mtu.edu/etds>



Part of the [Mechanical Engineering Commons](#)

DYNAMIC MODEL BASED STATE ESTIMATION IN A HEAVY DUTY  
DIESEL AFTERTREATMENT SYSTEM FOR ONBOARD DIAGNOSTICS  
AND CONTROLS

By

Harsha S. Surenahalli

A DISSERTATION

Submitted in partial fulfillment of the requirements for the degree of

DOCTOR OF PHILOSOPHY

Mechanical Engineering – Engineering Mechanics

MICHIGAN TECHNOLOGICAL UNIVERSITY

2013

© 2013 Harsha S. Surenahalli

This dissertation has been approved in partial fulfillment of the requirements for the Degree of DOCTOR OF PHILOSOPHY in Mechanical Engineering – Engineering Mechanics.

Department of Mechanical Engineering – Engineering Mechanics

Dissertation Advisor: Dr. Gordon G. Parker

Dissertation Co-Advisor: Dr John H. Johnson

Committee Member: Dr. Jeffrey D. Naber

Committee Member: Dr. Jason M. Keith

Department Chair: Dr. William W. Predebon

# CONTENTS

<b>List of Figures</b> . . . . .	xv
<b>List of Tables</b> . . . . .	xiv
<b>Acknowledgments</b> . . . . .	xv
<b>List of Symbols</b> . . . . .	xvii
<b>Abstract</b> . . . . .	xx
<b>1 Introduction</b> . . . . .	1
<b>2 Background and Literature Review</b> . . . . .	8
2.1 Onboard Diagnostics(OBD) and Controls . . . . .	8
2.2 State Estimation Strategies and Onboard Diagnostics . . . . .	14
2.3 Reduced Order Models and Controls . . . . .	16

2.4	Extended Kalman Filter (EKF) Based State Estimator . . . . .	18
<b>3</b>	<b>Experimental Setup and Data . . . . .</b>	<b>21</b>
3.1	Experimental Test Setup . . . . .	21
3.2	DOC Test Data . . . . .	25
3.2.1	DOC Steady State Data . . . . .	25
3.2.2	DOC Active Regeneration Data . . . . .	30
3.2.3	DOC Transient Data . . . . .	34
3.3	SCR Test Data . . . . .	36
3.3.1	SCR Steady State Data . . . . .	36
3.3.2	SCR Transient Data . . . . .	38
<b>4</b>	<b>DOC and SCR High Fidelity Models . . . . .</b>	<b>40</b>
4.1	DOC High Fidelity Model . . . . .	40
4.1.1	Reactions in the DOC . . . . .	41
4.1.2	Mass and Energy Balance Equations . . . . .	43
4.1.3	High Fidelity Model Calibration . . . . .	45
4.1.4	Steady State Simulation . . . . .	45

4.1.5	Active Regeneration Simulation . . . . .	50
4.1.6	Transient Simulation . . . . .	55
4.1.7	Aged Data Simulation . . . . .	58
4.2	SCR High Fidelity Model . . . . .	63
4.2.1	Reactions in the SCR . . . . .	64
4.2.2	Mass and Energy Balance Equations . . . . .	66
4.2.3	High Fidelity Model Calibration . . . . .	68
4.3	SCR Aged Data Simulation . . . . .	69
<b>5</b>	<b>DOC and SCR Reduced Order Models . . . . .</b>	<b>71</b>
5.1	DOC Reduced Order Model Development . . . . .	72
5.2	SCR Reduced Order Model Development . . . . .	74
5.3	DOC Reduced Order Model Calibration . . . . .	76
5.3.1	Steady State Simulation . . . . .	76
5.3.2	Active Regeneration Simulation . . . . .	81
5.4	SCR Reduced Order Model Calibration . . . . .	86
<b>6</b>	<b>Extended Kalman Filter (EKF) Estimator Development . . . . .</b>	<b>90</b>

6.1	DOC Estimator Development . . . . .	90
6.2	DOC Estimator Simulation . . . . .	91
6.2.1	Active Regeneration Test Case Simulation . . . . .	92
6.2.2	FTP Transient Cycle Simulation . . . . .	95
6.3	SCR Estimator Development . . . . .	97
6.4	SCR Estimator Simulation and the Effect of $NO_X$ and $NH_3$ Sensors on State Estimation Quality . . . . .	99
6.4.1	Effect of $NO_X$ and $NH_3$ Sensors on State Estimator . . . . .	103
<b>7</b>	<b>Summary and Conclusions . . . . .</b>	<b>109</b>
7.1	DOC Estimation . . . . .	111
7.2	SCR Estimation . . . . .	112
	<b>References . . . . .</b>	<b>123</b>
<b>A</b>	<b><math>NH_3</math> Concentration Calculation from DEF Injector Flowrate . . . . .</b>	<b>124</b>
<b>B</b>	<b><math>NO_X</math> Sensor Model . . . . .</b>	<b>126</b>
<b>C</b>	<b>SCR Jacobian Calculations . . . . .</b>	<b>128</b>

# LIST OF FIGURES

1.1	Schematic of a typical 2010 heavy-duty diesel aftertreatment system . . . .	3
3.1	Schematic of the test cell . . . . .	24
3.2	Experimental measured DOC conversion efficiencies of $NO$ , $CO$ and $HC$ during steady state conditions at three DOC inlet space velocities . . . . .	29
3.3	Experimental measured DOC conversion efficiencies of $NO$ , $CO$ and $HC$ during active regeneration conditions at three DOC inlet space velocities . .	33
3.4	Experimental measured DOC inlet and outlet concentrations of $NO$ , $CO$ and $HC$ and temperatures during transient test . . . . .	34
3.5	Experimental measured SCR inlet concentrations of $NO$ , $NO_2$ and $NH_3$ during steady state test . . . . .	37
3.6	Experimental measured SCR inlet concentrations of $NO$ , $NO_2$ and $NH_3$ and the SCR inlet and outlet temperatures during surrogate FTP test . . . .	39
4.1	Schematic showing the exhaust flow through the DOC . . . . .	41



4.2	Schematic of the DOC high fidelity model showing the gas and surface phase concentrations and temperatures . . . . .	42
4.3	Comparison of the simulated and experimental DOC $CO$ conversion efficiencies . . . . .	47
4.4	Comparison of the experimental and simulated HC conversion efficiencies .	49
4.5	Comparison of the simulated and experimental DOC outlet $NO_2/NO_X$ ratio	50
4.6	Comparison of the simulated and experimental DOC $CO$ conversion efficiencies during active regeneration . . . . .	52
4.7	Comparison of the experimental and simulated DOC HC conversion efficiencies during active regeneration . . . . .	53
4.8	Comparison of the simulated and experimental DOC outlet $NO_2/NO_X$ ratio during active regeneration . . . . .	54
4.9	Comparison of the experimental and simulated DOC outlet temperatures . .	55
4.10	Comparison of the DOC outlet temperature, $HC$ concentration, $NO_2/NO_X$ ratio and $CO$ concentration for the surrogate FTP cycle . . . .	57
4.11	Comparison of the experimental and simulated DOC outlet $HC$ , $NO_2$ and $CO$ concentrations for the degreened data . . . . .	59
4.12	Comparison of the experimental and simulated DOC outlet $HC$ , $NO_2$ and $CO$ concentrations for the aged data . . . . .	61

4.13	Comparison of the SCR outlet $NO$ , $NO_2$ and $NH_3$ concentrations between the experimental and the high-fidelity model corrected for sample line effects[1]. . . . .	68
5.1	Schematic showing the differences between high fidelity and reduced order DOC model . . . . .	73
5.2	Schematic showing the differences between high fidelity and reduced order SCR model . . . . .	74
5.3	Comparison of DOC outlet HC conversion efficiencies between the high fidelity and reduced order model for the steady state data . . . . .	78
5.4	Comparison of DOC outlet $NO_2/NO_X$ ratios between the high fidelity and reduced order model for the steady state data . . . . .	79
5.5	Comparison of DOC outlet CO conversion efficiencies between the high fidelity and reduced order model for the active regeneration experiments . .	82
5.6	Comparison of DOC outlet HC conversion efficiencies between the high fidelity and reduced order model for the active regeneration experiments . .	83
5.7	Comparison of DOC outlet $NO_2/NO_X$ ratios between the high fidelity and reduced order model for the active regeneration experiments . . . . .	84
5.8	Comparison of DOC outlet temperature between the high fidelity and reduced order model with respect to experimental DOC outlet temperature for the active regeneration experiments . . . . .	85

5.9	Comparison of the reduced order model with the experimental and high fidelity model results for test 8 . . . . .	87
5.10	Comparison of the reduced order model with the experimental and high fidelity model results for test 2. . . . .	89
6.1	Schematic showing the inputs to the estimator from the sensors and ECU maps . . . . .	92
6.2	Simulated temperature sensor measurement with Gaussian noise for test case	93
6.3	DOC inlet hydrocarbon concentration and a comparison between the simulated and estimated HC concentration and temperature at the 10 <sup>th</sup> element	94
6.4	Comparison of the DOC outlet $NO_2$ concentrations and temperatures with the estimator in open loop for the FTP cycle . . . . .	95
6.5	Comparison of the DOC outlet $NO_2$ concentrations and temperatures with the estimator in closed loop for the FTP cycle . . . . .	96
6.6	Schematic of the inputs to the SCR state estimator with the sensors downstream of the SCR . . . . .	98
6.7	Comparison of the measured and estimated SCR outlet $NO$ and $NO_2$ concentrations and $NH_3$ sensor signal for the FTP cycle with the estimator in open loop - without any sensors downstream of the SCR . . . . .	100

6.8	Comparison of the measured and estimated SCR outlet $NO$ and $NO_2$ concentrations and $NH_3$ sensor signal for the FTP cycle with the estimator in closed loop - with both $NO_X$ and $NH_3$ sensor downstream of the SCR . . .	101
6.9	Comparison of the $NH_3$ storage between an open loop and closed loop estimator for the FTP cycle - with both $NO_X$ and $NH_3$ sensor downstream.	102
6.10	Comparison of the measured and estimated SCR outlet $NO$ and $NO_2$ concentrations and $NH_3$ sensor signal for the FTP cycle - with just $NO_X$ sensor downstream. . . . .	104
6.11	Comparison of the measured and estimated SCR outlet $NO$ and $NO_2$ concentrations and $NH_3$ sensor signal for the FTP cycle - with just $NH_3$ sensor downstream. . . . .	105
B.1	Comparison of the $NO_X$ sensor model with the $NO_X$ sensor measurement	127

# LIST OF TABLES

1.1	EPA emission standards for heavy duty diesel engines [2] . . . . .	2
1.2	Monitoring requirements of EPA and California OBD systems[3] . . . . .	4
1.3	EPA thresholds for 2010 and later heavy-duty diesel engines[4] . . . . .	5
3.1	Aftertreatment system specifications . . . . .	22
3.2	Measurements and measurement locations in the test cell . . . . .	23
3.3	Test matrix for the steady state data showing the DOC inlet and outlet <i>CO</i> , <i>NO</i> , <i>NO<sub>2</sub></i> and <i>HC</i> concentrations and the DOC inlet temperature and space velocities(SV) . . . . .	27
3.4	Test matrix for the active regeneration tests showing the DOC inlet and out- let <i>CO</i> , <i>NO</i> , <i>NO<sub>2</sub></i> and <i>HC</i> concentrations and the DOC inlet temperatures and space velocities. The <i>HC</i> injection was achieved through in cylinder post injection . . . . .	31
3.5	Test matrix for the SCR steady state tests showing the SCR inlet <i>NO</i> , <i>NO<sub>2</sub></i> and <i>NH<sub>3</sub></i> concentrations along with the SCR inlet temperatures . . . . .	37

4.1	Kinetic parameters used to simulate steady state conditions . . . . .	46
4.2	Kinetic parameters used to simulate active regeneration . . . . .	51
4.3	Kinetic parameters used to simulate Johnson Matthey degreened data . . . .	60
4.4	Kinetic parameters used to simulate Johnson Matthey degreened and aged data . . . . .	63
4.5	The important kinetic parameters to simulate degreened and aged SCR data	70
5.1	Steady state testing conditions . . . . .	76
5.2	Kinetic parameters used to simulate steady state data . . . . .	77
5.3	Comparison of the reduced order simulated and the experimental DOC out- let $CO$ , $NO$ , $NO_2$ and $HC$ concentrations for the steady state data . . . . .	80
5.4	Comparison of the reduced order simulated and the experimental DOC out- let $CO$ , $NO$ , $NO_2$ and $HC$ concentrations for the active regeneration data .	86
6.1	Maximum errors and the standard deviation of the errors between the mea- sured and estimated SCR outlet concentrations with $NO_X$ sensor, $NH_3$ sensor and both $NO_X$ and $NH_3$ sensors for the surrogate FTP cycle. . . . .	106
6.2	Maximum errors and the standard deviation of the errors between the mea- sured and estimated SCR outlet concentrations with $NO_X$ sensor, $NH_3$ sensor and both $NO_X$ and $NH_3$ sensors for the surrogate FTP cycle for two sections of the test . . . . .	108

B.1	Kinetic parameters used to simulate steady state conditions . . . . .	127
C.1	States and outputs of an SCR with 2 axial elements . . . . .	128

## ACKNOWLEDGMENTS

This PhD thesis has been made possible with support from several important people in my professional and personal life. I would like to take this opportunity to thank some of the important people. I thank my PhD advisors Dr. Gordon Parker and Dr. John Johnson whose dedication, expertise and attention to detail have helped me become a better researcher. I would like to thank them for providing me the moral and financial support to complete this research work. The knowledge I have acquired under their guidance will continue to guide me towards being a successful researcher. I would also like to thank my committee members Dr. Jeffery Naber and Dr. Jason Keith for guiding me in my research work. I would also like to thank my colleague Xiaobo Song for the developing and calibrating the SCR high fidelity model and conducting the experiments to acquire the test data for the DOC and SCR.

I would like to thank U.S Department of Energy for providing the financial support for the project and John Deere for GRA support. I would also like to thank the industry partners John Deere, Navistar, Cummins and Johnson Matthey for evaluating the models and Johnson Matthey for providing the DOC aged data.



I would like to thank my parents Shivashankar S.G and Hemalatha , my wife Vathsalya, my sister Seema, my brother in law Niranjan and my uncle Dr Manju Prakash. Their constant moral support and encouragement has been the driving factor. I would like to dedicate this thesis to my wonderful mom and dad and my lovely wife Vathsalya.

I would like to thank all my family and friends at Michigan Tech and back home in India who have been instrumental in me getting to this point.

"This material is based upon work supported by the Department of Energy National Energy Technology Laboratory under Award Number(s) DEEE0000204."

#### **DISCLAIMER**

"This report was prepared as an account of work sponsored by an agency of the United States Government. Neither the United States Government nor any agency thereof, nor any of their employees, makes any warranty, express or implied, or assumes any legal liability or responsibility for the accuracy, completeness, or usefulness of any information, apparatus, product, or process disclosed, or represents that its use would not infringe privately owned rights. Reference herein to any specific commercial product, process, or service by trade name, trademark, manufacturer, or otherwise does not necessarily constitute or imply its endorsement, recommendation, or favoring by the United States Government or any agency thereof. The views and opinions of authors expressed herein do not necessarily reflect those of the United States Government or any agency thereof."

# LIST OF SYMBOLS

## Acronyms:

DOC - Diesel Oxidation Catalyst

CPF - Catalyzed Particulate Filter

SCR - Selective Catalytic Reduction

OBD - Onboard Diagnostics

EKF - Extended Kalman Filter

SI - Spark Ignition

EPA - Environmental Protection Agency

PM - Particulate Matter

NMHC - Non Methane Hydrocarbons

ECU - Engine Control Unit

## Variables:

$\epsilon$  - Void fraction of the catalyst

$C_g$  - Gaseous concentration of the species  $\left(\frac{\text{mol}}{\text{m}^3}\right)$

$C_s$  - Surface concentration of the species  $\left(\frac{\text{mol}}{\text{m}^2}\right)$

$C$  - Bulk concentration of the species  $\left(\frac{\text{mol}}{\text{m}^3}\right)$

$A_g$  - Geometric surface area ( $\frac{m^2}{m^3}$ )

$\beta$  - Mass transfer co-efficient

$R_i$  - Reaction rates ( $\frac{mol}{m^3.s}$ )

$T_g$  - Gaseous temperature (K)

$T_s$  - Surface temperature (K)

$T$  - Bulk temperature (K)

$\rho$  - Density of exhaust gas ( $\frac{kg}{m^3}$ )

$C_v$  - Specific heat of exhaust at constant volume ( $\frac{J}{kg.K}$ )

$C_p$  - Specific heat of exhaust at constant pressure ( $\frac{J}{kg.K}$ )

$u$  - Velocity of exhaust gas ( $\frac{m}{s}$ )

$h_g$  - Heat transfer coefficient between gas and surface phase ( $\frac{J}{m^2.s.K}$ )

$h_a$  - Heat transfer coefficient to ambient ( $\frac{J}{m^2.s.K}$ )

$\Delta h$  - Enthalpy of reaction ( $\frac{J}{mol}$ )

$MW$  - Molecular weight ( $\frac{mol}{g}$ )

$\rho_s$  - Density of substrate ( $\frac{kg}{m^3}$ )

$C_{p,s}$  - Specific heat capacity of the substrate ( $\frac{J}{kg.K}$ )

$G$  - Inhibition factors

$K_P$  - Equilibrium constant

$k$  - Reaction rate constants

$A$  - Pre exponential factor

$E_a$  - Activation energy

$P$  - Exhaust gas pressure(kpa)

$\Delta G$  - Gibbs free energy

$R$  - Universal gas constant

$A_a$  - Adsorption constants

$\Delta H_a$  - Adsorption heats

$\theta$  -  $NH_3$  Storage fraction

$\Omega$  - Storage capacity ( $\frac{\text{mol}}{\text{m}^3}$ )

**Vectors:**

$\vec{x}_k$  - State vector

$\vec{u}_k$  - Input vector

$\vec{y}_k$  - Output vector

$\vec{v}_k$  - Observation noise vector

$\vec{w}_k$  - Process noise vector

$\vec{P}_k$  - Estimation error covariance

$\vec{K}_K$  - Optimal Kalman Gain

## Abstract

Estimating un-measurable states is an important component for onboard diagnostics (OBD) and control strategy development in diesel exhaust aftertreatment systems. This research focuses on the development of an Extended Kalman Filter (EKF) based state estimator for two of the main components in a diesel engine aftertreatment system: the Diesel Oxidation Catalyst (DOC) and the Selective Catalytic Reduction (SCR) catalyst. One of the key areas of interest is the performance of these estimators when the catalyzed particulate filter (CPF) is being actively regenerated.

In this study, model reduction techniques were developed and used to develop reduced order models from the 1D models used to simulate the DOC and SCR. As a result of order reduction, the number of states in the estimator is reduced from 12 to 1 per element for the DOC and 12 to 2 per element for the SCR. The reduced order models were simulated on the experimental data and compared to the high fidelity model and the experimental data. The results show that the effect of eliminating the heat transfer and mass transfer coefficients are not significant on the performance of the reduced order models. This is shown by an insignificant change in the kinetic parameters between the reduced order and 1D model for simulating the experimental data.

An EKF based estimator to estimate the internal states of the DOC and SCR was developed. The DOC and SCR estimators were simulated on the experimental data to show that the estimator provides improved estimation of states compared to a reduced order model. The results showed that using the temperature measurement at the DOC outlet improved the estimates of the  $CO$ ,  $NO$ ,  $NO_2$  and  $HC$  concentrations from the DOC. The SCR estimator was used to evaluate the effect of  $NH_3$  and  $NO_X$  sensors on state estimation

quality. Three sensor combinations of  $NO_X$  sensor only,  $NH_3$  sensor only and both  $NO_X$  and  $NH_3$  sensors were evaluated. The  $NO_X$  only configuration had the worst performance, the  $NH_3$  sensor only configuration was in the middle and both the  $NO_X$  and  $NH_3$  sensor combination provided the best performance.

# 1. INTRODUCTION

Diesel engines are known for their high thermal efficiency and high torque characteristics compared to spark-ignition(SI) engines. The high torque characteristics of the diesel engine make them ideal for heavy load applications. Hence, diesel engines have been used to power most of the heavy duty trucks around the world. Diesel engines have also been used in light duty trucks and cars due to their low fuel consumption compared to SI engines. Similar to the SI engine, a diesel engine also produces undesirable green house gases and particle pollutants. Most of the countries around the world have some kind of regulations to regulate these emissions. In the Unites States, the emission regulations are set by the Environmental Protection Agency (EPA). The regulated emissions for heavy duty diesel engines are carbon monoxide ( $CO$ ), nitrogen oxides ( $NO_x$ ) , unburnt hydrocarbons (HC) and particulate matter (PM). Table 1.1 shows the EPA emission standards from 1988 to 2010. It can be seen that the limits for all the regulated emissions have been progressively lowered from 1988 to 2010.

**Table 1.1**  
EPA emission standards for heavy duty diesel engines [2]

	HC	CO	NO <sub>x</sub>	PM
Year	g/bhp-hr	g/bhp-hr	g/bhp-hr	g/bhp-hr
1988	1.30	15.50	10.70	0.60
1990	1.30	15.50	6.00	0.60
1991	1.30	15.50	5.00	0.25
1994	1.30	15.50	5.00	0.10
1998	1.30	15.50	4.00	0.10
2002	0.50	15.50	2.40	0.10
2007	0.14	15.50	0.20	0.01

To meet the 2010 EPA  $NO_X$  and PM emission standards, a typical 2010 aftertreatment system for heavy duty diesel engines consists of a DOC, CPF and SCR as shown in Figure 1.1. The figure also shows a Ammonia Oxidation Catalyst (AMOX) downstream of the SCR. The AMOX is used to oxidize the ammonia slip from the SCR. The figure also shows a  $NO_X$  sensor upstream of the DOC to measure inlet  $NO_X$  to the aftertreatment system and a  $NO_X$  sensor downstream of the AMOX to measure the  $NO_X$  out of the SCR. The DP sensor is used to measure pressure drop across the CPF and temperature sensors are used to measure temperatures at different locations in the aftertreatment system. Likely, between 2013-2016, the aftertreatment system will still contain these three components with higher SCR  $NO_X$  conversion efficiencies so that the fuel consumption of the engine can be reduced to meet the proposed 2014-2018 fuel consumption regulations [3]. The DOC oxidizes carbon monoxide ( $CO$ ) and hydrocarbons in the exhaust to  $CO_2$  and  $H_2O$  and oxidizes  $NO$  to  $NO_2$ . The CPF filters and oxidizes the PM in the exhaust and at the same time oxidizes the hydrocarbons to  $CO_2$  and  $H_2O$  and oxidizes  $NO$  to  $NO_2$  and consumes  $NO_2$  in oxidizing the PM. During normal engine operation ( $T < 400^0C$ ), the retained PM in the CPF is oxidized using  $NO_2$  [5] and the exhaust temperature. Active regeneration is



performed periodically by injecting the diesel fuel into the exhaust to oxidize the PM using  $O_2$  at higher temperatures ( $T > 500^\circ C$ ) [6]. The SCR catalyst reduces  $NO$  and  $NO_2$  in the exhaust to  $N_2$  and water. This is achieved by injecting urea upstream of the SCR catalyst, which thermally decomposes into  $NH_3$  and reacts with  $NO$  and  $NO_2$  on the active sites of the catalyst. The DOC either directly or indirectly affects the performance of the CPF and SCR and the CPF affects the SCR performance by the  $NO_2/NO_X$  ratio out of the filter.

The onboard diagnostic (OBD) systems that monitors the emission control system has

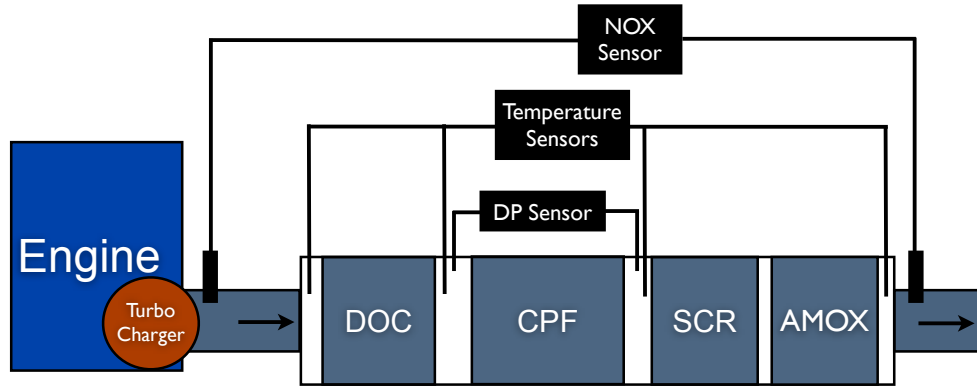


**Figure 1.1.** Schematic of a typical 2010 heavy-duty diesel aftertreatment system

been implemented on SI engines since 1991 and more stringent OBD standards were implemented in 1996. All light duty diesel engines have been required to meet OBD standards since 2004. From 2010 onwards, the OBD standards were implemented for heavy-duty diesel engines. By 2013 all the diesel engines manufactured are required to meet the OBD standards. Table 1.2 shows the OBD monitoring requirements for heavy duty diesel aftertreatment systems. The table shows specifications related to the performance and failure related monitoring systems for the DOC, CPF and SCR aftertreatment system components. Along with the performance related monitoring, the table also indicates the monitoring of catalyst aging. With regards to the sensors, the rule also specifies the monitoring of the

**Table 1.2**  
Monitoring requirements of EPA and California OBD systems[3]

System/Component	Parameter Requiring Monitoring
NMHC(Non Methane Hydrocarbons) catalyst Conversion efficiency	Provide DPF heating Provide SCR feedgas (e.g., NO <sub>2</sub> ) Provide post DPF NMHC clean-up Provide ammonia clean-up Catalyst aging
SCR NO <sub>x</sub> catalyst	Conversion efficiency SCR reductant: - delivery performance, - tank level, quality, and - injection feedback control Catalyst aging
NO <sub>x</sub> adsorber	NO <sub>x</sub> adsorber capability Desorption function fuel delivery Feedback control
DPF Filtering performance	Frequent regeneration NMHC conversion Incomplete regeneration Missing substrate Active regeneration fuel delivery Feedback control
Exhaust gas sensors	For air-fuel ratio and NO <sub>x</sub> sensors: - performance, - circuit faults, - feedback, and - monitoring capability Other exhaust gas sensors Sensor heater function Sensor heater circuit faults

failure of the sensors and circuits and any auxiliary devices associated with the sensors such as heaters.

Table 1.3 shows the thresholds for detecting the failure of these systems. The thresholds are specified either in terms of the multiples of the emission standards (indicated with a 'x'

**Table 1.3**  
EPA thresholds for 2010 and later heavy-duty diesel engines[4]

Monitor	Model Year	Diesel Threshold			
		NMHC	CO	$NO_X$	PM
		g/bhp-hr			
$NO_X$ catalyst system	2010-2012	-	-	+0.6	-
	2013 & later	-	-	+0.3	-
DPF system	2010-2012	2.5x	-	-	+0.05 or +0.04
	2013 & later	2x	-	-	+0.05 or +0.04
$NO_X$ sensors	2010-2012	-	-	+0.6	+0.05 or +0.04
	2013 & later	-	-	+0.3	+0.05 or +0.04
Other monitors with emissions thresholds	2010-2012	2.5x	2.5x	+0.3	+0.03 or +0.02
	2013 & later	2x	2x	+0.3	+0.03 or +0.02

after a number in the table) or in terms of absolute value of the species (indicated by '+' in front of a number). The onboard diagnostic strategies are required to detect and inform the driver when any of the regulated emissions exceed the limits indicated in Table 1.3 .

The DOC, CPF and SCR contain un-measurable states (such as PM retained in the CPF and  $NH_3$  storage in the SCR) that need to be estimated for diesel fuel injection for active regeneration and urea injection control systems on-board the vehicle. To optimize the performance of the aftertreatment system, it is necessary to estimate the internal states in real time and use them for control system and onboard diagnostics (OBD) strategy implementation. In order to meet the 2014-18 fuel consumption standards, the use of fuel for active regeneration must be minimized and the fuel injection control strategy must be optimized. To achieve this, it is important to know the hydrocarbon and temperature states in the DOC and to optimize the urea injection so as to minimize the urea use and maximize the  $NO_X$  reduction.

One of the important aspects of state estimation is to have a reduced order model of

the dynamic system. A reduced order DOC and SCR model and corresponding Extended Kalman Filter (EKF) state estimation strategy is discussed relative to the research that has been conducted for this thesis.

The literature review of section 3 shows that models and sensors are valuable tools to assist in estimating states that cannot be measured. The models provide additional information based on the inputs to the system. The limitations of using the models to estimate states is that the error between the estimated and true states is high if the model is not an accurate representation of the system. With an optimal state estimator, even if the system is not well known, the estimation error is minimized. Hence, the main objective of this research is to create state estimation strategies for the DOC and SCR heavy duty diesel aftertreatment components. The state estimation strategies include development of reduced order models, evaluation of state estimation strategies and evaluation of estimation quality based on several different sensor combinations. The general objectives can be divided into reduced order model development and state estimator development.

1. The objectives for the reduced order models: (a) Develop reduced order model for the DOC and SCR. (b) Validate the performance of the reduced order models with the experimental data and the high-fidelity models.
2. The objectives for the state estimation: (a) Develop Kalman Filter based state estimators to estimate states in the DOC and SCR. (b) Validate the performance of the estimators with the experimental data. (c) Evaluate the several different sensor combinations needed to estimate the states in both the DOC and SCR.

The thesis is organized as follows: 1. Introduction, 2. Background and Literature Review, 3. Experimental Setup and Data, 4. DOC and SCR High Fidelity Models, 5. DOC and SCR Reduced Order Models, 6. Extended Kalman Filter(EKF) Estimator Development and Simulations and 7. Summary and Conclusions.

## **2. BACKGROUND AND LITERATURE REVIEW**

This section provides an review of the significant relevant literature with respect to the reduced order model development and state estimation strategy development. There are four subsections:

1. Onboard Diagnostics and Controls.
2. State Estimations Strategies and Onboard Diagnostics - describes the states estimation strategies and the onboard diagnostics.
3. Reduced Order Models and Controls - describes the reduced order models and controls

### **2.1 Onboard Diagnostics(OBD) and Controls**

Onboard Diagnostics or OBD are tools which provide the ability to monitor and detect the status of different subsystems in a vehicle. On-Board-Diagnostics concepts assist in trouble shooting the problems in the vehicle subsystem and help manufacturers monitor the state of the different components and also detect any failures. A failure in the aftertreatment

system would result in the vehicle exceeding the legal emission limits. OBD strategies can detect any critical failures and provide the user the limp home capability to prevent any serious damage and reduce the cost of repairs[7].

Any physical failure of aftertreatment devices can be detected with the sensors already present in the production system. To detect any performance related failures, models could be used to check the performance of the actual device with the simulated values. To do this, the models need to be very accurate and computationally efficient. For an SCR an efficient and robust control system would be useful in controlling the urea injection and the performance of the SCR. There are two kind of control systems that have been reported in the literature - open loop and closed loop control systems.

**Open Loop Control Systems:** The heavy duty diesel industry have used open loop control systems to control the urea injection into the SCR. The open loop control strategies provide good  $NO_X$  conversion performance and are very stable and easy to implement. The open loop control strategies inject urea based on the  $NO_X$  estimate at the SCR inlet. The control laws determine the  $NO_2 / NO_X$  ratios from the engine maps for a particular engine speed and load and then estimate the amount of urea injection. This often results in the over injection of urea and results in higher  $NH_3$  slip at the SCR outlet. To overcome this problem, manufacturers have used a Ammonia Oxidation Catalyst (AMOX), which oxidizes the  $NH_3$  in the exhaust to  $N_2$  and  $H_2O$  . This increases the total cost of the aftertreatment system.

**Closed Loop Control Systems:** Another solution is to use a closed loop control system. The closed loop control system would minimize the ammonia slip at the SCR outlet and it is also possible to retain the high  $NO_X$  conversion efficiency. A closed loop control on an SCR is challenging due to the slow dynamics of the SCR and the response of the urea

injection system. Several researchers have proposed  $NO_X$  and  $NH_3$  sensor based control strategies. These control strategies use the  $NH_3$  or  $NO_X$  sensors located at the SCR outlet to determine the amount of urea injection. The objective of these strategies have been to maintain the  $NH_3$  storage in the SCR at a optimum level. To achieve this, the control system use models to estimate the  $NH_3$  storage along with a linearized first order model for the SCR to determine the urea injection quantity. The first order models are developed from the CFD models and are an approximation of the SCR. Since the SCR is a non linear system, all the controls oriented models use variable parameters in the transfer function of the system. The parameters in the first order transfer function vary as a function of SCR inlet temperature and mass flow rates. To estimate the  $NH_3$  storage,  $NH_3$  balance models are used. Several researchers have compared the performance of different control strategies. Some of the important literature are reviewed in this section.

The researchers in reference[8] compared the performance of a closed loop feedforward and an open loop control system for urea injection. The performance of the controllers were evaluated at steady state conditions and the results showed that closed loop control reduced the steady state error to 5% which was not possible with an open loop controller. The evaluation of the control strategies on transient conditions showed that closed loop controller improves the transient SCR  $NO_X$  reduction performance. The authors concluded that the closed loop control is a must to meet the EPA 2010 emission standards.

The goal of the study in reference [9] was to evaluate the modeling approaches and to develop models which can be used for control system development. The paper infers that simplistic models might lack physical representations and such models will have limited applications. The paper states that the kinetics parameters of the catalyst should be included in the models in some way to enable the control systems to account for the aging



related performance changes. The authors concluded that more complex models and observers would be useful to develop advanced control strategies and could help in increasing the conversion efficiencies of the aftertreatment system.

The goal of the research work in reference [10] was to develop a control oriented model for the SCR and develop a feedforward control system for urea injection. The model developed consisted of ODE's for the gas and surface phase concentrations and PDE's for temperature and  $NH_3$  storage on a single storage site. The model was then used to develop model based feedforward controls for urea injection. The feedforward control system was developed with a goal to maintain constant  $\frac{NO_X}{NH_3}$  ratio at the SCR outlet. The controller was implemented and validated on an engine dynamometer. The controller achieved up to 85%  $NO_X$  conversion efficiency with reduced  $NH_3$  slip compared to a open loop controller.

In reference [11] the researchers evaluated the possibility of using the  $NO_X$  sensor to monitor the health of the SCR. The  $NO_X$  sensor signals were compared to chemiluminescence detector (CLD) measurements. The  $NO_X$  sensor's cross sensitivity toward  $NH_3$  and other components in the exhaust were evaluated. The authors concluded that  $NO_X$  sensors are robust enough to implement in production systems and are very useful to implement control strategies.

The objective of the research in reference [12] was to develop an SCR control strategy for urea injection. A 1D single channel model to simulate the SCR was developed and calibrated to the experimental data. Using the 1D model a first order transfer function was derived to represent the SCR. The parameters for the transfer function model were estimated using Model Reference Adaptive Control with composite adaptation law. The first order model was used to develop a closed loop self tuning control strategy with online adaptation of the controller gains. The transfer function model parameters are estimated

using time history of the SCR catalyst inlet concentrations , exhaust flow rates and temperatures. The controller was able to reduced the mean  $NH_3$  slip to less than 7 ppm and maximum slip to less than 55 ppm. The authors concluded that knowledge of the  $NH_3$  storage and temperature is very important for the performance of the controller.

The goal of reference [13] was to evaluate several OBD concepts for the SCR catalyst. The monitoring requirements and challenges associated with open and closed loop control strategies were discussed. The authors concluded that to meet the 2010 SCR OBD requirements, a closed loop control strategy is needed.

The objective of the research in reference [14] was to compare a  $NO_X$  sensor based control strategy with an open loop control strategy for the SCR. The authors compared a  $NO_X$  sensor based closed loop SCR surface coverage /  $NH_3$  slip control strategy with cross sensitivity compensation with an open loop control strategy. The authors concluded that the SCR catalyst dynamics, time delay in urea injection system and maximum  $NH_3$  slip targets limit the dynamic performance of the SCR closed loop control. The open loop control had high (>85%)  $NO_X$  conversion efficiency but was unable to adapt to 30% higher SCR inlet  $NO_X$  .

The objective of the research in reference [15] was to evaluate  $NO_X$  sensor based and  $NH_3$  sensor based control strategies. The  $NH_3$  sensor was used with a surface coverage /  $NH_3$  slip control strategy. The  $NH_3$  sensor signal was used as a feedback for  $NH_3$  slip and also to estimate  $NH_3$  coverage fraction. The  $NH_3$  sensor based control strategy achieved similar  $NO_X$  conversion efficiency but with lower  $NH_3$  slip.

The goal of the research in reference [16] was to compare  $NO_X$  based and  $NO$  and  $NO_2$  based control strategies. A linearized SCR model was used to develop and compare

$NO_X$  based and  $NO$  and  $NO_2$  based control strategies. The  $NO$  and  $NO_2$  based control strategy produced less SCR outlet  $NO_X$  compared to the  $NO_X$  based control strategy.

The objective of the research in reference [17] was to analyze the limitations and requirements for open loop and closed loop control systems for the SCR urea injection. The authors concluded that for feedforward open loop control strategies, the controller needs a good estimate of  $NO$  and  $NO_2$ . Since most of the time the  $NO$  and  $NO_2$  is not known accurately, the controller ends up injecting excess urea, which results in excess  $NH_3$  slip. For optimal  $NO_X$  conversion efficiency, the knowledge of accurate  $NH_3$  storage is important. This is especially important during transients and low temperature operation. The amount of  $NH_3$  stored in the SCR determines how long the high  $NO_X$  conversion at low temperatures can be maintained. The closed loop control system is affected by the quality of the sensor signals, the maximum  $NH_3$  slip limits, slow SCR dynamics and urea injection system delays. The major conclusion was that the performance of the SCR control system is a strong function of the estimated  $NH_3$  storage.

The authors in reference [18] compared the performance of a closed loop control strategy with  $NH_3$  sensor at the mid brick of an SCR and an open loop control strategy with a  $NO_X$  sensor. The performance of the closed loop control strategy was significantly improved by the inclusion of a  $NH_3$  sensor at mid brick location. The  $NH_3$  sensor located mid brick had faster response compared to the  $NH_3$  sensor at the SCR outlet. The faster  $NH_3$  sensor response improved the performance of the closed loop control system.

The objective of the research in reference[19] was to compare the performance of a proportional integral(PI) controller with  $NH_3$  storage estimate as feedback and an adaptive PI controller. The model for the controls was approximated by a first order transfer function. The parameters in the transfer function were estimated as a function of engine condition.

The results showed that both the controllers were able to achieve over 90% conversion efficiency and less than 2 ppm of peak  $NH_3$  slip.

The focus of the research in reference [20] was to experimentally evaluate  $NH_3$  storage as a function of aging. The storage capacity of the SCR was calculated with an hydrothermally aged SCR. The results showed that the SCR storage capacity changes with aging on exposure to high temperatures.

This objective of the reference [21] was to evaluate the cross sensitivities of the  $NO_X$  sensor to  $HCNO$ ,  $HCN$ ,  $NH_3$  and other components of the exhaust. The results show that the  $NO_X$  sensor is only sensitive to the  $NH_3$  in the exhaust.

Based on the literature review of the control systems for the SCR, it can be concluded that the both closed loop and open loop controls can achieve high  $NO_X$  Conversion efficiency, but a closed loop control strategy can also reduce the  $NH_3$  slip at the SCR outlet. The implementation of a closed loop control system on an SCR is limited by slow SCR dynamics, inaccurate estimate of the  $NH_3$  storage and the time delay in the urea injection system. One of the critical parameters in the control strategy performance for both open and closed loop control system is the accurate  $NH_3$  storage estimate.

## **2.2 State Estimation Strategies and Onboard Diagnostics**

To meet the increasingly stringent emission control standards, better control strategies need to be developed. Control strategy performance is a direct function of the ability to measure, estimate and use internal states. This is usually done using sensors, however implementing sensors to measure all the states needed for a controller is usually not possible

nor cost effective. Sometimes models and state estimators can be used as virtual sensors to estimate states that cannot be measured by a sensor. For the diesel engine application, these models and estimators must be implementable in the ECU. Thus, computational efficiency is of great importance in virtual sensor algorithm development. State estimators can also be used to detect degradation in the performance or failure of the system within an OBD strategy.

Either linear or nonlinear state estimation strategies should be implemented depending on the system's input output model form. Linear state estimation techniques are simpler and easier to implement as compared to nonlinear estimators. Since the models of after treatment devices are nonlinear, there is a performance penalty associated with using a linear state estimation strategy for this application. It can be done, but the system must be linearized about some operating point and the range of operation constrained about that point. Devarokonda et al. [16] and Na et al. [22] used linearized models for SCR state estimation and controls. In general, a linear state estimation technique applied to a non linear system results in large errors with increasing non linearities. To decrease the estimation errors, a non linear state estimation strategy should be used.

Recent work on Extended Kalman Filter (EKF) estimator design in diesel aftertreatment systems includes the  $NH_3$  storage estimator [23] and  $NO_X$  sensor cross-sensitivity estimator[24] for SCR catalysts by Hsieh et al. The authors also designed a  $NO$ - $NO_2$  concentration observer for both the DOC and CPF [25]. The main objective of the study was to estimate the  $NO$  and  $NO_2$  concentrations into the SCR. It should be noted that hydrocarbon and  $CO$  oxidation reactions were not considered in the estimator design. The presence of large concentrations of hydrocarbons during CPF active regeneration inhibits the  $NO$  oxidation reaction in the DOC [26,27]. Without modeling the  $CO$  and HC oxidation and

the inhibition effects, the  $NO$  and  $NO_2$  prediction during active regeneration condition will be not accurate.

## 2.3 Reduced Order Models and Controls

In order to develop state estimators, an accurate model of the system is necessary. The high fidelity models for the DOC[28–32] and the SCR[33,34], perform very well in predicting the performance characteristics, but these models are complex and implementing them on an ECU would require more computational resources[35]. So to implement control and OBD strategies, reduced order models are needed.

For a DOC, the important states that need to be estimated include the  $NO$  ,  $NO_2$  , hydrocarbon and temperatures states at the outlet of the DOC. The  $NO$  ,  $NO_2$  and temperature states are useful to predict passive PM oxidation in the CPF. The HC and temperature states during active regeneration are useful to predict the thermal oxidation of the retained PM, prevent CPF failures[36] and also give better control over the regeneration process itself[37].

There have been several approaches to develop reduced order models for the DOC. Singh et al.[38] developed a lumped parameter reduced order model to predict the DOC outlet hydrocarbon concentration and temperature during active regeneration. The DOC model was used along with a CPF model to evaluate control strategies. Birkby et al.[39] developed model based controls using a reduced order model to predict the hydrocarbon concentration and temperature out of the DOC. The objective of the research was to control the DOC outlet temperature during active regeneration conditions. Researchers in refer-

ences [40,41] developed a reduced order model to predict the  $C_3H_6$  oxidation across the DOC and the corresponding energy release. The authors also discuss the possibility of using the temperature response of the DOC for OBD.

In an SCR, the outlet  $NH_3$ ,  $NO$ ,  $NO_2$  and  $NH_3$  storage are the important states to estimate. Chi et al.[42] developed a 1D SCR model. The model consists of gas phase and surface phases for the species and energy balance. The objective of the study was to develop a urea injection control system to maintain the high  $NO_X$  conversion efficiency of the SCR. Deverakonda et al.[16,43] developed SCR reduced order models for the purpose of  $NO_X$  control. The research describes a 3-state and a 4-state SCR model. The models were compared to a more complex model and the experimental data. The authors concluded that a 4-state model is sufficient to predict the  $NO_X$  conversion across the SCR and is suitable for the implementation of urea injection control strategy. Devarokonda et al.[16] developed a linear state estimator based on the 4 state SCR model. A control strategy was implemented using the SCR state estimator and a  $NO_x$  sensor down stream of the SCR. Similarly Cho et al. [44] developed a 3 state SCR model with  $NO_X$ ,  $NH_3$  and  $NH_3$  storage as states. Herman et al.[45] developed a 1D SCR model to predict the  $NO_X$  conversion efficiency and the  $NH_3$  slip across the SCR. A control system was developed using a SCR model along with a  $NO_X$  sensor upstream of the SCR and a  $NH_3$  sensor downstream of the SCR. Oliveira Costa et al.[46] developed diagnostic strategies to detect changes in the performance of the SCR using a reduced order model. The  $NO_X$  conversion efficiency of the SCR model was compared with the actual SCR in real time to determine the changes in the conversion efficiency performance. Hollauf et al.[47] developed a reduced order model to implement a  $NH_3$  based control strategy to minimize the  $NH_3$  slip across the SCR. Mallouh et al.[48] used a combination of a linear and non linear SCR model to develop an adaptive proportional-integral(PI) control to prevent  $NO_X$  and  $NH_3$  slip at the

SCR outlet. The stored  $NH_3$ , SCR outlet  $NO_X$  and SCR outlet  $NH_3$  was assumed to be known to implement the control strategy. Na et al.[22] developed a reduced order model to implement control strategies. A linearized state space model was developed based on the reduced order model. McKinley et al [49] developed an eigen value based approach for controls oriented models. Stevens et al [50] developed a data driven model for the SCR and used the model to develop a urea injection profile for a HD-FTP test cycle which improved the  $NO_X$  conversion efficiency and reduced the amount of urea injected.

## 2.4 Extended Kalman Filter (EKF) Based State Estimator

The Extended Kalman Filter (EKF) is a nonlinear Kalman filter which linearizes about the current mean and covariance [51]. To implement an extended Kalman filter, the equations describing the model must be differentiable functions. A general discrete non linear system with states  $\vec{x}_k$ , inputs  $\vec{u}_k$  and noises  $\vec{w}_k$  and  $\vec{v}_k$  can be represented as [52].

$$\vec{x}_k = f_{k-1}(\vec{x}_{k-1}, \vec{u}_{k-1}, \vec{w}_{k-1}) \quad (2.1)$$

$$\vec{y}_k = h_k(\vec{x}_k, \vec{v}_k) \quad (2.2)$$

The function  $f$  is used to predict the state estimate and the function  $h$  is used to compute the predicted measurement.  $\vec{w}_k$  and  $\vec{v}_k$  are the process and observation noises, which are assumed to be zero mean multivariate Gaussian noises with covariance  $Q_k$  and  $R_k$  respectively. Implementation of EKF on such a system involves the following steps: [52].



**Compute the matrices  $F_k$  and  $L_k$  from  $f_{k-1}$**

$$F_k = \frac{\partial f_{k-1}}{\partial x} \big|_{\vec{x}_{k-1}, \vec{u}_{k-1}} \quad (2.3)$$

$$L_k = \frac{\partial f_{k-1}}{\partial w} \big|_{\vec{x}_{k-1}, \vec{u}_{k-1}} \quad (2.4)$$

**Update the state estimate and estimation error covariance**

$$\vec{x}_k^- = f_{k-1}(\vec{x}_{k-1}^+, \vec{u}_{k-1}, 0) \quad (2.5)$$

$$P_k^- = F_{k-1} P_{k-1}^+ F_{k-1}^T + L_{k-1} Q_{k-1} L_{k-1}^T \quad (2.6)$$

**Compute the matrices  $H_k$  and  $M_k$  from  $h_k$**

$$H_k = \frac{\partial h_k}{\partial x} \big|_{\vec{x}_k^-} \quad (2.7)$$

$$M_k = \frac{\partial h_k}{\partial v} \big|_{\vec{x}_k^-} \quad (2.8)$$

**Calculate the optimal Kalman gain**

$$K_k = P_k^- H_k^T (H_k P_k^- H_k^T + M_k R_k^- M_k^T)^{-1} \quad (2.9)$$

**Perform the measurement update of the state estimate and estimation error covariance**

$$\vec{x}_k^+ = \vec{x}_k^- + K_k (\vec{y}_k - h_k(\vec{x}_k^-, 0)) \quad (2.10)$$

These steps are followed at each time step and the covariance and gain matrices are updated with new values of the optimal Kalman gain matrix. An optimal estimator minimizes the estimation error by using the measured states and the knowledge of the known system. For

the Kalman Filter to be optimal, the system should satisfy the following conditions:

1. The process and observation noises  $\vec{w}_k$  and  $\vec{v}_k$  are known and are zero mean multi-variate Gaussian noises
2. The covariances of the noise are exactly known
3. For an EKF, the state transition and observation functions are not needed to be linear but must be differentiable functions

The literature review of the control systems have shown that accurate estimate of  $NH_3$  storage is very important for the performance of both an open loop and control loop system. Both  $NO_X$  and  $NH_3$  sensors can be used as feedback to a closed loop control system. The  $NH_3$  sensor used with feedback controls not only provides the high  $NO_X$  conversion efficiencies of  $NO_X$  sensor based control system but also reduces the  $NH_3$  slip at the SCR outlet. A model used to estimate the  $NH_3$  storage would be accurate during normal operation of the SCR, but when used with an aged SCR the model will fail to simulate the  $NH_3$  storage and  $NO$ ,  $NO_2$  and  $NH_3$  concentrations. State estimators with sensors can be used to estimate  $NH_3$  storage in realtime and can also be used to estimate  $NO$  and  $NO_2$  concentrations which can be used to develop better control strategies. In this dissertation, development of reduced order models and estimators for the DOC and SCR is described. The estimators are simulated on the experimental data and the effect of  $NO_X$  and  $NH_3$  sensors on SCR estimator performance is described.

### **3. EXPERIMENTAL SETUP AND DATA**

This section describes the experimental setup and the test matrices used to acquire the experimental data. The data to simulate both the DOC and SCR model were acquired using a 2010 Cummins ISB engine with Cummins production aftertreatment system.

#### **3.1 Experimental Test Setup**

The testing for the DOC and SCR was done using a 2010 cummins ISB engine with a 2010 Cummins ISB production system consisting of the DOC, CPF and SCR aftertreatment system. Table 3.1 shows the details and dimensions of the DOC, CPF, SCR and AMOX components. The DOC substrate is made of cordierite, has a diameter of 9.5in, length of 4in and celldensity of 400 cpsi. The DPF is substrate is made of cordierite, has a diameter of 9.5in, length of 12in and celldensity of 200 cpsi. The Cu-Zeolite SCR is made of cordierite, has a diameter of 10.5in, length of 12in and celldensity of 400 cpsi. The AMOX is made of cordierite, has a diameter of 10.5in, length of 4in and celldensity of 400 cpsi.

**Table 3.1**  
Aftertreatment system specifications

	DOC	DPF	SCR	AMOX
Material	Cordierite			
Diameter (inch)	9.5	9.5	10.5	10.5
Length (inch)	4	12	12	4
Cell Geometry	Square	Square	Square	Square
Total Volume (L)	4.65	13.94	17.03	5.68
Cell Density $\frac{1}{in^2}$	400	200	400	400
Cell Width (mil)	46	59	46	46
Filtration Area ( $in^2$ )	NA	19975	NA	NA
Open Frontal Area ( $in^2$ )	60	24	73	73
Channel Wall Thickness (mil)	4	12	4	4
Wall density ( $\frac{g}{cm^3}$ )	1.2	1.2	1.2	1.2
Porosity	0.35	0.59	0.35	0.35
Mean Pore Size ( $\mu m$ )	NA	15	NA	NA
Number of inlet cells	28353	7088	34636	34636

The test cell is equipped with a 2010 Cummins ISB engine coupled with an eddy current dynamometer. A schematic of the test cell setup is shown in Figure 3.1. The exhaust from the engine can be routed through two lines: baseline and trapline. Baseline is used to warm up the engine. When the exhaust is routed through the base line, the exhaust gas bypasses the aftertreatment system and goes directly to the building exhaust. This capability provides the ability to warm up and condition the engine before starting the experiments. When the exhaust is routed through the trap line the exhaust from the engine flows through the DOC, CPF and SCR aftertreatment system. The trapline is equipped with thermocouples and pressure drop transducers to measure the temperature and pressure drop across the DOC, CPF and SCR. The trapline is also equipped with the sample probes which can be used to sample the gaseous emissions upstream of the DOC, downstream of the DOC/upstream of CPF, downstream of CPF, upstream of the SCR and downstream of the SCR. The pressure drop sensor in the Laminar Flow Element(LFE) measures the air flow into the engine. The

fuel flow measurement from the AVL fuel flow meter along with the air flow rate is used to estimate the exhaust mass flow rate. The exhaust temperatures in the DOC , CPF and SCR are measured using K type thermocouples. The list of all the emission measurements, measurement locations and the instruments used are tabulated in Table 3.2.

**Table 3.2**  
Measurements and measurement locations in the test cell

Measurement	Measurement Location	Instruments
Pressure Drop	Upstream DOC Downstream DOC Downstream CPF Upstream SCR Downstream SCR	$\Delta P$ Transducer $\Delta P$ Transducer $\Delta P$ Transducer $\Delta P$ Transducer $\Delta P$ Transducer
Gaseous measurement	Upstream DOC Downstream DOC Downstream CPF Upstream SCR Downstream SCR	Mass Spectrometer/5 Gas Analyzer Mass Spectrometer/5 Gas Analyzer Mass Spectrometer/5 Gas Analyzer Mass Spectrometer/5 Gas Analyzer Mass Spectrometer/5 Gas Analyzer
Temperature	Upstream DOC Downstream DOC Downstream CPF Upstream SCR Downstream SCR In the DOC, CPF & SCR	K Type Thermocouples K Type Thermocouples K Type Thermocouples K Type Thermocouples K Type Thermocouples K Type Thermocouples
Sensors	Upstream DOC Downstream SCR	$NO_X$ Sensor $NO_X$ and $NH_3$ sensor
PM concentration measurement	Upstream DOC Downstream CPF	Stack Sampler Stack Sampler
PM particle size measurement	Upstream DOC Downstream DOC Downstream CPF Upstream SCR Downstream SCR	Scanning Mobility Particle Sizer Scanning Mobility Particle Sizer Scanning Mobility Particle Sizer Scanning Mobility Particle Sizer Scanning Mobility Particle Sizer
Engine airflow	Engine Inlet	Laminar Flow Element
Engine fuel flow	Engine Inlet	AVL Fuel Flow Meter

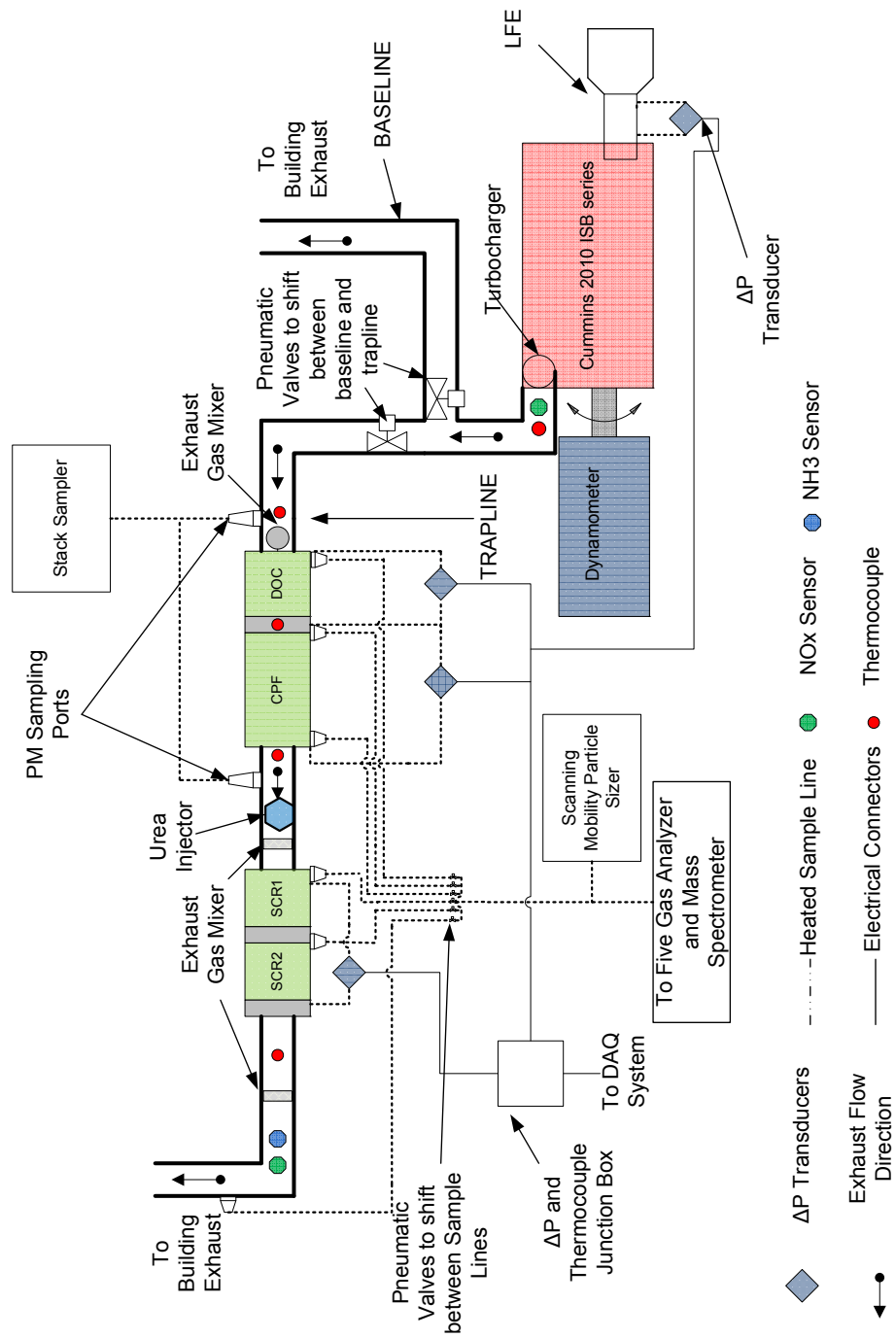


**Figure 3.1.** Schematic of the test cell

## 3.2 DOC Test Data

The goal of the experimental studies of the DOC was to collect data to use for identification of the kinetic parameters in the DOC model. To achieve this, the tests were divided into steady state, active regeneration and transient tests. The steady state experiments were designed to identify the kinetic parameters during normal engine operating conditions. The active regeneration experiments were designed to identify kinetic parameters during active regeneration conditions and the transient tests were developed to identify the transient behavior of the DOC including the transient temperature response of the substrate due to the thermal inertia and the heat transfer to the ambient.

### 3.2.1 DOC Steady State Data

The objective of the DOC steady state experiments was to acquire performance data that can be used to identify the kinetic parameters in the DOC model. The performance of the DOC is a function of DOC inlet temperature and the inlet space velocities. To capture the effect of both space velocity and the temperature, the tests were developed such that the DOC inlet temperatures and space velocities were varied. To capture the effect of space velocity three space velocities of  $162k$ ,  $235k$  and  $281k \text{ hr}^{-1}$  were selected as shown in table 3.3. The space velocity of the exhaust is calculated at the actual temperature and pressure and the equation to calculate the actual space velocities are calculated using Equation 3.1.

$$SpaceVelocity(Actual) = \frac{MassFlowRate}{ExhaustGasDensity(ActualTemperature)} \quad (3.1)$$

These space velocities were selected to cover the range of space velocities observed by the DOC during normal engine operation. At each of these space velocities the DOC inlet temperature was varied from 237 to 474<sup>0</sup>C as shown in table 3.3. The engine speed and load were varied to achieve different DOC inlet temperatures while keeping the DOC inlet space velocity constant.

Table 3.3 shows the tabulated values of DOC inlet and outlet *CO* , *NO* , *NO<sub>2</sub>* and hydrocarbon (*HC* ) concentrations and DOC inlet temperature for the steady state testing. The first column in the table is the DOC inlet space velocities at actual temperatures and the second column shows the DOC inlet mass flow rate in *kg/min* . The rest of the table is divided into DOC inlet and outlet concentrations and temperatures. The first column under the DOC inlet shows the DOC inlet temperature in <sup>0</sup>C, the second, third and fourth columns show the DOC inlet *CO* , *NO* , *NO<sub>2</sub>* concentrations in *ppm* and the fifth column shows the DOC inlet *HC* concentrations in *ppmC*. The columns under DOC outlet shows *CO* , *NO* and *NO<sub>2</sub>* concentrations in *ppm* and the *HC* concentrations in *ppmC*.



**Table 3.3**

Test matrix for the steady state data showing the DOC inlet and outlet  $CO$ ,  $NO$ ,  $NO_2$  and  $HC$  concentrations and the DOC inlet temperature and space velocities(SV)

SV *		Inlet					Outlet			
$hr^{-1}$	$\dot{M}$ $\frac{kg}{min}$	$T_{in}$ $^{\circ}C$	$CO$ $ppm$	$NO$ $ppm$	$NO_2$ $ppm$	$HC$ $ppm_{C1}$	$CO$ $ppm$	$NO$ $ppm$	$NO_2$ $ppm$	$HC$ $ppm_C$
162k	7.4	237	83	287	44	98	0	150	182	12.9
	6.6	296	63	301	33	103	0	102	232	8.7
	6.4	315	56	395	32	98	0	128	298	8.0
	6.2	352	53	434	24	90	0	170	288	5.8
	5.5	399	73	587	18	73	0	329	276	3.9
	5.8	374	81	480	23	82	0	215	288	4.5
	5.4	431	81	669	14	63	0	455	228	3.6
	5.2	457	96	970	14	53	0	759	225	4.0
	7.0	272	69	283	37	102	0	111	209	11.1
235k	10.0	252	88	206	42	122	0	129	119	23.6
	10.1	275	82	242	40	116	0	131	151	23.1
	8.3	390	61	331	16	91	1	182	165	10.6
	8.9	345	67	282	27	100	0	121	188	13.6
	8.3	369	63	306	21	96	1	148	179	11.4
	7.9	439	107	497	13	61	1	368	142	6.8
	7.3	462	205	490	13	51	1	407	96	6.6
	7.0	492	184	670	14	41	1	601	83	6.8
	8.2	413	58	451	17	66	1	299	170	7.8
	9.3	306	69	306	35	98	1	110	231	14.8
	9.3	307	69	308	36	98	0	112	232	16.3
	9.7	402	69	274	15	83	1	169	120	7.7
	10.6	356	61	281	25	87	0	129	180	12.6
	8.7	474	212	484	15	44	1	413	86	4.4
281k	12.1	273	91	204	37	113	0	121	121	22.8
	10.2	378	63	284	21	84	1	146	159	7.8
	11.4	302	78	247	36	98	0	116	167	16.1
	9.5	424	57	420	16	59	0	287	149	4.5
	11.1	323	68	269	32	92	0	109	192	13.7
	8.9	446	103	482	15	54	0	375	122	4.1
	8.6	507	293	700	18	35	0	647	71	3.7
	10.6	356	59	289	24	84	0	132	181	12.1

\*The space velocity(SV) of the exhaust is calculated at actual temperature and pressure and is calculated using equation 3.1.

Figure 3.2 shows a plot of the experimental  $CO$  ,  $NO$  and  $HC$  conversion efficiencies for the three space velocities plotted against temperature in  $^{\circ}C$  along the x axis. The conversion efficiencies for  $162\text{ }khr^{-1}$  are plotted in red 'X',  $235\text{ }khr^{-1}$  space velocities are plotted in green 'X' and  $281\text{ }khr^{-1}$  are plotted with blue 'X'. The first subplot shows the  $NO$  conversion efficiencies, the plot shows that between  $200 - 350^{\circ}C$  the  $NO$  conversion efficiency decreases with the increasing DOC space velocities. At temperatures higher than  $350^{\circ}C$  data shows similar  $NO$  conversion efficiencies for all space velocities. The second subplot shows the DOC  $CO$  conversion efficiencies plotted as a function of the temperature. It can be observed from the plot that the experimental data shows 100% conversion of  $CO$  across the DOC for all temperatures. The third subplot shows the  $HC$  conversion efficiencies as a function of temperature. The plot shows that the  $HC$  conversion efficiencies for 235 and  $281\text{ }khr^{-1}$  space velocities are similar. Compared to the  $162\text{ }khr^{-1}$  space velocity,  $HC$  conversion efficiencies for both 235 and  $281\text{ }khr^{-1}$  shows lower conversion efficiencies.

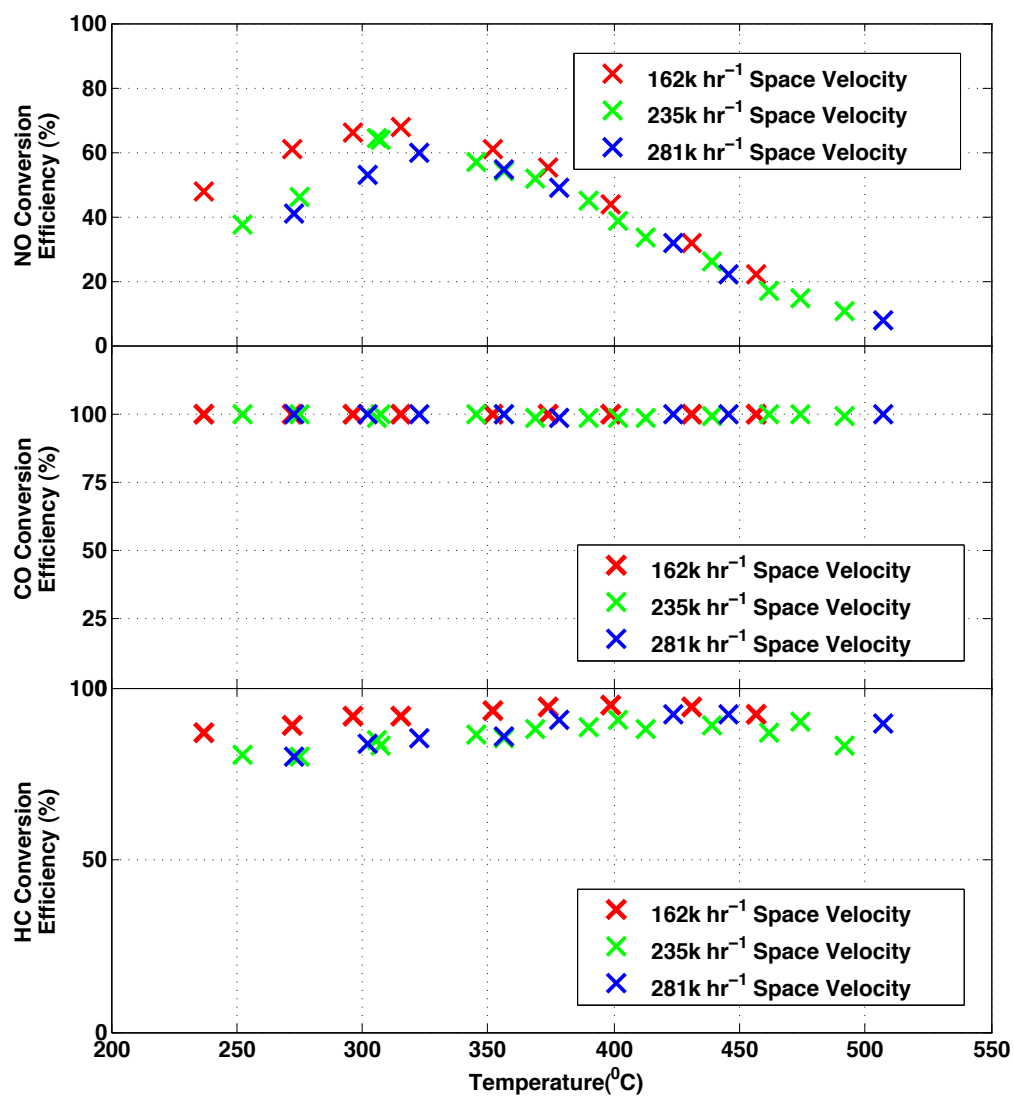


**Figure 3.2.** Experimental measured DOC conversion efficiencies of *NO* , *CO* and *HC* during steady state conditions at three DOC inlet space velocities

### 3.2.2 DOC Active Regeneration Data

The active regeneration condition in the DOC represents a special case in the operation of the DOC. The active regeneration condition exposes the DOC to high temperatures and high concentration of  $HC$ s. The high  $HC$  concentrations in the exhaust results in the inhibition of the other reactions in the DOC. To capture the effects of the high temperature and high  $HC$  concentrations in the exhaust, three data points from the steady state testing test matrix were selected. The test conditions were selected such that the DOC inlet temperature was above  $320^{\circ}C$ . This was done to ensure the DOC light off for the  $HC$  oxidation reaction was achieved. At each of these conditions the  $HC$  injection (post injection in the cylinder) was varied to achieve different DOC inlet  $HC$  concentrations and DOC outlet temperatures. The DOC inlet and outlet  $CO$ ,  $NO$ ,  $NO_2$  and  $HC$  concentrations and temperatures were measured using the mass spectrometer emission measurement instrument described in Figure 3.1. Table 3.4 shows the tabulated values of DOC inlet and outlet concentrations and temperatures for the three space velocities. In the table the  $CO$ ,  $NO$  and  $NO_2$  concentration are in  $ppm$ , the  $HC$  concentrations are in  $ppmC$  and the temperatures are in  $^{\circ}C$ . From the table it can be observed that the DOC inlet concentration of  $CO$ ,  $NO$  and  $NO_2$  and DOC inlet temperatures are constant, while the the DOC inlet  $HC$  concentration is varied depending on the desired DOC outlet temperature.

**Table 3.4**

Test matrix for the active regeneration tests showing the DOC inlet and outlet  $CO$ ,  $NO$ ,  $NO_2$  and  $HC$  concentrations and the DOC inlet temperatures and space velocities. The  $HC$  injection was achieved through in cylinder post injection

SV	Inlet					Outlet				
$hr^{-1}$	$T_{in}$ $^{\circ}C$	CO ppm	NO ppm	$NO_2$ ppm	HC $ppm_C$	$T_{out}$ $^{\circ}C$	CO ppm	NO ppm	$NO_2$ ppm	HC $ppm_C$
162k	344	83	499	18	132	348	0	183	334	16
	344	83	499	18	8340	497	3	481	36	305
	344	83	499	18	9896	526	4	497	20	319
	344	83	499	18	11021	547	6	507	10	313
	344	83	499	18	13620	599	12	517	0	330
235k	344	71	296	13	185	350	0	124	185	18
	344	71	296	16	7875	504	12	305	7	468
	344	71	296	16	9069	524	17	307	5	516
	344	71	296	27	10791	548	23	320	3	930
	344	71	296	33	14259	615	75	325	4	1104
281k	320	75	285	21	215	326	0	130	175	34
	320	75	285	24	10550	509	58	301	8	1323
	320	75	285	27	11687	533	65	306	6	1426
	320	75	285	30	12936	557	80	310	5	1550
	320	75	285	34	15199	597	140	312	7	1695

Figure 3.3 shows the plot of the experimental  $NO$ ,  $CO$  and  $HC$  conversion efficiencies plotted against the DOC outlet temperature. The conversion efficiencies for  $162khr^{-1}$  are plotted in red 'X',  $235khr^{-1}$  are plotted in green 'X' and  $281khr^{-1}$  are plotted with blue 'X'. The conversion efficiencies between temperatures of  $300 - 350^{\circ}C$  indicate the  $NO$  conversion efficiencies without  $HC$  injection. The conversion efficiencies at temperatures higher than  $500^{\circ}C$  show conversion efficiencies with  $HC$  injection. The first subplot shows the  $NO$  conversion efficiencies plotted against the DOC outlet temperature. The plot shows that at temperatures greater than  $500^{\circ}C$  the  $NO$  conversion efficiency shows negative values indicating the conversion of  $NO_2$  to  $NO$ . The second plot shows the  $CO$

conversion efficiencies of DOC plotted against DOC outlet temperature. It can be observed from the plot that the *CO* conversion efficiency decreases with a increase in the DOC inlet *HC* concentration. The  $281\text{ khr}^{-1}$  space velocity *CO* conversion efficiency shows negative conversion at temperatures greater than  $550^{\circ}\text{C}$ . The negative *CO* conversion indicates the production of *CO* across the DOC. The third subplot shows *HC* conversion efficiencies plotted against the DOC outlet temperatures. The plot shows that for the temperatures tested, the HC conversion efficiency remains more than 80% and there is no significant difference between the *HC* conversion for three space velocities.

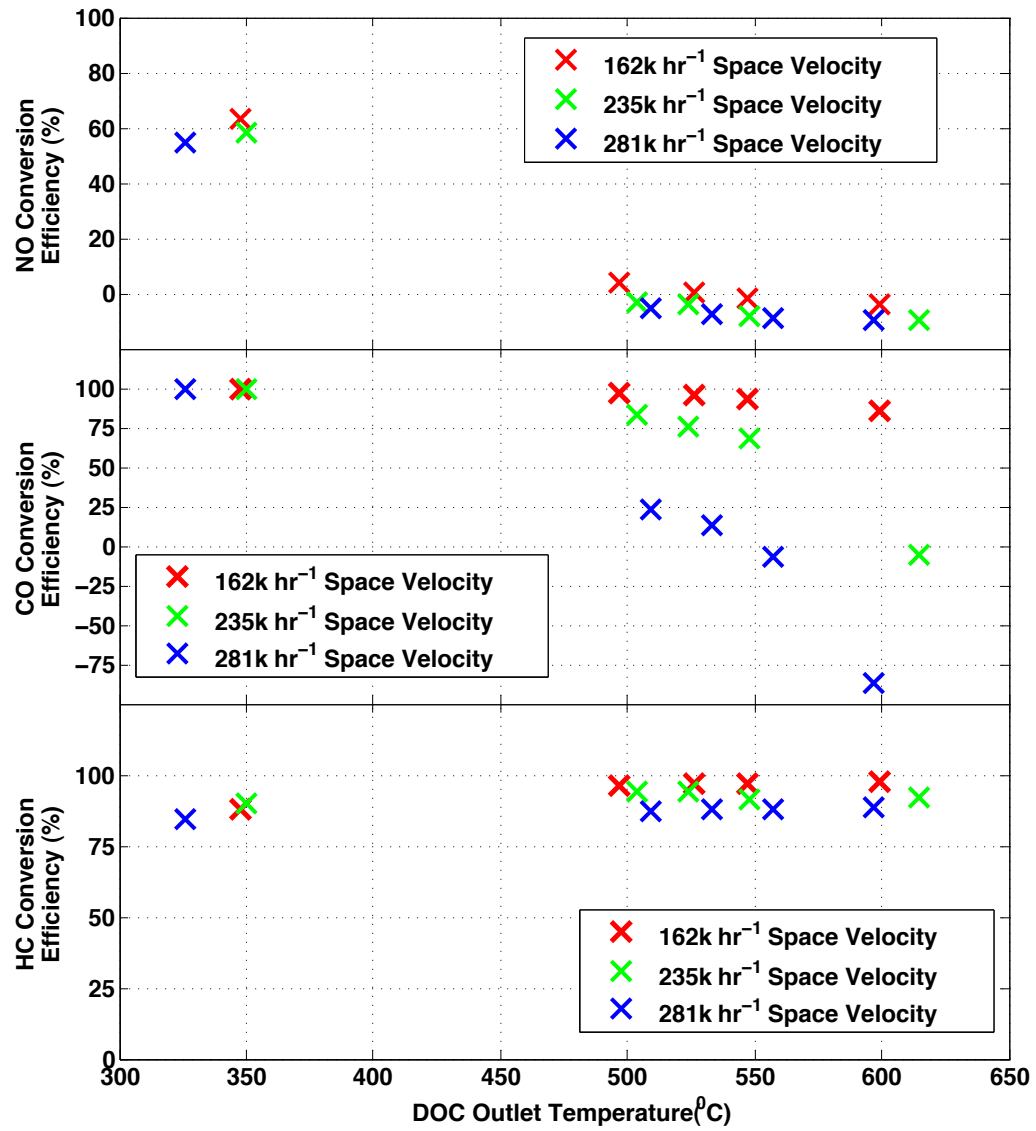


**Figure 3.3.** Experimental measured DOC conversion efficiencies of *NO* , *CO* and *HC* during active regeneration conditions at three DOC inlet space velocities

### 3.2.3 DOC Transient Data

To understand the transient performance of the DOC, a surrogate FTP cycle based on a standard Heavy-Duty FTP cycle was developed[53]. The surrogate FTP cycle captures the important transient features of the standard FTP cycle. But eliminates the speed load points that are beyond the capability of the test cell.

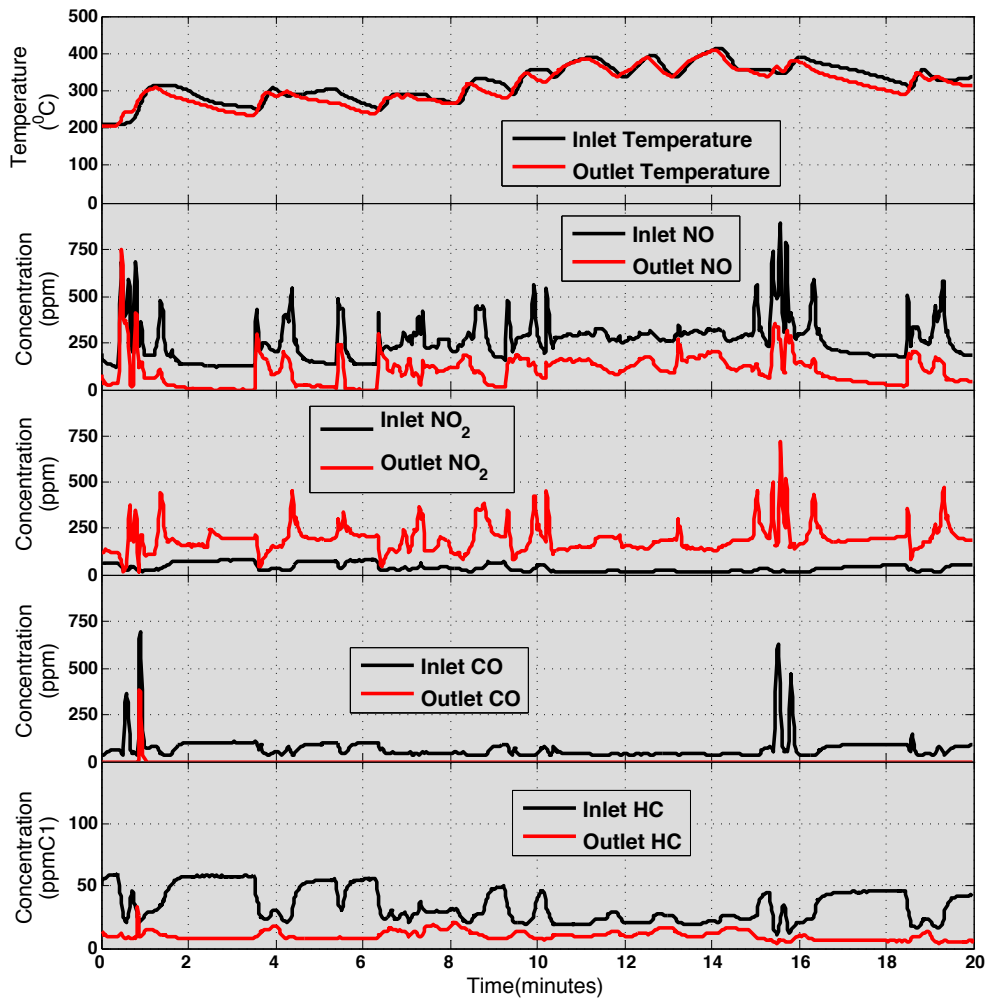


**Figure 3.4.** Experimental measured DOC inlet and outlet concentrations of  $NO$ ,  $CO$  and  $HC$  and temperatures during transient test



Figure 3.4 shows the DOC inlet and outlet concentrations of  $NO$  ,  $NO_2$  ,  $CO$  and  $HC$  and the temperatures during the transient FTP test. In the figure, the curves in black represents the DOC inlet concentrations and temperatures and the curves in red represent the DOC outlet concentrations and temperatures. The first subplot shows the DOC inlet and outlet temperature in  $^{\circ}C$  plotted as a function of time in minutes along the x axis. It can be observed that the DOC inlet and outlet temperatures vary from 200 to 405 $^{\circ}C$  and consist of regions where the DOC inlet temperature increases and decreases, which simulates the heating and cooling of the DOC. The second subplot shows the DOC inlet and outlet  $NO$  concentrations in  $ppm$  plotted against time in minutes along the x axis. It can be observed that the DOC inlet  $NO$  concentrations vary from 0 to 770  $ppm$ . The  $NO$  concentrations show fast transients where the inlet concentrations change from greater than 700 $ppm$  to less than 100  $ppm$ . The third subplot shows the DOC inlet and outlet  $NO_2$  concentrations in  $ppm$  plotted against time in minutes along the x axis. Compared to the DOC inlet  $NO$  concentration the DOC inlet  $NO_2$  concentration is much lower which indicates that most of the engine out  $NO_x$  is composed of  $NO$  . The DOC outlet  $NO_2$  concentration profile is higher than the DOC inlet  $NO_2$  concentration which represents the oxidation of  $NO$  to  $NO_2$  across the DOC. The fourth subplot shows the DOC inlet and outlet  $CO$  concentration in  $ppm$  plotted against time in minutes along the x axis. The DOC inlet  $CO$  concentration does not change and remains constant except for the spikes observed at 1 minute and between 15 and 16 minutes. For the entire test, the DOC outlet  $CO$  shows almost 100% conversion of  $CO$  across the DOC except at 1 minute. The fifth subplot shows the DOC inlet and outlet  $HC$  concentrations in  $ppmC$  plotted against time in minutes along the x axis. The DOC inlet  $HC$  concentration is less than 50  $ppmC$  for the entire test. The DOC outlet  $HC$  is less than 10  $ppmC$  which shows that for the entire test conditions the DOC light off is achieved.

The DOC high fidelity model was simulated using the steady state, active regeneration and transient data. The DOC reduced order model was simulated on steady state and active regeneration data and the reduced order DOC estimator was simulated on the transient FTP data.

### 3.3 SCR Test Data

To simulate and validate the SCR reduced order model and reduced order estimator, steady state and transient tests were conducted. Both the data sets were generated on a 2010 Cummins ISB engine with a 2010 Cummins production aftertreatment system. This section briefly describes the experimental data for the SCR tests. More detailed analysis of the data and details on the test setup can be found in the reference[1].

#### 3.3.1 SCR Steady State Data

The objective of the SCR steady state tests was to identify the kinetic parameters to simulate the SCR on an engine. The steady state data was collected at 8 different SCR inlet temperatures. The engine speed and load points were selected to achieve different SCR inlet temperatures and  $NO_2/NO_X$  ratios. Table 3.5 shows the test matrix for the light test points for the steady state tests. The SCR inlet temperatures were varied from  $250 - 299^{\circ}C$ . At each of the SCR inlet temperatures, the inlet  $NO$  and  $NO_2$  concentrations were maintained constant. For the eight tests the SCR inlet  $NO$  and  $NO_2$  concentration varied between 78 to 462  $ppm$  and 120 to 295  $ppm$  respectively. During each of these tests, different  $NH_3/NO_X$  ratios were achieved by varying the urea injection rate.

**Table 3.5**

Test matrix for the SCR steady state tests showing the SCR inlet  $NO$ ,  $NO_2$  and  $NH_3$  concentrations along with the SCR inlet temperatures

Test Point	SCR inlet Temp	SCR SV	SCR Inlet $NO$	SCR Inlet $NO_2$
	C	$kg\,hr^{-1}$	ppm	ppm
1	399	58.9	462	295
2	376	60.1	185	160
3	353	61.5	115	187
4	331	59.8	97	176
5	301	60.6	78	220
6	278	60.8	80	199
7	252	60.2	110	120
8	366	53.5	197	208

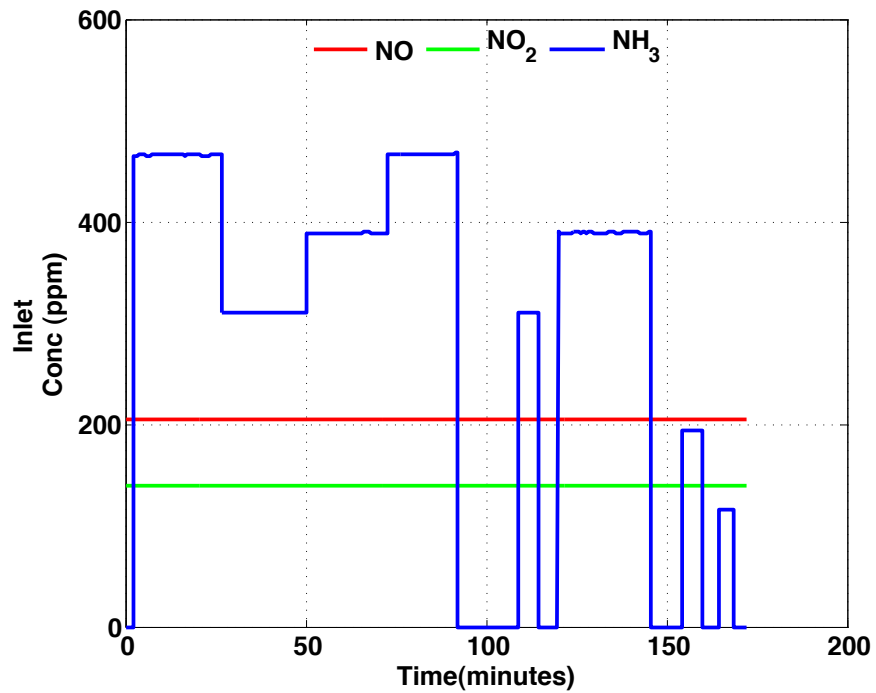


**Figure 3.5.** Experimental measured SCR inlet concentrations of  $NO$ ,  $NO_2$  and  $NH_3$  during steady state test

Figure 3.5 shows the SCR inlet concentrations of  $NO$ ,  $NO_2$  and  $NH_3$  plotted against time for test number 8. The plot shows that the SCR inlet  $NO$  and  $NO_2$  concentrations are maintained constant for the entire test and the SCR inlet  $NH_3$  concentration varies to achieve different SCR inlet  $NH_3 / NO_x$  ratios. The SCR inlet  $NH_3$  concentrations are calculated using the DEF injector flow rate, urea properties and the exhaust flow rate. More details on the  $NH_3$  concentration calculation can be found in Appendix A. More detailed analysis of the data and details on the test setup can be found in the reference[1].

### 3.3.2 SCR Transient Data

To simulate the SCR transients, the surrogate FTP test was created [1]. The surrogate FTP test is based on a standard heavy duty FTP test. The standard heavy duty FTP test was modified to remove some of the test conditions which are beyond the capability of the test cell. Figure 3.6 shows the SCR inlet  $NO$ ,  $NO_2$  and  $NH_3$  concentrations and the SCR inlet and outlet temperatures during the surrogate FTP test. The first subplot shows the SCR inlet  $NO$ ,  $NO_2$  and  $NH_3$  concentrations plotted against time in minutes. The plots show that the inlet concentrations show fast transients similar to the standard FTP cycle. The second subplot shows a plot of the SCR inlet and outlet temperatures against time in minutes. The SCR inlet temperature varies from 250 to 375<sup>0</sup>C. The plot also shows that the SCR inlet and outlet temperature profiles are similar but the SCR outlet temperature lags the inlet temperature.

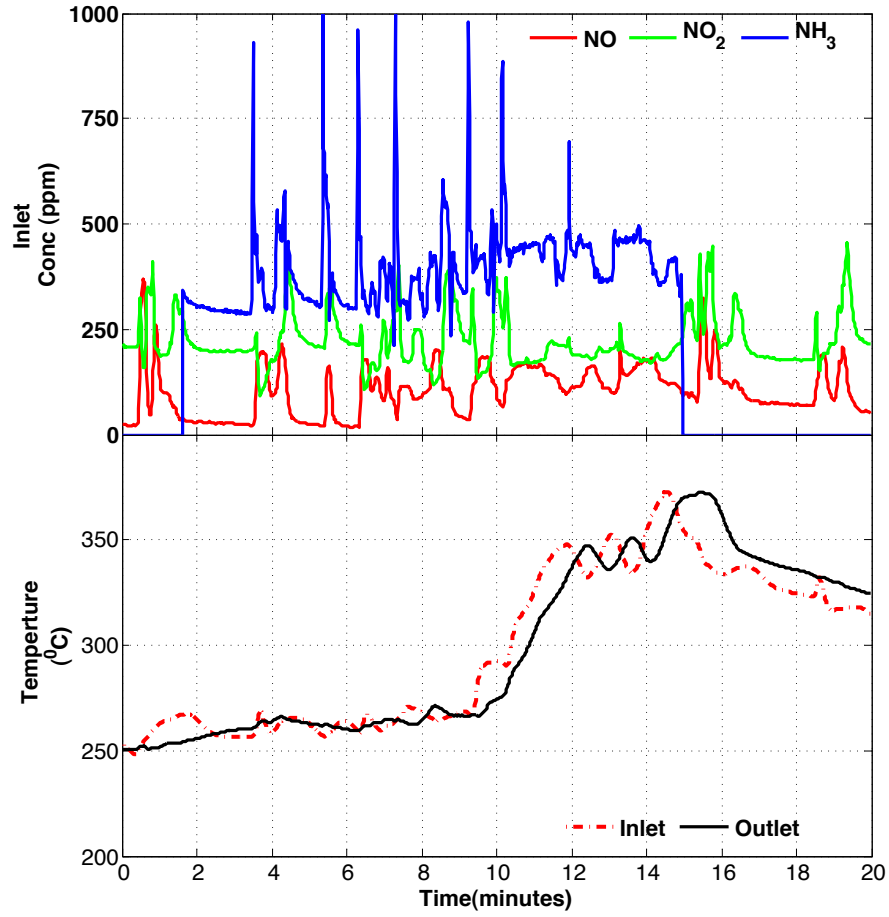


**Figure 3.6.** Experimental measured SCR inlet concentrations of  $NO$  ,  $NO_2$  and  $NH_3$  and the SCR inlet and outlet temperatures during surrogate FTP test

The SCR steady state test data were used to compare to the reduced order model simulation and the transient test data were used to compare to the SCR reduced order estimator simulation.

## 4. DOC AND SCR HIGH FIDELITY MODELS

Aftertreatment system modeling has been used in the design process to improve the performance and to reduce the cost of the system including the development cost and to understand the performance characteristics of these systems. The 1D single channel modeling approach is the most commonly used approach, since 3D and 2D modeling of an aftertreatment system is very complex and requires significant computational resources. The 1D modeling approach requires less computational resources and is still relatively accurate. This section describes the 1D modeling approach as applied to the DOC and SCR aftertreatment devices as used in the dissertation.

### 4.1 DOC High Fidelity Model

The DOC model developed for this dissertation is a 1D single square channel approximation of the DOC. The DOC model simulates three important reactions for  $CO$ ,  $HC$  and  $NO$  oxidation[28–30,54,55]. The DOC model assumes that a single channel can be used to represent a DOC and simulates the gas and surface phase mass and energy balance equations. The heat and mass transfer between the gas and surface phase are limited by the heat and mass transfer coefficients. The important assumptions made in the development of the

DOC model are:

1. Exhaust gas is assumed to be ideal.
2. Reaction rate constants are of the Arrhenius form.
3. Convection heat transfer is assumed to ambient .

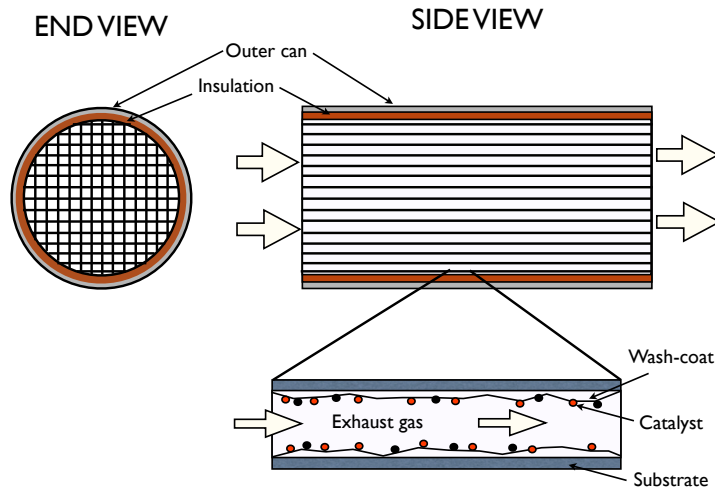


**Figure 4.1.** Schematic showing the exhaust flow through the DOC

#### 4.1.1 Reactions in the DOC

The DOC model simulates the oxidation of  $CO$ ,  $NO$  and  $HC$  in the exhaust.  $HC$  and  $CO$  oxidation are considered as forward only reactions and  $NO$  oxidation is considered as a reversible reaction. The  $NO \leftrightarrow NO_2$  oxidation is a reversible reaction which is kinetics limited at low temperatures and thermodynamically limited at higher temperatures[28–30, 55].  $NO \leftrightarrow NO_2$  equilibrium is used to determine the direction of the  $NO$  oxidation reaction and is based on the Gibbs free energy function[28–30, 55]. Some modeling studies such as OH et al[56] have used  $C_3H_6$  to represent fast oxidizing hydrocarbons and  $CH_4$

methane to represent the slow oxidizing hydrocarbons. But several research studies [28–30,55,57,58] involving modeling of the DOC have concluded that  $C_3H_6$  is sufficient to represent the exhaust of a heavy duty diesel engine. Hence, in the DOC model used in this study,  $C_3H_6$  is considered to be a representative hydrocarbon in the DOC. This reduces the number of differential equations to be solved in the model and improves the speed of the model. The reactions considered in the model are shown below:

NO oxidation:



CO oxidation:



Hydrocarbon oxidation:

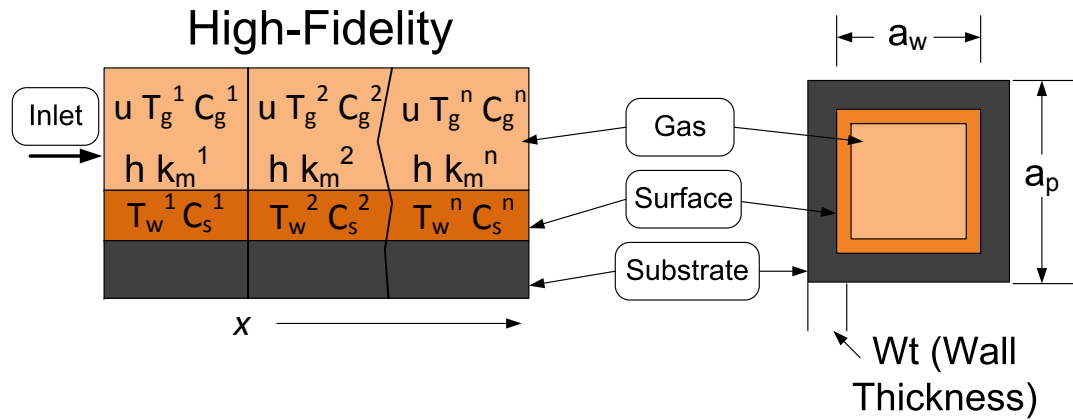
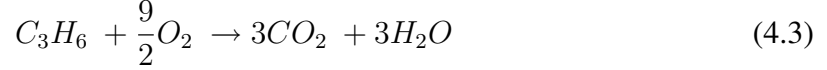


**Figure 4.2.** Schematic of the DOC high fidelity model showing the gas and surface phase concentrations and temperatures



#### 4.1.2 Mass and Energy Balance Equations

The species balance equations for  $CO$ ,  $NO$ ,  $NO_2$  and  $C_3H_6$  are represented as:

$$\epsilon \frac{\partial C_{g,i}}{\partial t} = -\epsilon u \frac{\partial C_{g,i}}{\partial x} - \beta_i A_g (C_{g,i} - C_{s,i}) \quad (4.4)$$

$$(1 - \epsilon) \frac{\partial C_{s,i}}{\partial t} = -\beta_i A_g (C_{s,i} - C_{g,i}) - R_i \quad (4.5)$$

$i = CO, NO, NO_2, C_3H_6$

Where,  $C_{g,i}$  and  $C_{s,i}$  are the gas and surface concentration of  $i^{th}$  species,  $\epsilon$  is the void fraction and  $u$  is the exhaust gas velocity. The energy balance equation is represented as:

$$\rho C_v \frac{\partial T_g}{\partial t} = -\rho u C_p \frac{\partial T_g}{\partial t} - h_g \frac{4}{a_w} (T_g - T_w) \quad (4.6)$$

$i = CO, NO, NO_2, C_3H_6$

$$(\rho_s c_{p,s}) \frac{\partial T_w}{\partial t} = h_g \frac{4a_w}{a_p^2 - a_w^2} (T_g - T_w) - h_a \frac{4a_p}{a_p^2 - a_w^2} (T_g - T_w) + \frac{A_g}{1 - \epsilon} \sum_{i=CO}^{HC} \frac{\Delta h_i r_i}{MW_i} \quad (4.7)$$

Where,  $T_g$  and  $T_w$  are the gas and substrate temperatures,  $h_g$  and  $h_a$  are the heat transfer coefficients between gas and surface phase and the between the outer surface of the channel and the atmosphere,  $\rho_s$  and  $c_{p,s}$  are the density and specific heats,  $\rho$  is the density of the exhaust gas,  $c_p$  and  $c_v$  are specific heats of the exhaust gas,  $\Delta h_i$  is the enthalpy of the  $CO$ ,  $NO$  and  $C_3H_6$  oxidation reactions,  $MW_i$  is the molecular weight of  $i^{th}$  species and  $A_g$  is the geometric surface area. The heat transfer to the ambient is an empirical approximation. The reaction rate for the  $CO$ ,  $NO$  and  $C_3H_6$  oxidation reactions are defined as:

$$r_{CO} = \frac{k_{CO,s} c_{CO,s} c_{O_2}}{G_1} \quad (4.8)$$

$$r_{NO} = \frac{k_{NO} \left( c_{NO,s} c_{O_2}^{0.5} - \frac{c_{NO_2,s}}{K_p} \right)}{G_2} \quad (4.9)$$

$$r_{C_3H_6} = \frac{k_{C_3H_6} c_{C_3H_6} c_{O_2}}{G_3 G_4} \quad (4.10)$$

where  $k_{CO}$ ,  $k_{NO}$  and  $k_{C_3H_6}$  are the Arrhenius reaction rate constants given by Eq. 4.11.

$$k_i = A_i e^{-(E_i/RT_w)} \quad (4.11)$$

$$i = CO, NO, NO_2, C_3H_6$$

where the  $A_i$  are the pre exponential factors,  $E_i$  are the activation energies and  $T_s$  is the substrate temperature. The quantity  $K_p$  is the thermodynamic equilibrium constant and is calculated as:

$$K_p = \frac{RT_s e^{-(\Delta G/RT_s)}}{P} \quad (4.12)$$

where,  $\Delta G$  is the Gibbs free energy for a mixture of  $NO$ ,  $NO_2$  and  $O_2$  at temperature  $T_s$ ,  $R$  is the universal gas constant and  $P$  is exhaust gas pressure.  $G_1$ ,  $G_2$ ,  $G_3$  and  $G_4$  are the inhibition terms to account for the inhibition of the oxidation reactions due to the availability of catalyst sites.

$$G_1 = G_2 = G_3 = (1 + K_{a,1} C_{s,CO} + K_{a,2} C_{s,C_3H_6})^2 (1 + K_{a,3} C_{s,CO}^2 C_{s,C_3H_6}^2) + K_{a,4} C_{s,NO}^{0.7}$$

$$G_4 = (1 + K_{a,5} C_{s,O_2})^{1.5} \quad (4.13)$$

Where  $K_{a,j}$  are of the Arrhenius form and are called inhibition factors:

$$K_{a,j} = A_{a,j} e^{\frac{\Delta H_{a,j}}{RT_s}} \quad (4.14)$$

$$j = 1, 2, \dots, 5$$

Where,  $A_{a,j}$  are the adsorption constants and  $\Delta H_{a,j}$  are the adsorption heats.

#### 4.1.3 High Fidelity Model Calibration

The DOC high fidelity model was simulated using the steady state and active regeneration data. The steady state data were used to identify the activation energies for  $CO$ ,  $NO$  and  $HC$  oxidation reactions and the active regeneration data were used to identify the inhibition factors during active regeneration with diesel fuel being injected into the cylinder later in the expansion stroke. The activation energies reported in the reference [1] were used as initial values.

#### 4.1.4 Steady State Simulation

The steady state data consists of  $CO$ ,  $NO$  and  $HC$  concentrations upstream and downstream of the DOC at DOC inlet temperatures from 237 to 507°C at three different space velocities of 162, 235 and 281  $kg/hr^{-1}$ . The steady state data provides the data needed to identify the activation energies and pre exponential factors for the  $CO$ ,  $NO$  and  $HC$  oxidation reactions.

To identify the activation energies and pre exponential factors, the adsorption factors in the inhibition terms were set to zero. The activation energies for each of the oxidation reactions were changed to simulate the shape of the conversion efficiency curves. Table 4.1 contains the kinetic parameters used in simulating the steady state data. As mentioned earlier, the inhibition factors were set to zero.

**Table 4.1**  
Kinetic parameters used to simulate steady state conditions

	CO Oxidation		HC Oxidation		NO Oxidation	
Activation Energy	894000.0		10000.0		715000.0	
Preexponential Factor	39.0		25.0		46.4	
Inhibition	$A_{a,j}$	$\Delta H_{a,j}$	$A_{a,j}$	$\Delta H_{a,j}$	$A_{a,j}$	$\Delta H_{a,j}$
$A_{a,1}$	0.0	7990.0	0.0	7990.0	0.0	7990.0
$A_{a,2}$	0.0	75000.0	0.0	3000.0	0.0	75000.0
$A_{a,3}$	0.0	96534.0	0.0	96534.0	0.0	96534.0
$A_{a,4}$	0.0	31036.0	0.0	31036.0	0.0	31036.0
$A_{a,5}$	0.0	0.0	0.0	0.0	0.0	0.0

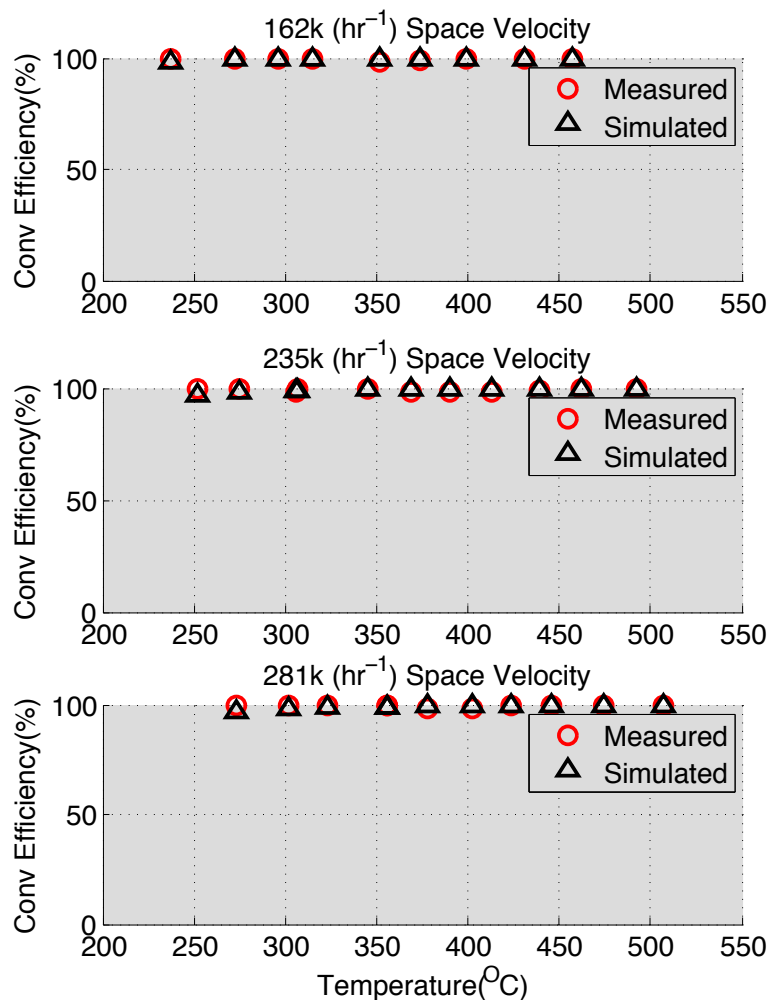
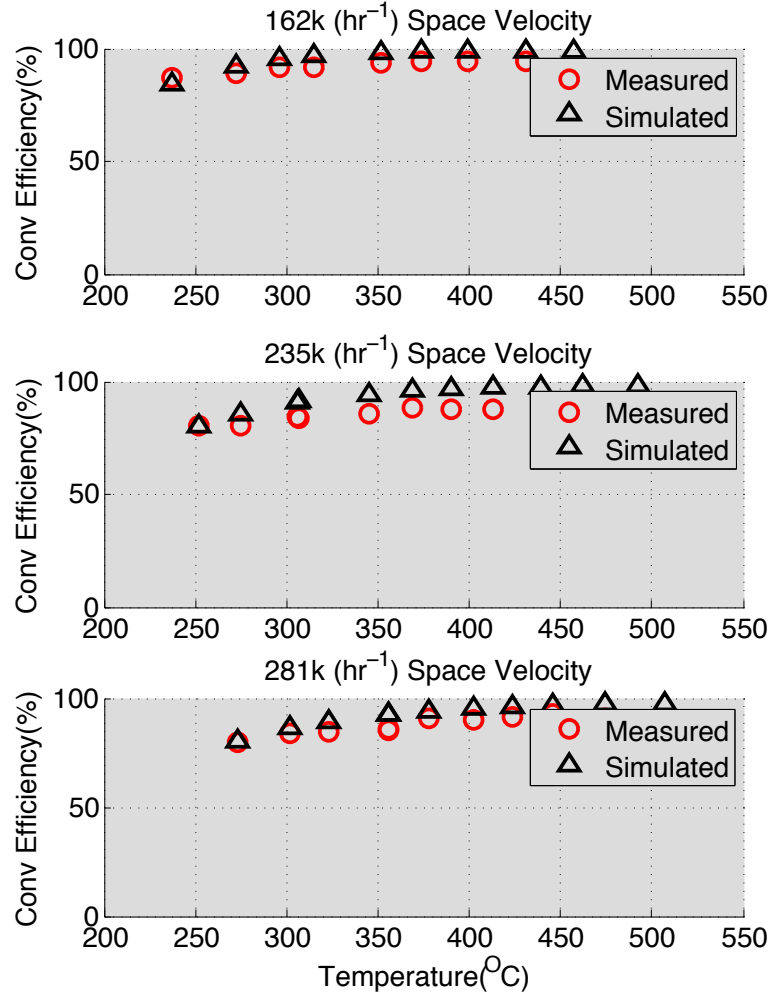


**Figure 4.3.** Comparison of the simulated and experimental DOC  $CO$  conversion efficiencies

Figure 4.3 shows the comparison of the experimental and simulated  $CO$  conversion efficiency for 162, 235 and 281  $hr^{-1}$  space velocities. The experimental (measured)  $CO$  conversion efficiencies are plotted with symbol 'O' in red and the simulated  $CO$  conversion efficiencies are plotted with symbol ' $\Delta$ ' in black. The experimental  $CO$  conversion efficiency was more than 99% for all the temperatures. Hence, to simulate the conversion efficiency profile, the activation energy used to simulate the model was lowered to 39  $J/kmol$  for the  $CO$  oxidation reaction. With the lower activation energy, the model is able

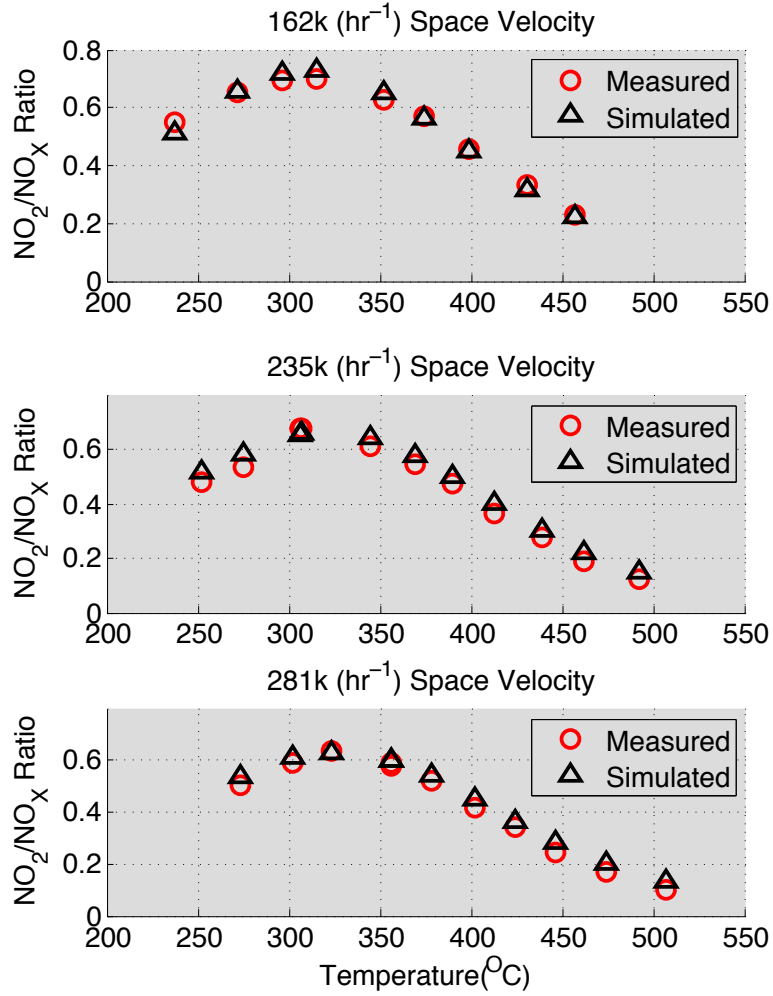
to simulate the experimental  $CO$  conversion efficiencies observed in the experimental data.

Figure 4.4 shows the comparison of the experimental and simulated  $HC$  conversion efficiencies for 162, 235 and  $281\text{ }khr^{-1}$  space velocities. The experimental (measured)  $HC$  conversion efficiencies are plotted with symbol 'O' in red and the simulated  $HC$  conversion efficiencies are plotted with symbol ' $\Delta$ ' in black. At  $235\text{ }khr^{-1}$  space velocity, the experimental data shows a decrease in conversion efficiency with increasing temperature. This trend is not seen in the other space velocities and when the measurement uncertainty of  $\pm 5\text{ }ppmC$  is considered, it can be concluded that the trend is not a real phenomenon. The experimental  $HC$  conversion efficiency curve shows more than 98% conversion efficiency for temperatures above  $350^{\circ}C$ . To simulate the conversion efficiency profile, the activation energy used to simulate the model was lowered to  $25\text{ }J/kmol$  for the  $HC$  oxidation reaction. With the lower activation energy, the model is able to simulate the experimental  $HC$  conversion efficiencies.



**Figure 4.4.** Comparison of the experimental and simulated HC conversion efficiencies

Figure 4.5 shows a comparison of the simulated and experimental DOC outlet  $NO_2/NO_X$  ratios for three space velocities. The  $NO_2/NO_X$  ratio is plotted as a function of temperature along the x axis. The experimental (measured)  $NO_2/NO_X$  ratios are plotted with symbol 'O' in red and the simulated  $NO_2/NO_X$  ratios are plotted with symbol 'Δ' in black. With the activation energy of 46.4 J/kmol, the model follows the shape of the experimental  $NO_2/NO_X$  ratio. There are slight differences in the  $NO_2/NO_X$  ratios at a given temperature, but these differences fall within the limits of measurement uncertainty.



**Figure 4.5.** Comparison of the simulated and experimental DOC outlet  $NO_2/NO_X$  ratio

#### 4.1.5 Active Regeneration Simulation

The active regeneration data consists of in cylinder  $HC$  dosing which results in increased  $HC$  concentrations at the inlet of the DOC. The data consists of  $HC$ ,  $NO$  and  $CO$  conversion across the DOC at three space velocities and different  $HC$  injection levels and corresponding DOC outlet temperatures. The important difference between the steady



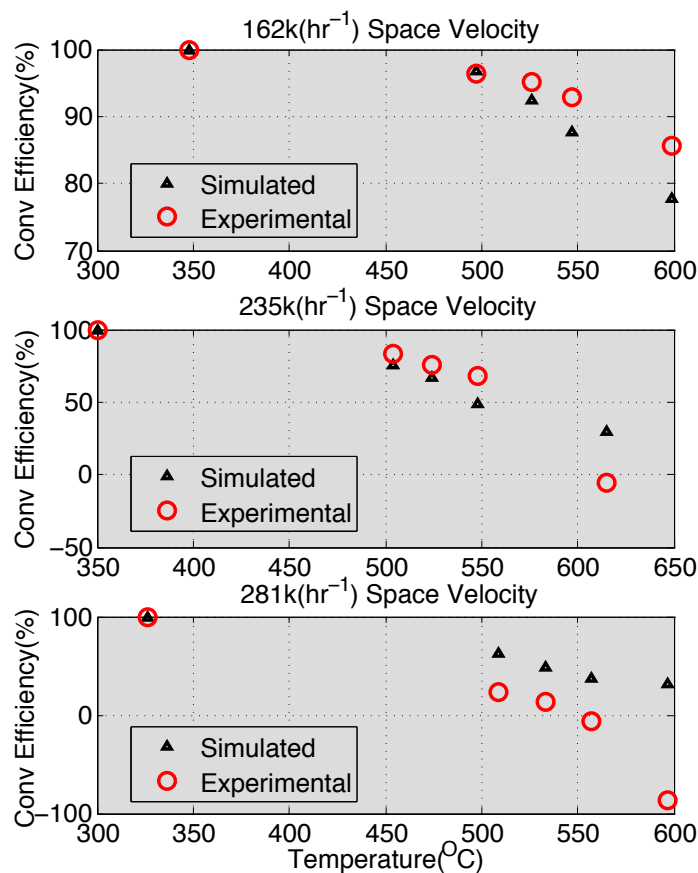
**Table 4.2**  
Kinetic parameters used to simulate active regeneration

	CO Oxidation		HC Oxidation		NO Oxidation	
Preexponential Factor	894000.0		10000.0		715000.0	
Activation Energy	39.0		25.0		46.4	
Inhibition	$A_{a,j}$	$\Delta H_{a,j}$	$A_{a,j}$	$\Delta H_{a,j}$	$A_{a,j}$	$\Delta H_{a,j}$
$A_{a,1}$	0.0	7990.0	0.0	7990.0	0.0	7990.0
$A_{a,2}$	7.0E+07	75000.0	20.5	3000.0	6.8E+08	75000.0
$A_{a,3}$	0.0	96534.0	0.0	96534.0	0.0	96534.0
$A_{a,4}$	0.0	31036.0	0.0	31036.0	0.0	31036.0
$A_{a,5}$	0.0	0.0	0.0	0.0	0.0	0.0

state and active regeneration tests is the presence of high hydrocarbon concentrations and the large temperature increase across the DOC. This provides an opportunity to identify the inhibition factors and adsorption heats for inhibition due to the hydrocarbons affecting the reaction rates. To simulate the DOC outlet species measurements, the inhibition factor associated with the affect of the  $HC$  concentrations on oxidation reactions ( $A_{a,2}$  and  $\Delta H_{a,2}$ ) were changed to simulate the DOC outlet concentrations and temperatures. Table 4.2 contains the kinetic parameters used in simulating the active regeneration data. The main difference from the Table 4.1 is that the inhibition factors are non-zero and are different between HC, CO and NO oxidation reactions.

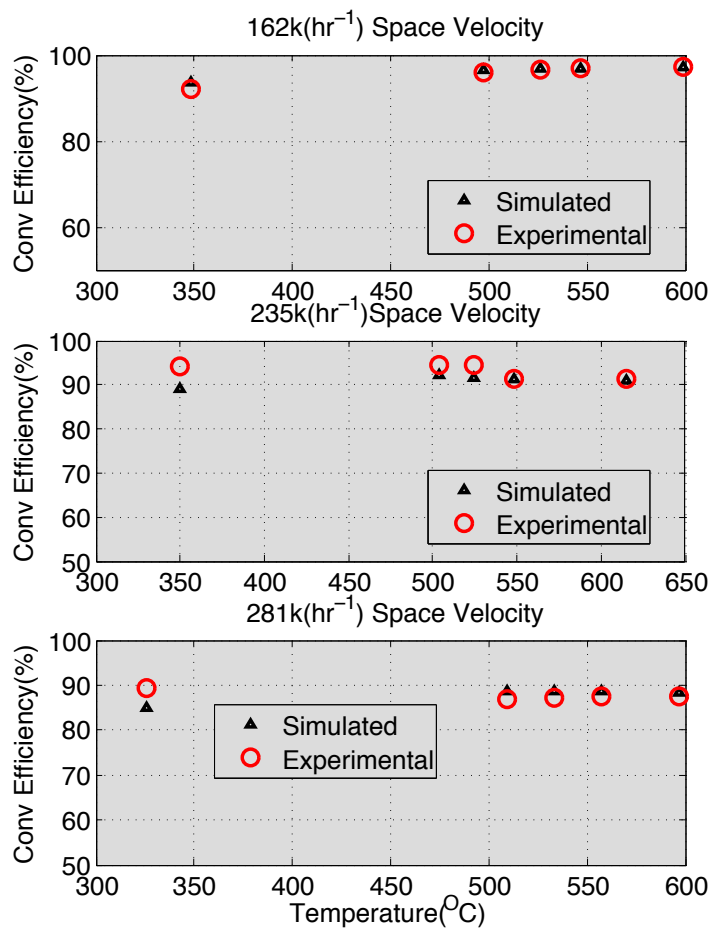
Figure 4.6 shows the comparison of the experimental and simulated DOC  $HC$  conversion efficiencies for 162, 235 and 281  $hr^{-1}$  space velocities. To simulate the DOC outlet CO conversion efficiency, the inhibition factor for  $A_{a,2}$  and adsorption heat  $\Delta H_{a,2}$  were changed to  $6.8 \times 10^{+08}$  and 75000 for the  $CO$  oxidation reaction. With the new values for inhibition, the model is able to simulate the shape of experimental DOC  $CO$  conversion efficiency curve for most of the 162 and 235  $hr^{-1}$  space velocities. The model is not able to simulate the 550°C and higher temperature points and the 281  $hr^{-1}$  space velocity points.

This is due to the presence of  $CO$  production in the DOC from incomplete  $HC$  oxidation and the model does not have the capability to model this phenomenon.



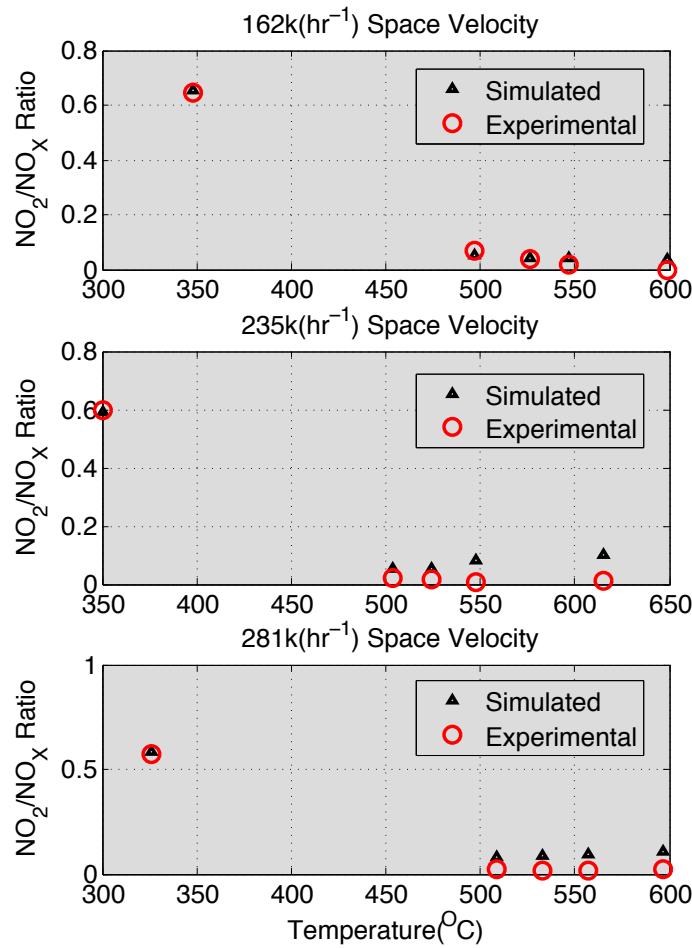
**Figure 4.6.** Comparison of the simulated and experimental DOC  $CO$  conversion efficiencies during active regeneration

Figure 4.7 shows the comparison of the experimental and simulated  $HC$  conversion efficiencies for 162, 235 and  $281khr^{-1}$  space velocities. With the inhibition factor for the  $HC$  inhibition, the model is able to simulate the experimental  $HC$  conversion efficiencies. At temperatures less than  $350^{\circ}C$ , the model predicts lower conversion of  $HC$  across the DOC. But when the measurement uncertainty of  $\pm 5 ppmC$  is considered, the simulated conversion efficiency falls within the error.



**Figure 4.7.** Comparison of the experimental and simulated DOC HC conversion efficiencies during active regeneration

Figure 4.8 shows the comparison of the experimental and simulated DOC outlet  $NO_2/NO_X$  ratios for the 162, 235 and 281  $kh r^{-1}$  space velocities. To simulate the DOC outlet  $NO_2/NO_X$  ratios, the inhibition factor for  $A_{a,2}$  and adsorption heat  $\Delta H_{a,2}$  were changed to  $7.0 \times 10^{+07}$  and 75000 for the NO oxidation reaction. With the new values for the inhibition factor, the model is able to simulate the experimental DOC outlet  $NO_2/NO_X$  ratios.



**Figure 4.8.** Comparison of the simulated and experimental DOC outlet  $NO_2/NO_X$  ratio during active regeneration

Figure 4.9 shows the comparison of the experimental and simulated DOC outlet temperatures for 162, 235 and 281  $kh r^{-1}$  space velocities. To simulate the DOC outlet tem-

perature profile, the inhibition factor for  $A_{a,2}$  was changed to 20.5 for the HC oxidation reaction. With this inhibition factor, the model is able to simulate the experimental DOC outlet temperature.

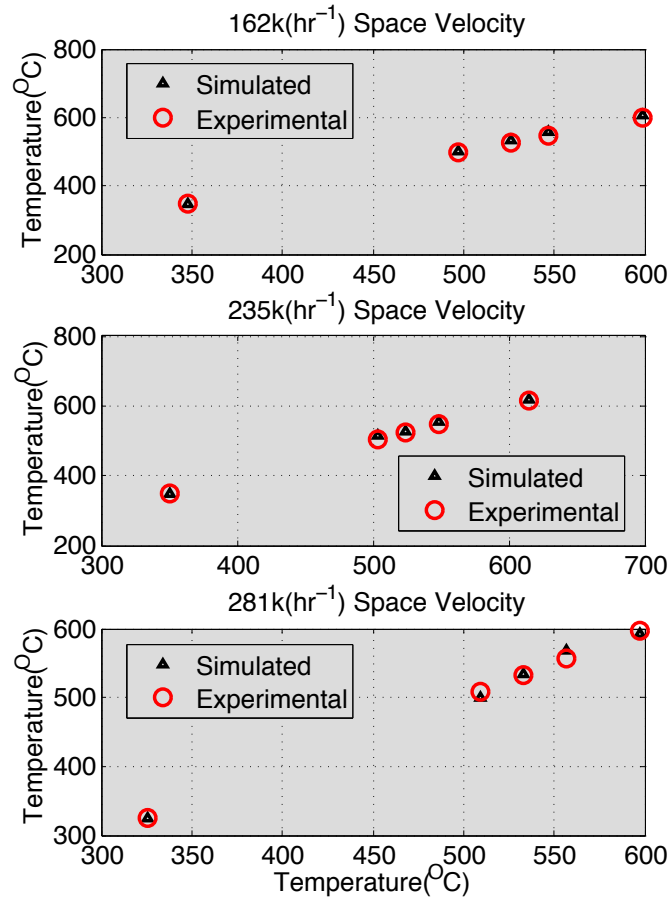


**Figure 4.9.** Comparison of the experimental and simulated DOC outlet temperatures

#### 4.1.6 Transient Simulation

The kinetic constants tabulated in Table 4.2 were used to simulate the transient FTP data. From the initial simulation results, it was observed that there was a lag in the response of simulated DOC outlet temperature compared to the experimental DOC outlet tempera-

tures. To improve the thermal response of the DOC model, the density of the substrate( $\rho_{s,i}$ ) was reduced. However, the resulting effect of reduced density of the substrate was not sufficient to simulate the experimental temperature. To simulate the experimental DOC outlet temperature, the heat transfer coefficient to ambient was set to ' $h_a = 0.11 \frac{W}{m^2.K}$ '.

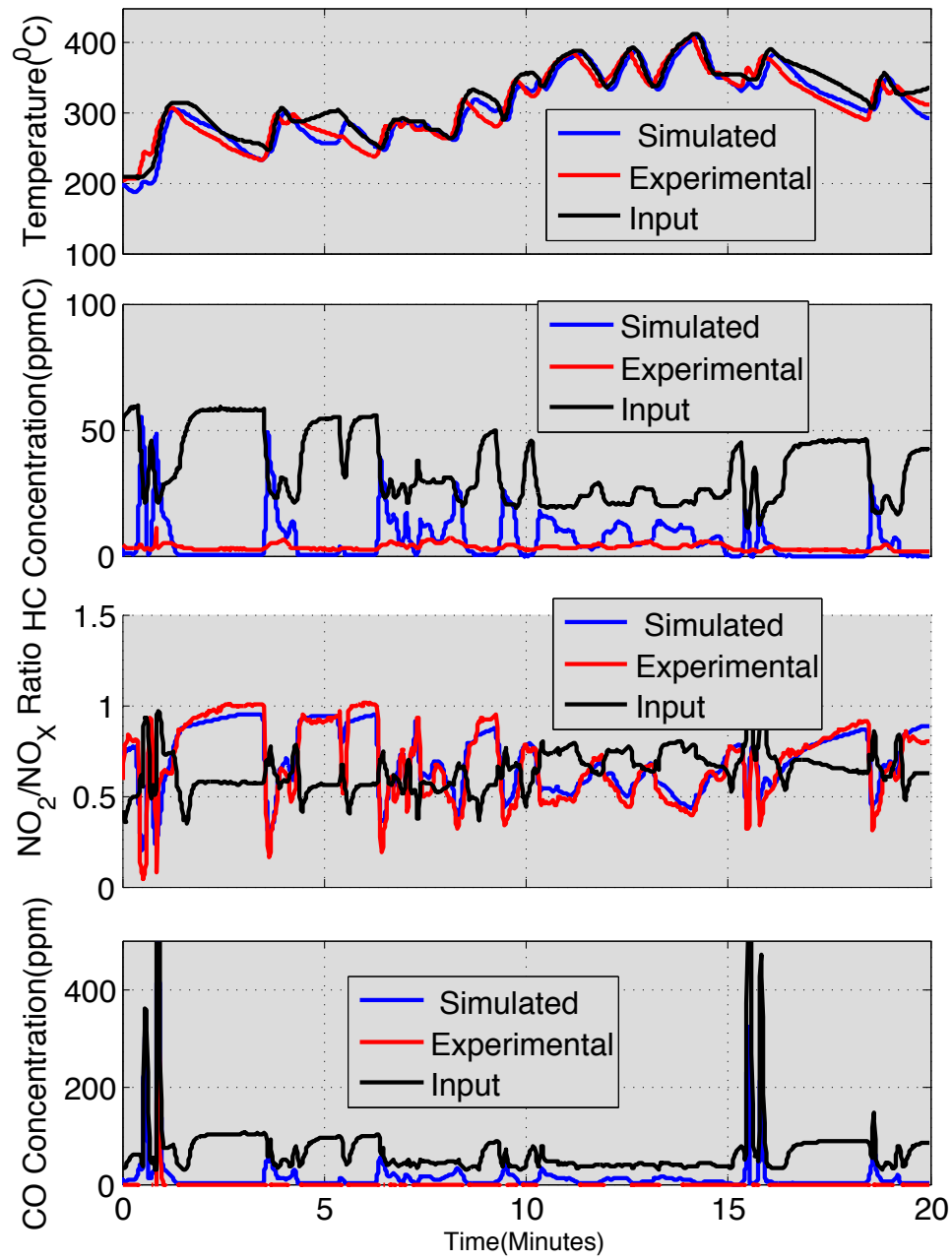


**Figure 4.10.** Comparison of the DOC outlet temperature, *HC* concentration,  $NO_2/NO_X$  ratio and *CO* concentration for the surrogate FTP cycle

Figure 4.10 shows the simulation results. The experimental DOC inlet and outlet val-

ues are plotted in black and red and the simulated DOC outlet values are plotted in blue. The first subplot in Figure 4.10 shows the comparison of the experimental and simulated temperatures. With the heat transfer to ambient added to the model, the model is able to simulate the response of the DOC experimental data except between 4-6 minutes. The second subplot shows the comparison of the DOC outlet HC concentrations. The experimental data shows complete conversion of HC across the DOC, but the model results show HC slip of upto 50 *ppmC* across the DOC. The third subplot shows the comparison of the  $NO_2/NO_X$  ratios. The simulated  $NO_2/NO_X$  ratio follows the experimental DOC outlet  $NO_2/NO_X$  ratio. The fourth subplot shows the comparison of the DOC outlet CO concentration. The experimental data shows complete conversion of CO across the DOC and the model is able to simulate the outlet CO concentration.

#### 4.1.7 Aged Data Simulation

To evaluate the capability of the DOC model to simulate aging of the catalyst, the experimental data was carried out at Johnson Matthey USA. The engine and the DOC used for testing was similar in size to the specification DOC used in this research and is described in chapter 3 . The test data consists of several engine speed load points to achieve different DOC inlet temperatures. The DOC inlet temperatures for the fresh(degreened) data ranged from 312 to 504<sup>0</sup>C. The DOC inlet *CO* concentrations varied from 23 to 169 *ppm*, *NO* concentrations varied from 140 to 571 *ppm* ,  $NO_2$  concentrations varied from 15 to 28 *ppm* and *HC* concentrations varied from 75 to 1380 *ppmC* . To simulate the DOC, the kinetic parameters identified (Table 4.2 ) from simulating the steady state and active regeneration data in this dissertation was used as the starting point for simulating the degreened data. The activation energy for the *CO* oxidation reaction was changed from



39J/kmol to 55J/kmol, the activation energy for the *NO* oxidation reaction was changed from 46.4J/kmol to 55J/kmol and activation energy for the *HC* oxidation reaction was changed from 25J/kmol to 55J/kmol. The activation energies were changed to simulate the shape of the conversion efficiency curves.

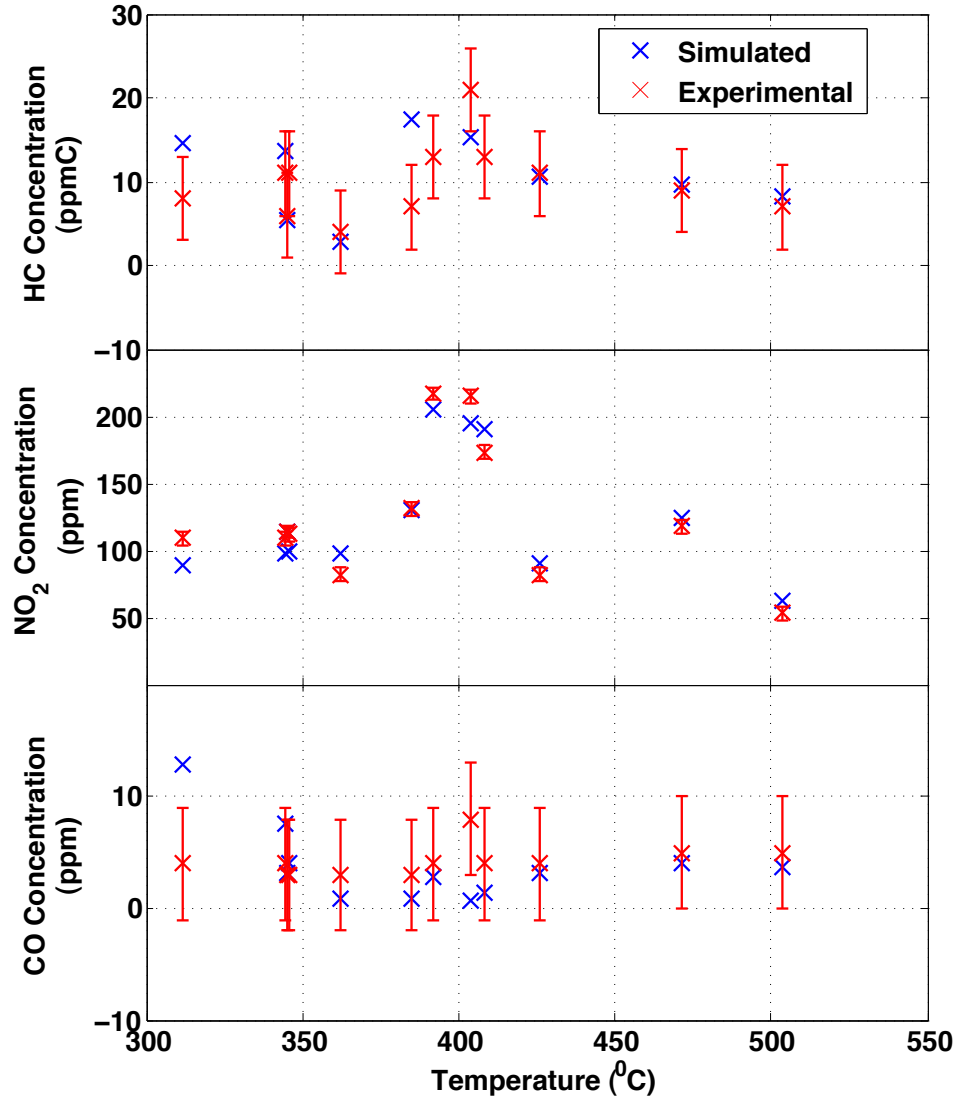


**Figure 4.11.** Comparison of the experimental and simulated DOC outlet *HC* , *NO<sub>2</sub>* and *CO* concentrations for the degreened data

Figure 4.11 shows a comparison between the experimental and simulated DOC outlet  $HC$ ,  $NO_2$  and  $CO$  concentrations for the fresh data. The DOC outlet  $HC$ ,  $NO_2$  and  $CO$  concentrations are plotted against temperature. The  $HC$  concentrations are plotted in  $ppm_C$  and the  $CO$  and  $NO_2$  concentrations are plotted in  $ppm$ . The experimental data is plotted with an error bar of  $\pm 5ppm$ . The simulated  $HC$  concentrations are within the error bars except for the  $311^0C$  and  $390^0C$  cases and the simulated  $CO$  concentration falls within the experimental error bars except for the  $311^0C$  condition where the experimental measured  $CO$  concentration is 3  $ppm$  and the simulated concentration is 12  $ppm$ . The simulated  $NO_2$  concentration falls within the experimental error bars except for temperatures between 390 to  $410^0C$  and at  $310^0C$ . The kinetic parameters used in the simulation are tabulated in Table 4.3.

**Table 4.3**  
Kinetic parameters used to simulate Johnson Matthey degreened data

	CO Oxidation		HC Oxidation		NO Oxidation	
$A(\text{fresh})$	1500000.0		1500000.0		4600000.0	
$A(\text{aged})$	1500000.0		1500000.0		1000000.0	
$E_a(\text{fresh})$	55.0		55.0		55.0	
$E_a(\text{aged})$	55.0		55.0		55.0	
Inhibition	$A_{a,j}$	$\Delta H_{a,j}$	$A_{a,j}$	$\Delta H_{a,j}$	$A_{a,j}$	$\Delta H_{a,j}$
$A_{a,1}$	0.0	7990.0	0.0	7990.0	0.0	7990.0
$A_{a,2}$	7.0E+07	75000.0	20.5	3000.0	6.8E+08	75000.0
$A_{a,3}$	0.0	96534.0	0.0	96534.0	0.0	96534.0
$A_{a,4}$	0.0	31036.0	0.0	31036.0	0.0	31036.0
$A_{a,5}$	0.0	0.0	0.0	0.0	0.0	0.0

The test data for the aged DOC consists of several engine speed load points to achieve different DOC inlet temperatures. To simulate the effect of aging, the DOC was aged at  $700^0C$  for 100  $hrs$ . The DOC inlet temperatures for the degreened data ranged from 275

to  $413^{\circ}\text{C}$ . The DOC inlet  $\text{CO}$  concentration varied from 79 to 159 ppm,  $\text{NO}$  concentrations varied from 165 to 637 ppm,  $\text{NO}_2$  concentrations varied from 9 to 29 ppm and  $\text{HC}$  concentrations varied from 28 to 46 ppm. Figure 4.12 shows a comparison between the experimental and simulated DOC outlet  $\text{HC}$ ,  $\text{NO}_2$  and  $\text{CO}$  concentration for the aged data.

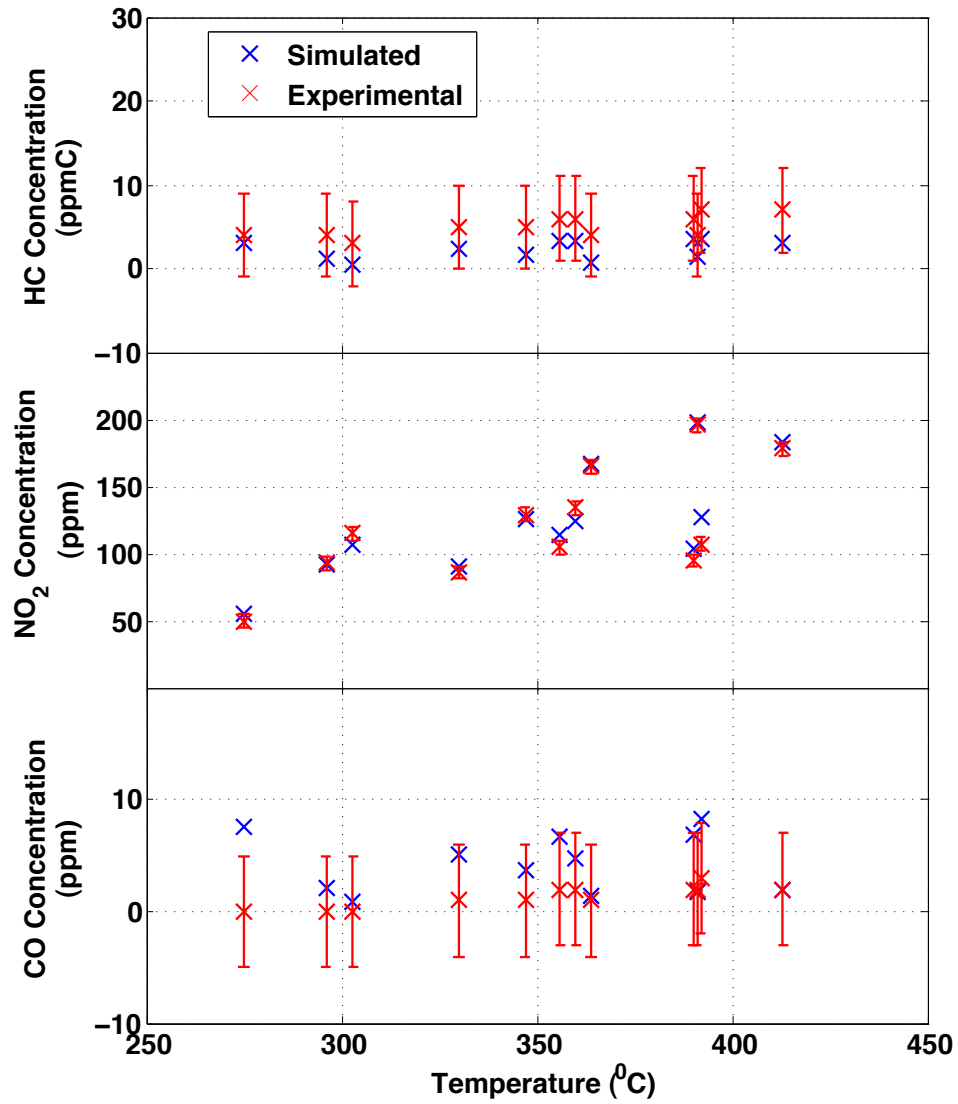


**Figure 4.12.** Comparison of the experimental and simulated DOC outlet  $\text{HC}$ ,  $\text{NO}_2$  and  $\text{CO}$  concentrations for the aged data

To simulate the aged DOC data, the kinetic parameters from the degreened data simulation was used as the starting point. The experimental  $CO$  and  $HC$  conversion efficiencies for the degreened and aged DOC were similar and to simulate the aged data the kinetic parameters for  $CO$  and  $HC$  oxidation reactions were not changed. The  $NO$  conversion efficiencies for the aged DOC was significantly lower compared to the degreened data. Hence, to simulate the aged data the pre exponential factor for the  $NO$  oxidation reaction was changed from  $4.6E06$  to  $1.5E06$ . Figure 4.12 shows a comparison between the experimental and simulated DOC outlet  $HC$ ,  $NO_2$  and  $CO$  concentration for the aged DOC data. The DOC outlet  $HC$ ,  $NO_2$  and  $CO$  concentrations are plotted against temperature. The  $HC$  concentrations are plotted in  $ppm_C$  and the  $CO$  and  $NO_2$  concentrations are plotted in ppm. The experimental data is plotted with an error bar of  $\pm 5$  ppm. The simulated  $HC$  concentration are within the error bars and the simulated  $CO$  concentration falls within the experimental error bars except for the  $250^0C$  condition where the experimental measured  $CO$  concentration is zero and the simulated concentration is 8 ppm. The simulated  $NO_2$  concentration falls within the experimental error bars except for the  $390^0C$  temperature condition. The kinetic parameters used to simulate both the degreened and aged data are tabulated in Table 4.4. It can be observed that the kinetic parameters for the degreened and aged data are similar except for the  $NO$  oxidation reaction pre exponential factor. The results show that with aging, the reactions still have the similar activation energies but the pre exponential factor for  $NO$  oxidation is lower. In a OBD model for the DOC, this effect would be important to include since the  $NO_2$  into the CPF affects the rate of  $NO_2$  production assisted PM oxidation and it would in turn affect the SCR reactions. Since the  $NO_2/NO_X$  ratio is an important parameter for the  $NO_X$  conversion efficiencies and the  $NH_3$  slip [1].

**Table 4.4**  
Kinetic parameters used to simulate Johnson Matthey degreened and aged data

	CO Oxidation		HC Oxidation		NO Oxidation	
$A(\text{degreened})$	1500000.0		1500000.0		4600000.0	
$A(\text{aged})$	1500000.0		1500000.0		1000000.0	
$E_a(\text{degreened})$	55.0		55.0		55.0	
$E_a(\text{aged})$	55.0		55.0		55.0	
Inhibition*	$A_{a,j}$	$\Delta H_{a,j}$	$A_{a,j}$	$\Delta H_{a,j}$	$A_{a,j}$	$\Delta H_{a,j}$
$A_{a,1}$	0.0	7990.0	0.0	7990.0	0.0	7990.0
$A_{a,2}$	7.0E+07	75000.0	20.5	3000.0	6.8E+08	75000.0
$A_{a,3}$	0.0	96534.0	0.0	96534.0	0.0	96534.0
$A_{a,4}$	0.0	31036.0	0.0	31036.0	0.0	31036.0
$A_{a,5}$	0.0	0.0	0.0	0.0	0.0	0.0

\*Both degreened and aged data.

## 4.2 SCR High Fidelity Model

A metal based Zeolite SCR catalyst is commonly for heavy duty diesel application. The function of the SCR is to reduce the  $NO_X$  in the exhaust to  $N_2$  and  $H_2O$ . To achieve this, urea is injected into the exhaust upstream of the SCR. The urea thermally decomposes to  $NH_3$  and adsorbs onto the surface of the catalyst. The urea decomposition is a complex function which depends on the SCR inlet temperature, flowrates and injection profile[59]. The urea decomposes in the exhaust and on the catalyst surface[60]. Some of the  $NH_3$  reacts with the  $NO$  and  $NO_2$  on the catalyst surface to form  $N_2$  and  $H_2O$  and the rest of the  $NH_3$  is stored in the catalyst through adsorption. In addition,  $NH_3$  slip occurs which is oxidized by the AMOX catalyst brick at the SCR outlet. The stored ammonia either reacts with the  $NO_X$  or desorbs from the catalyst surface to the exhaust. Several 1D high-fidelity

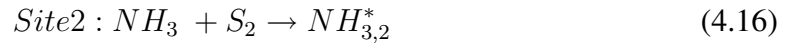
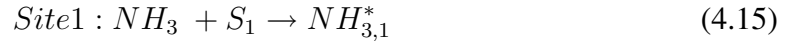
models similar to the model described in this study have been reported in the literature[34, 54,61,62].

The model described in this section was developed by Song et al in reference[1]. The model was developed to simulate the copper-Zeolite SCR used in the aftertreatment system Cummins ISB 2010 engine described in section 3. The bench reactor [63] and engine dynamometer[64] data were used to calibrate the model. The model and the calibration is briefly described in this dissertation since it is used in the developing the SCR reduced order model.

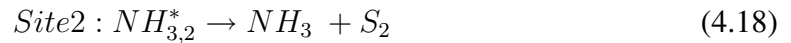
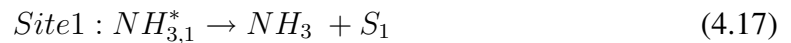
#### 4.2.1 Reactions in the SCR

The  $NH_3$  storage is modeled using two storage sites, site 1 participates in the  $NH_3$  storage and  $NO_X$  reduction where as site 2 participates only in the storage of  $NH_3$  [63, 64]. The reduction of the  $NO_X$  take place through three main reaction mechanisms[61,62, 65]: standard, fast and slow SCR reactions as shown in equations 4.20 4.21, 4.22 and 4.23 in reference [61].

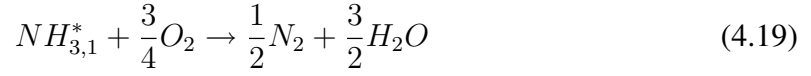
$NH_3$  adsorption:



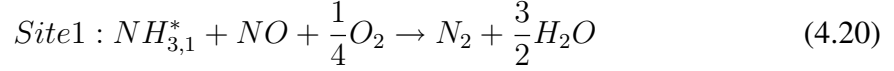
$NH_3$  desorption:



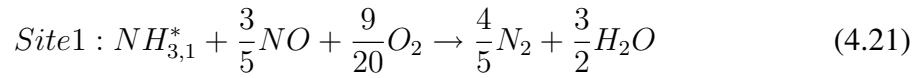
$NH_3$  oxidation:



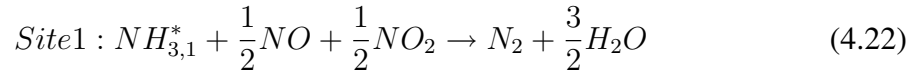
Standard SCR 1:



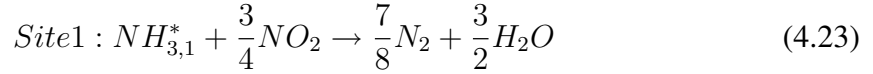
Standard SCR 2:



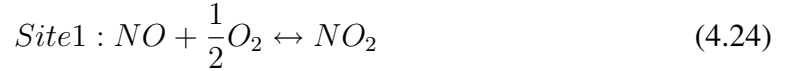
Fast SCR:



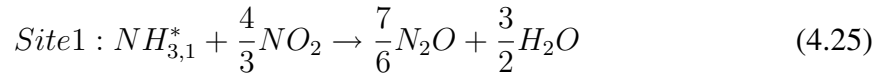
Slow SCR:



NO oxidation:



$N_2O$  formation:



These reactions are exponential functions in temperature, hence the  $NO_X$  reduction performance of the SCR is also a function of the temperature. There are two main types of the commercially available Zeolite based SCR's in production in the U.S depending on the catalyst formulation: Iron-Zeolite(Fe-Ze) and Copper-Zeolite(Cu-Ze). Among the two SCR catalysts, the Cu-Zeolite SCR performs better at low temperatures[66–68]. Several studies[61,66] have shown that the maximum  $NO_X$  conversion efficiency can be achieved at  $\frac{NO_2}{NO_X} = 0.5$  for both Fe-Zeolite and Cu-Zeolite catalysts.

## 4.2.2 Mass and Energy Balance Equations

The differential equations describing the high-fidelity SCR model are shown in Equations 4.26 to 4.29. Equations 4.26 and 4.27 is the species balance equation for  $NH_3$ ,  $NO$ ,  $NO_2$ , and  $N_2O$ .

$$\epsilon \frac{\partial C_{g,i}}{\partial t} = -u \frac{\partial C_{g,i}}{\partial x} - \beta_i A_g (C_{g,i} - C_{s,i}) \quad (4.26)$$

$$(1 - \epsilon) \frac{\partial C_{s,i}}{\partial t} = \beta_i A_g (C_{g,i} - C_{s,i}) - \sum_{j=NH_3}^{N_2O} n_{i,j} R_j \quad (4.27)$$

$$i = NH_3, NO, NO_2, N_2O \text{ \& } j = \text{Ads, Des, Std, Fst, Slo, Oxi}$$

The symbol  $u$  is the velocity of the exhaust gas in  $m/s$ , the  $C_i$  are the concentrations of  $NH_3$ ,  $NO$ ,  $NO_2$ , and  $N_2O$ ,  $n_{i,j}$  is the stoichiometric coefficient and the  $R_j$  are the reaction rates. Equations 4.28 and 4.29 describe the  $NH_3$  balance equations for  $NH_3$  storage sites 1 and site 2 in the two site model[69].

$$\Omega_1 \dot{\theta}_1 = R_{Ads,1} - R_{Des,1} - 4R_{Oxi} - 4R_{Std} - 4R_{Fst} - 4R_{Slo} \quad (4.28)$$

$$\Omega_2 \dot{\theta}_2 = R_{Ads,2} - R_{Des,2} \quad (4.29)$$

where,  $\theta_i$  are  $NH_3$  storage fractions and  $\Omega_i$  are storage capacities. The quantities  $RR_{Ads,1}$ ,  $RR_{Ads,2}$ ,  $RR_{Des,1}$  and  $RR_{Des,2}$  are the adsorption and desorption rates.  $R_{Oxi}$ ,  $R_{std}$ ,  $R_{fst}$  and  $RR_{slow}$  are the reaction rates for  $NH_3$  oxidation, standard SCR, fast SCR and slow



SCR reactions. The rate equations for all the reactions in the SCR are shown below:

$$R_{Ads,1} = k_{Ads,1} C_{NH_3,s} (1 - \theta_1) \Omega_1 \quad (4.30)$$

$$R_{Des,1} = k_{Des,1} \theta_1 \Omega_1 \quad (4.31)$$

$$R_{Ads,2} = k_{Ads,2} C_{NH_3,s} (1 - \theta_2) \Omega_2 \quad (4.32)$$

$$R_{Des,2} = k_{Des,2} \theta_2 \Omega_2 \quad (4.33)$$

$$R_{Oxi,NH_3} = k_{Oxi,NH_3} \eta_{O_2} \theta_1 \Omega_1 \quad (4.34)$$

$$R_{Std} = k_{Std} C_{NO,s} \eta_{O_2} \theta_1 \Omega_1 \quad (4.35)$$

$$R_{Std_2} = k_{Std_2} C_{NO,s} \eta_{O_2} \theta_1 \Omega_1 \quad (4.36)$$

$$R_{Fst} = k_{Fst} C_{NO,s} C_{NO_2,s} \theta_1 \Omega_1 \quad (4.37)$$

$$R_{Slo} = k_{Slo} C_{NO_2,s} \theta_1 \Omega_1 \quad (4.38)$$

$$R_{NO} = k_{NO} \left( C_{NO,s} c_{O_2}^{0.5} - \frac{C_{NO_2,s}}{K_p} \right) \quad (4.39)$$

$$R_{N_2O} = k_{N_2O} C_{NO_2,s} \theta_1 \Omega_1 \quad (4.40)$$

The reaction rate coefficients  $k_i$  are of the Arrhenius form and are expressed as:

$$k_i = A_i e^{-\frac{E_{a,i}}{RT}}$$

$$i = Ads_1, Des_1, Ads_2, Des_2, Std_1, Std_2, Fast, Slow, NO_{oxidation} \& N_2O \text{ Formation} \quad (4.41)$$

Where,  $A_i$  is the pre exponential factor and  $E_{ai}$  is the activation energies for the  $i^{th}$  reaction.

### 4.2.3 High Fidelity Model Calibration

The SCR high fidelity model was calibrated to both the engine and the reactor data. The details of the calibration process and the data are described in references [1,63,64] . This section shows the results for one of the test cases (test point 8) in Table 3.5.

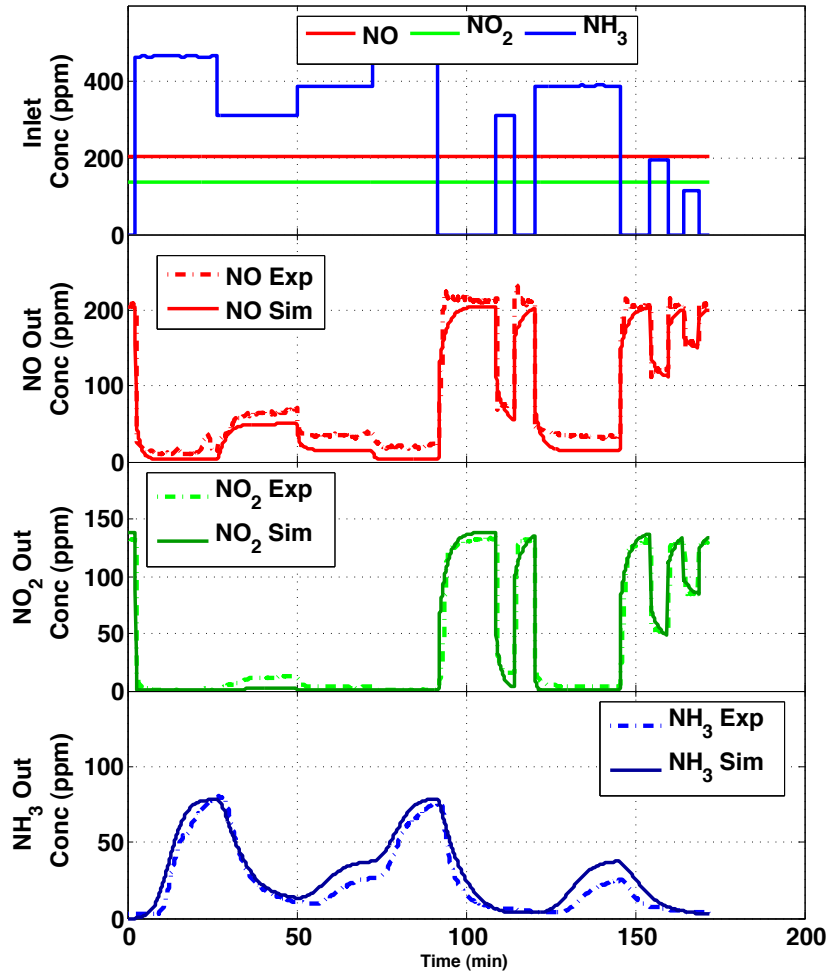


**Figure 4.13.** Comparison of the SCR outlet  $NO$  ,  $NO_2$  and  $NH_3$  concentrations between the experimental and the high-fidelity model corrected for sample line effects[1].

Figure 4.13 shows a comparison of the SCR outlet  $NO$   $NO_2$  and  $NH_3$  concentration between the mass spectrometer experimental data and the high-fidelity model. The first

subplot shows the SCR inlet  $NH_3$ ,  $NO$  and  $NO_2$  concentrations. The  $NO$  and  $NO_2$  concentrations are maintained constant for the entire test and the inlet  $NH_3$  concentration is varied by controlling the urea injector located upstream of the SCR to achieve different levels of  $NH_3/NO_X$  ratio. The second subplot shows the comparison of the SCR outlet  $NO$  concentration. It is observed that the high fidelity model simulates the experimental  $NO$  concentration profile with less than  $\pm 30$  ppm error. The third subplot shows the comparison of the SCR outlet  $NO_2$  concentration. Similar to  $NO$  the that the high fidelity model simulates the experimental  $NO_2$  concentration profile with less than  $\pm 20$  ppm error. The fourth subplot shows the comparison of the SCR outlet  $NH_3$  concentration. An exhaust sample line model described in reference[1,64] was used to simulate the effect of adsorption of the  $NH_3$  in the sample line. The high-fidelity model follows the experimental  $NH_3$  concentration profile with less than  $\pm 48$  ppm error when the simulation results are corrected for the sample line adsorption/desorption effects.

### 4.3 SCR Aged Data Simulation

The testing for the aged SCR was conducted at Oak Ridge National Laboratories on an SCR core sample of 8 cm length and 2 cm diameter. The data for both degreened and aged core samples were acquired on a reactor setup and Spaci-IR measurement technique was used to measure the emissions. The cores were degreened for 4 hours at  $700^{\circ}C$  and aged core was aged at  $800^{\circ}C$  for 16 hours. The simulation of the degreened and aged SCR with the SCR highfidelity model was done by Xiaobo Song as part of his PhD research work and detailed description of the test setup and the core samples is described in reference [1]. The experimental results showed the aging process does not change the overall  $NO_X$

conversion efficiencies but changes the axial concentration profiles. The experimental data also showed that the  $NH_3$  storage capacity for aged SCR is 30% lower compared to the degreened SCR.

The SCR high fidelity model was used to simulate both the degreened and aged SCR data. The kinetic parameters simulate the axial  $NH_3$  storage and axial  $NO$ ,  $NO_2$  and  $NH_3$  concentration profiles were identified. Table 4.5 shows the important kinetic parameters that were different between the degreened and aged SCR data. The table shows that the  $NH_3$  storage capacity for the aged SCR is lower compared to the degreened SCR. The table also shows the activation energies for the  $NH_3$  desorption,  $NH_3$  oxidation, fast SCR and standard SCR reactions for aged SCR are lower compared to the degreened SCR.

**Table 4.5**  
The important kinetic parameters to simulate degreened and aged SCR data

Parameter	De-greened	Aged	Unit
$\Omega$	138	94.6	$gmol/m^3$
$E_{ads}$	0	0	$kJ/gmol$
$E_{des}$	38.2	28.6	$kJ/gmol$
$A_{NH_3Oxi}$	1.35E+04	5.81E+02	1/s
$E_{NH_3Oxi}$	86	66.3	$kJ/gmol$
$A_{Fast}$	1.40E+08	6.13E+06	$m^6/gmol^2.s$
$E_{Fast}$	52.8	41.6	$kJ/gmol$
$A_{Std}$	9.99E+04	2.33E+04	$m^3/gmol.s$
$E_{Std}$	47.3	39.9	$kJ/gmol$

It was concluded that the aging of the SCR results in 30% lower  $NH_3$  storage capacity and the aging also decreases the activation energies for  $NH_3$  desorption,  $NH_3$  oxidation, fast SCR and standard SCR reactions. The results showed that the SCR aging does not change the overall  $NO_X$  conversion efficiency of the SCR but changes the axial  $NH_3$  storage and  $NO$ ,  $NO_2$  and  $NH_3$  concentration profiles.

## 5. DOC AND SCR REDUCED ORDER MODELS

The high fidelity models are accurate in predicting the outlet concentrations and temperatures from a DOC and a SCR. But these models are computationally demanding and state estimation strategies are difficult to implement with them. Hence, reduced order models are an important part of state estimation which is the focus of this dissertation. The reduced order models are often based on the complex models, but some assumptions are made to reduce the computational resources needed. This section describes the development of the reduced order models for the DOC and the SCR. To reduce the order of the model, the following assumptions were made:

1. The reactions are instantaneous  $\implies \frac{\partial C_g}{\partial t} = \frac{\partial C_s}{\partial t} = 0$
2. The surface phase and gas phase concentrations are identical and can be assumed to be equal,  $C = C_g = C_s$ .
3. The surface phase and gas phase temperatures are identical and can be assumed to be equal,  $T = T_g = T_s$ .

The assumption 2 results in the elimination of the mass transfer coefficients from the mass balance equations and the assumption 3 results in the elimination of the heat transfer coefficients from the energy balance equations. If the DOC and SCR operates in a space

velocity range where the reactions are mass transfer limited, then the reduced order model will not be able to simulate the reactions. The mass transfer coefficients could be simulated but it would make reduced order model and the estimator significantly more complex computationally.

## 5.1 DOC Reduced Order Model Development

A reduced order DOC model to capture the non linear behavior of the DOC was developed based on the high fidelity model in references [28,53]. The reduced order model employs bulk phase energy balance equations and reactions instead of separate gas phase and surface phase reactions and energy balance equations as used in many high fidelity model studies. This reduces the complexity and reduces the simulation time and computational requirements to simulate the DOC. A schematic highlighting the important differences between the high fidelity and reduced order model is shown in Figure 5.1. A 1-D, single channel representation was developed using MATLAB/Simulink. A discrete time step solver is used to solve the species and energy conservation equations.

Using assumptions 1 and 2, the equations (4.4) and (4.5) reduce to equation (5.1), an ODE for the reduced order model species balance.

$$\epsilon u \frac{dC_i}{dx} = -r_i \quad (5.1)$$

$$i = CO, NO, NO_2, C_3H_6$$

Using the assumption 3, the equations (4.6) and (4.7) reduce to equation (5.2) for the re-

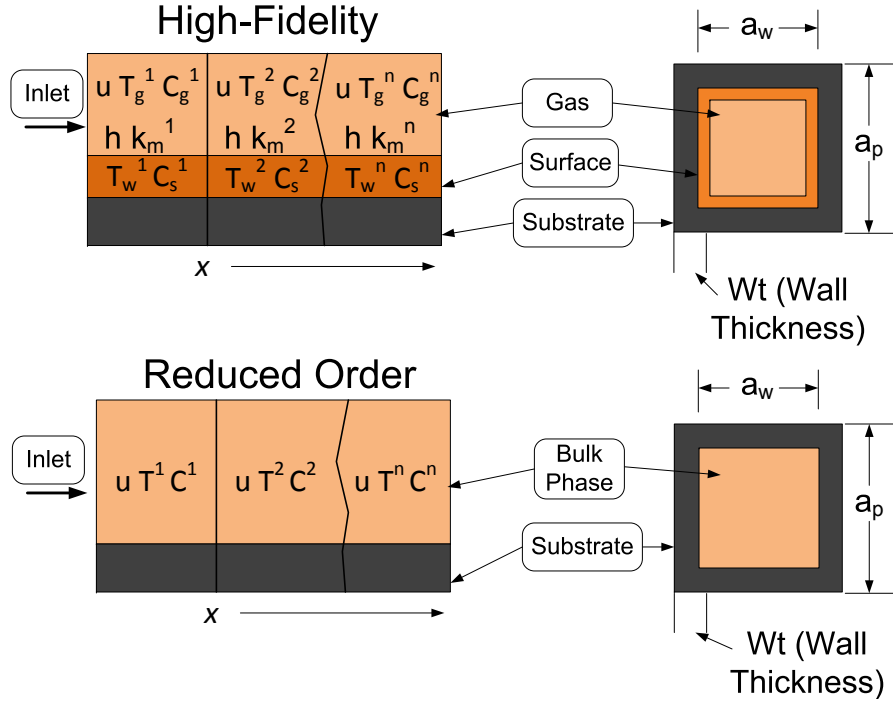


**Figure 5.1.** Schematic showing the differences between high fidelity and reduced order DOC model

duced order model energy balance.

$$(\rho_s c_{p,s} + \rho c_v) \frac{\partial T}{\partial t} = -\rho u c_p \frac{\partial T}{\partial x} + -\frac{A_g}{1 - \epsilon} \sum_{i=1}^3 \frac{\Delta h_i r_i}{MW_i} \quad (5.2)$$

$$i = CO, NO, NO_2, C_3H_6$$

where,  $\rho_s$  and  $c_{p,s}$  are the density and specific heats of the substrate,  $\rho$  is the density of the exhaust gas,  $c_p$  and  $c_v$  are specific heats of the exhaust gas,  $\Delta h_i$  is the enthalpy of the  $CO$ ,  $NO$  and  $C_3H_6$  oxidation reactions,  $MW_i$  is the molecular weight of  $i^{th}$  species and  $A_g$  is the geometric surface area.

## 5.2 SCR Reduced Order Model Development

The SCR reduced order model is based on the 1D high-fidelity model[63,64]. The SCR model is similar to several models reported in the published literature. The high fidelity model simulates gas and surface phase along with  $NH_3$  storage. The model uses two  $NH_3$  storage sites to simulate  $NH_3$  adsorption and desorption. The important difference between the reduced order and hi-fidelity model is the absence of the separate gas and surface phase in the reduced order model. In the reduced order model, the gas and surface phase are combined to form a representative bulk phase. Figure 5.2 highlights the important differences between the high-fidelity and reduced order SCR model.

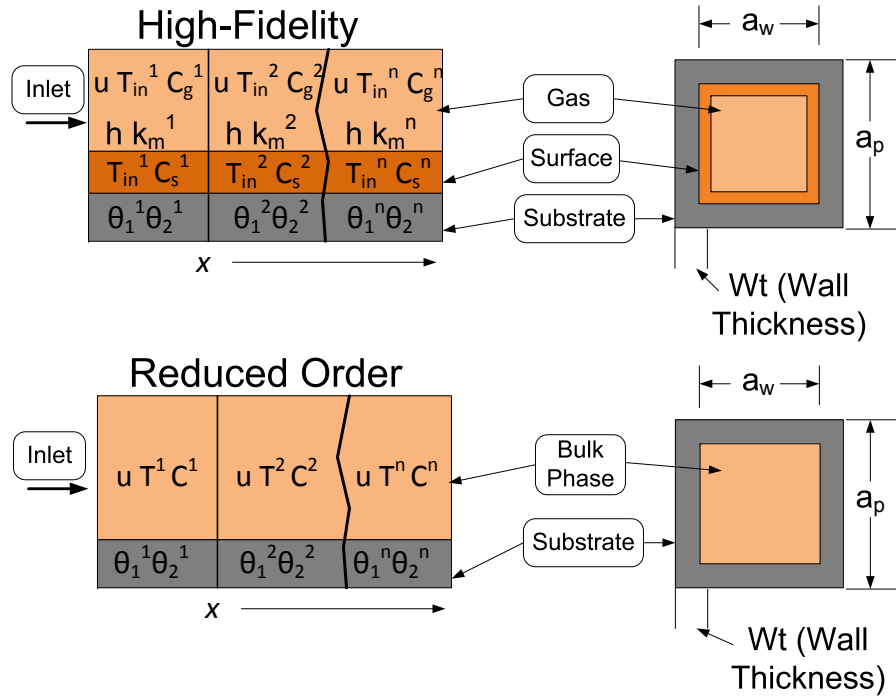


**Figure 5.2.** Schematic showing the differences between high fidelity and reduced order SCR model

The SCR model consists of adsorption and desorption of  $NH_3$  on site 1 and 2. Site 2 also consists of  $NH_3$  oxidation, standard SCR, fast SCR, slow SCR,  $NO$  oxidation and



$N_2O$  production reactions. The chemical balance equations describing these reactions are shown in Equations 4.15 through 4.25.

Using the assumption 1 and 2, Equations (4.26) and (4.27) reduces to Equation (5.3), the species balance equation for  $NH_3, NO, NO_2$  and  $N_2O$ .

$$\frac{\partial C_i}{\partial t} = -u \frac{\partial C_i}{\partial x} - \sum_j n_{i,j} R_j \quad (5.3)$$

$$i = NH_3, NO, NO_2, N_2O \text{ \& } j = Ads, Des, Std, Fst, Slo, Oxi$$

The symbol  $u$  is the velocity of the exhaust gas, the  $C_i$  are the concentrations of  $NH_3, NO, NO_2$  and  $N_2O$ ,  $n_{i,j}$  is the stoichiometric coefficient and the  $R_j$  are the reaction rates. The  $NH_3$  balance equations for the high fidelity and reduced order models are the same. Equations (5.4) and (5.5) are the  $NH_3$  balance equations for storage site 1 and 2 respectively.

$$\Omega_1 \dot{\theta}_1 = R_{Ads,1} - R_{Des,1} - 4R_{Oxi} - 4R_{Std} - 4R_{Fst} - 4R_{Slo} \quad (5.4)$$

$$\Omega_2 \dot{\theta}_2 = R_{Ads,2} - R_{Des,2} \quad (5.5)$$

where,  $\theta_i$  are  $NH_3$  storage fractions and  $\Omega_i$  are storage capacities. The quantities  $RR_{Ads,1}$ ,  $RR_{Ads,2}$ ,  $RR_{Des,1}$  and  $RR_{Des,2}$  are the adsorption and desorption rates.  $R_{Oxi}$ ,  $R_{std}$ ,  $R_{fst}$  and  $RR_{slow}$  are the reaction rates for  $NH_3$  oxidation, standard SCR, fast SCR and slow SCR reactions. The reaction rate and rate coefficients are the same as the hi-fidelity model and are described in Equations 4.30 to 4.40.

### 5.3 DOC Reduced Order Model Calibration

The DOC reduced order model was simulated with the steady state and active regeneration data and compared to the high fidelity model and the experimental data. The steady state data was collected for three different space velocities  $162k$  ,  $235k$  and  $281khr^{-1}$  . At each of these space velocities the DOC inlet temperatures were varied. The active regeneration tests was collected for three space velocities of  $162k$  ,  $235k$  and  $281khr^{-1}$  at a DOC inlet temperature of greater than  $320^{\circ}C$  . The incylinder hydrocarbon injection at the DOC inlet was varied to achieve different DOC outlet temperatures.

#### 5.3.1 Steady State Simulation

The test matrix for steady state testing consists of three space velocities of  $162k$  ,  $235k$  and  $281khr^{-1}$ . The DOC inlet temperature was varied and the  $NO$  ,  $CO$  and  $HC$  conversion across the DOC was measured. Table 5.1 shows the space velocities and the DOC inlet temperatures used for the steady state testing conditions. More details about the test setup, test conditions and calibration of high fidelity model to the data can be found in reference[53].

**Table 5.1**  
Steady state testing conditions

Space Velocities( $hr^{-1}$ )	Inlet Temperature( $^{\circ}C$ )
162k	237-457
235k	252-492
281k	273-507

To simulate the experimental data with the reduced order model, some of the calibration constants were changed from the high fidelity model in Table 4.2. With the high fidelity  $NO$  oxidation kinetic parameters, the reduced order model was predicting higher  $NO_2/NO_X$  ratios at temperatures  $450^{\circ}C$  and above. To simulate the DOC outlet  $NO_2/NO_X$  at higher temperatures, the inhibition factor associated with  $NO$  concentrations was set to  $15.0E05$  and the pre exponential for  $NO$  oxidation was changed to  $10.15E05$ . The complete list of calibration constants are given in Table 5.2.

**Table 5.2**  
Kinetic parameters used to simulate steady state data

	CO Oxidation		HC Oxidation		NO Oxidation	
Activation Energy	894000.0		10000.0		715000.0	
Preexponential Factor	39.0		25.0		46.4	
Inhibition	$A_{a,j}$	$\Delta H_{a,j}$	$A_{a,j}$	$\Delta H_{a,j}$	$A_{a,j}$	$\delta H_{a,j}$
$A_{a,1}$	0.0	7990.0	0.0	7990.0	0.0	7990.0
$A_{a,2}$	$7.0E+07$	75000.0	20.5	3000.0	$6.8E+08$	75000.0
$A_{a,3}$	0.0	96534.0	0.0	96534.0	0.0	96534.0
$A_{a,4}$	0.0	31036.0	0.0	31036.0	150000.0	31036.0
$A_{a,5}$	0.0	0.0	0.0	0.0	0.0	0.0

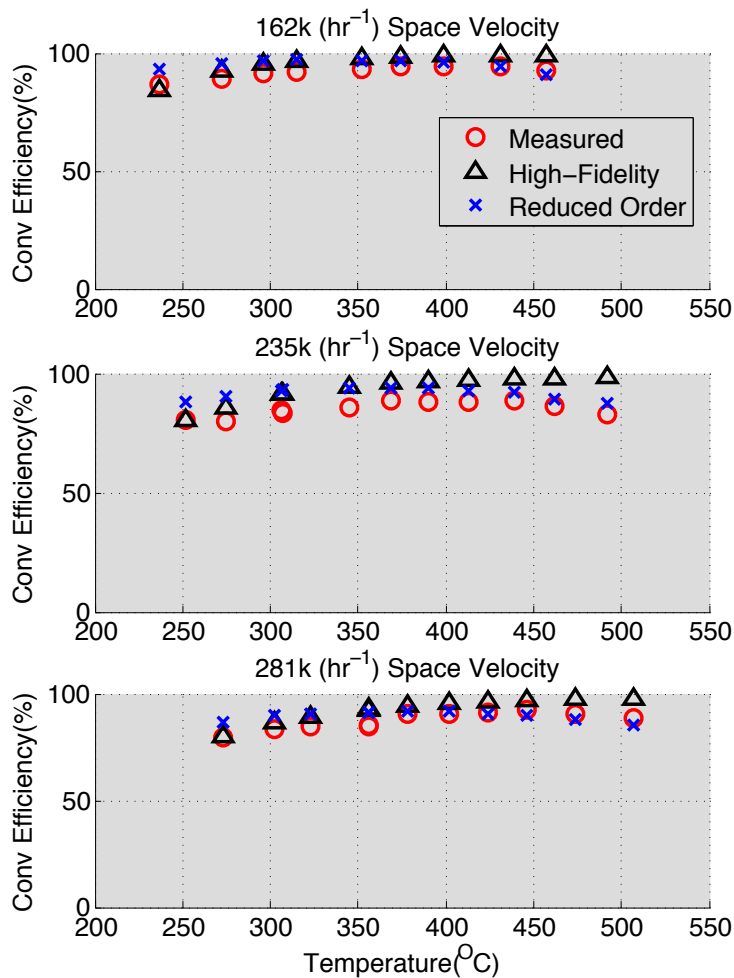


**Figure 5.3.** Comparison of DOC outlet HC conversion efficiencies between the high fidelity and reduced order model for the steady state data

Figure 5.3 shows the comparison of the HC conversion efficiencies between the measured experimental, high fidelity model and the reduced order model for three space velocities. The reduced order model agrees with the experimental and high fidelity model DOC HC conversion efficiencies within  $\pm 12\%$ . The  $CO$  conversion plot is not shown here since the  $CO$  conversion across the DOC during steady state conditions were close to 100% for all the space velocities and the reduced order model agrees with the experimental data.

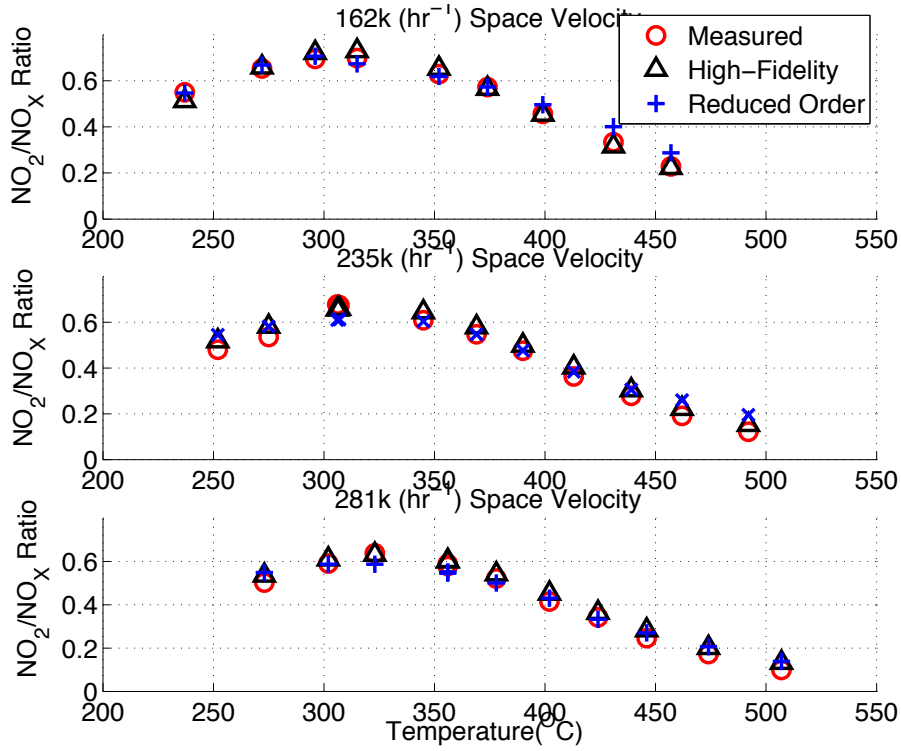


**Figure 5.4.** Comparison of DOC outlet  $NO_2/NO_X$  ratios between the high fidelity and reduced order model for the steady state data

Figure 5.4 shows a comparison of the DOC outlet  $NO_2/NO_X$  ratios from the high fidelity and reduced order model with the experimental measurements for the three space velocities. The reduced order model agrees with the experimental and the high fidelity model DOC outlet  $NO_2/NO_X$  ratios generally within maximum error of  $\pm 30\%$ . Table 5.3 shows the tabulated values of the comparison of the experimental and simulated  $CO$ ,  $NO$ ,  $NO_2$  and  $HC$  concentrations for the steady state testing. The table also shows the error between the simulated and experimental DOC outlet  $NO_2$  concentration in ppm and percent which ranged from  $-50$  to  $15$  ppm and  $-60$  to  $10\%$ . Typically the  $NO_2$  concentrations were within  $\pm 20$  ppm.

**Table 5.3**

Comparison of the reduced order simulated and the experimental DOC outlet  $CO$ ,  $NO$ ,  $NO_2$  and  $HC$  concentrations for the steady state data

$T_{Intlet}$	<b>Experimental</b>				<b>Simulated</b>				$\Delta NO_2$	
	<b>CO</b>	<b>NO</b>	$NO_2$	<b>HC</b>	<b>CO</b>	<b>NO</b>	$NO_2$	<b>HC</b>		
$^{\circ}C$	ppm	ppm	ppm	ppmC	ppm	ppm	ppm	ppmC	ppm	%
237	0	150	182	13	0	150	181	7	1	1%
296	0	102	232	9	0	98	236	3	-4	-2%
315	0	128	298	8	0	139	288	3	10	3%
352	1	170	288	6	0	175	283	3	5	2%
399	0	329	276	4	0	305	300	3	-24	-9%
374	1	215	288	5	0	215	288	3	0	0%
431	0	455	228	4	0	409	274	4	-46	-20%
457	0	759	225	4	0	702	282	5	-57	-25%
272	0	111	209	11	0	106	214	4	-5	-2%
252	0	129	119	24	0	113	135	14	-16	-13%
275	0	131	151	23	0	118	164	11	-13	-9%
390	1	182	165	11	0	182	165	6	0	0%
345	0	121	188	14	0	122	187	6	1	1%
369	1	148	179	11	0	148	179	6	0	0%
439	1	368	142	7	0	354	156	5	-14	-10%
462	1	407	96	7	0	372	131	5	-35	-36%
492	1	601	83	7	0	551	133	5	-50	-60%
413	1	299	170	8	0	289	179	5	-9	-5%
306	1	110	231	15	0	133	208	7	23	10%
307	0	112	232	16	0	134	210	7	22	9%
402	1	169	120	8	0	165	124	7	-4	-3%
356	0	129	180	13	0	137	169	7	11	6%
474	1	413	86	4	0	396	103	5	-17	-20%
273	0	121	121	23	0	109	132	15	-11	-9%
378	1	146	159	8	0	152	153	7	6	4%
302	0	116	167	16	0	117	166	10	1	1%
424	0	287	149	5	0	291	145	5	4	3%
323	0	109	192	14	0	124	177	9	15	8%
446	0	375	122	4	0	363	134	5	-12	-10%
507	0	647	71	4	0	619	99	5	-28	-39%
356	0	132	181	12	0	142	171	7	10	6%

### 5.3.2 Active Regeneration Simulation

The active regeneration experiments were done on the test setup described in chapter 3. Three test points corresponding to different space velocities with the DOC inlet temperatures of greater than 320°C were selected. The hydrocarbon injection was varied to achieve DOC outlet temperatures from 500-600°C. Table 4 shows the engine conditions used for active regeneration testing. The DOC inlet and outlet concentrations and the temperatures were measured during the experiments. The hydrocarbon concentrations downstream of the DOC were measured and the hydrocarbon concentrations upstream of the DOC were estimated using an energy balance across the DOC. A detailed description of this procedure is given in Reference [4].

Figure 5.5 shows the comparison of the *CO* conversion efficiencies between the measured, high fidelity model and the reduced order model for three space velocities. The measured *CO* conversion efficiency shows *CO* production across the DOC and both the reduced order model and the high fidelity model are not able to simulate this due to the absence of *CO* production reaction in the model.

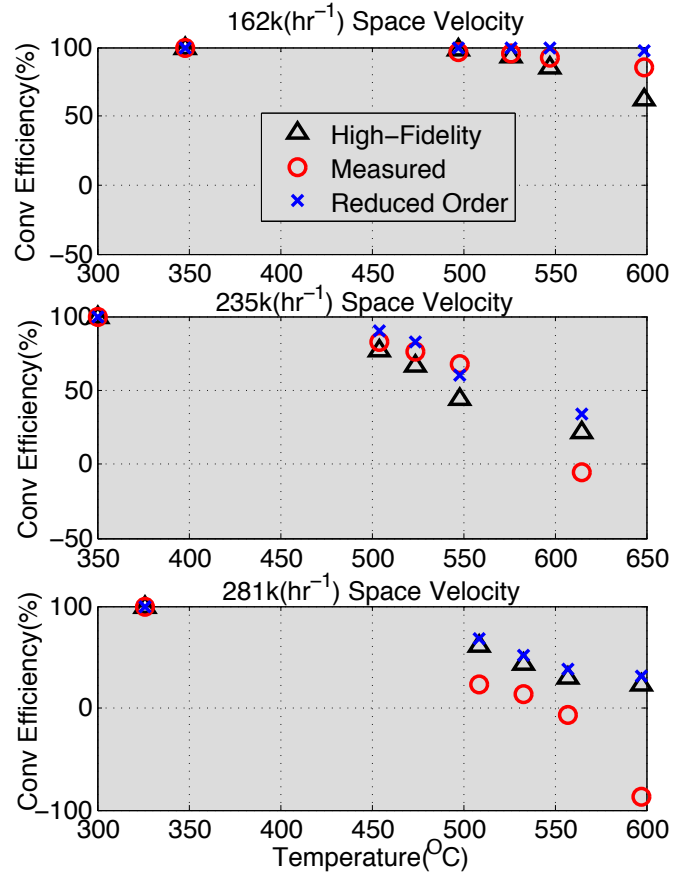


**Figure 5.5.** Comparison of DOC outlet CO conversion efficiencies between the high fidelity and reduced order model for the active regeneration experiments

Figure 5.6 shows the comparison of the *HC* conversion efficiencies between the measured, high fidelity model and the reduced order model for three space velocities. The observed experimental *HC* conversion efficiency is always greater than 90% and the reduced order model agrees with the measured and high fidelity model DOC *HC* conversion efficiencies within +/-6%.



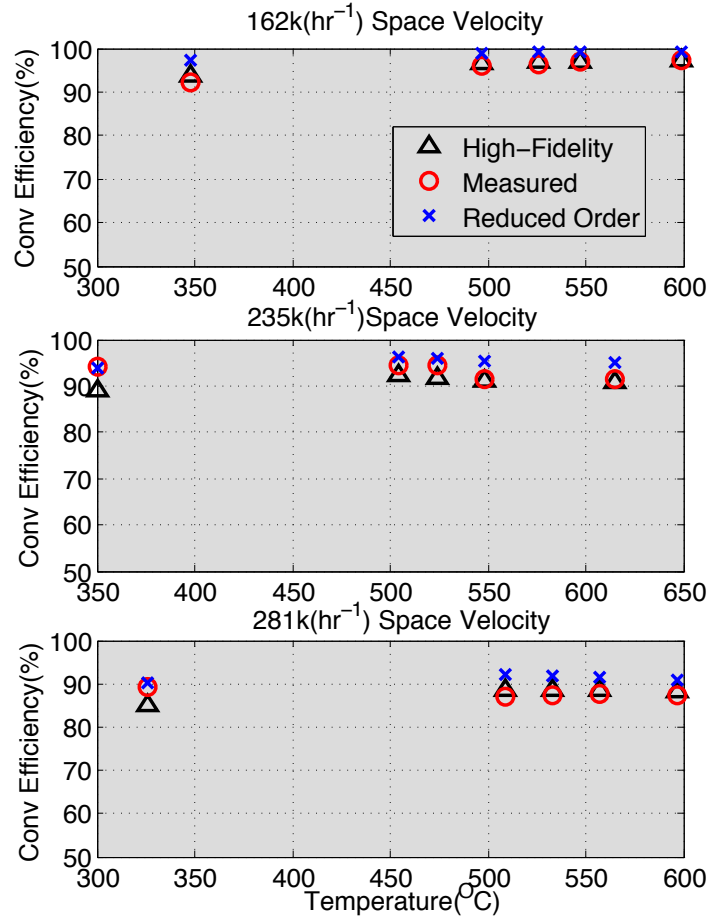


**Figure 5.6.** Comparison of DOC outlet HC conversion efficiencies between the high fidelity and reduced order model for the active regeneration experiments

Figure 5.7 shows the comparison of the DOC outlet  $NO_2/NO_X$  ratios between the measured, high fidelity model and the reduced order model for three space velocities. The DOC outlet  $NO_2/NO_X$  ratios are plotted against the experimental DOC outlet temperatures. The experimental data shows lower  $NO$  conversion with the increase in the DOC outlet temperature. The reduced order model agrees with the experimental and high fidelity model DOC  $NO_2/NO_X$  ratios within +/-20%.

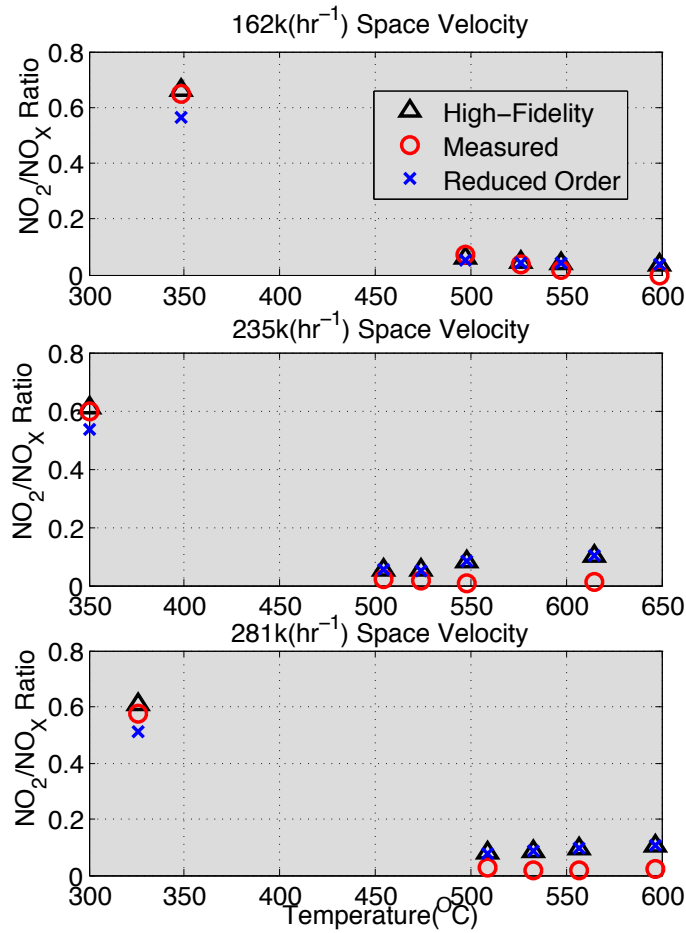


**Figure 5.7.** Comparison of DOC outlet  $NO_2/NO_X$  ratios between the high fidelity and reduced order model for the active regeneration experiments

Figure 5.8 shows the comparison of the DOC outlet temperatures between the measured, high fidelity model and the reduced order model for three space velocities. The DOC outlet temperatures are plotted against the experimental DOC outlet temperature along the x axis. The reduced order model agrees with the experimental and high fidelity model DOC outlet temperatures within  $\pm 3\%$ . Table 5.4 shows the tabulated values of the comparison of the experimental and simulated  $CO$ ,  $NO$ ,  $NO_2$  and  $HC$  concentrations for the active regeneration experiments. The table also shows the error between the simulated and

experimental DOC outlet  $NO_2$  concentration in ppm and percent.

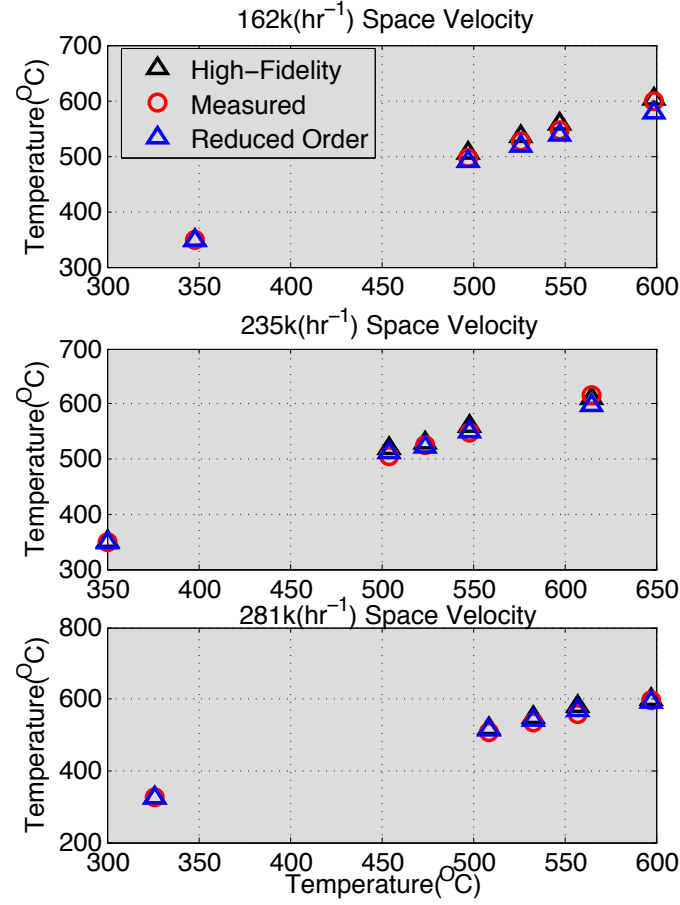


**Figure 5.8.** Comparison of DOC outlet temperature between the high fidelity and reduced order model with respect to experimental DOC outlet temperature for the active regeneration experiments

Table 5.4 shows the tabulated values of the comparison of the experimental and simulated  $CO$ ,  $NO$ ,  $NO_2$  and  $HC$  concentrations for the steady state testing. The table also shows the error between the simulated and experimental DOC outlet  $NO_2$  concentration in ppm and percent which ranged from  $-27$  to  $43$  ppm and  $-100$  to  $33\%$ .

**Table 5.4**

Comparison of the reduced order simulated and the experimental DOC outlet  $CO$ ,  $NO$ ,  $NO_2$  and  $HC$  concentrations for the active regeneration data

Experimental DOC Outlet					Simulated DOC Outlet					$\Delta NO_2$	
T °C	CO ppm	NO ppm	$NO_2$ ppm	HC ppmC	T °C	CO ppm	NO ppm	$NO_2$ ppm	HC ppmC	ppm	%
348	0	183	334	16	348	0	226	291	6	43	15
497	3	481	36	305	491	0	490	27	75	9	33
526	4	497	20	319	518	0	495	22	77	-2	-9
547	6	507	10	313	539	1	496	21	76	-11	-52
599	12	517	0	330	579	2	498	19	76	-19	-100
350	0	124	185	18	350	0	144	165	19	20	12
504	12	305	7	468	512	7	295	17	305	-10	-59
524	17	307	5	516	522	13	296	16	381	-11	-69
548	23	320	3	930	551	28	296	27	509	-24	-89
615	75	325	4	1104	599	47	296	33	627	-29	-88
326	0	130	175	34	327	0	150	156	30	19	12
509	58	301	8	1323	515	24	285	24	806	-16	-67
533	65	306	6	1426	543	37	285	27	914	-21	-78
557	80	310	5	1550	571	47	285	30	1063	-25	-83
597	140	312	7	1695	591	52	285	34	1226	-27	-79

## 5.4 SCR Reduced Order Model Calibration

The SCR reduced order model was simulated using the test point 8 to compare the reduced order model to the high fidelity model. The kinetic parameters identified in the high fidelity model [1,64] were used in the reduced order model. More details on the high fidelity model calibration and parameter identification process can be found in reference [1,63,64].

Figure 5.9 shows a comparison of the SCR outlet  $NO$ ,  $NO_2$  and  $NH_3$  concentrations between the experimental, high-fidelity model and the reduced order model. The first sub-

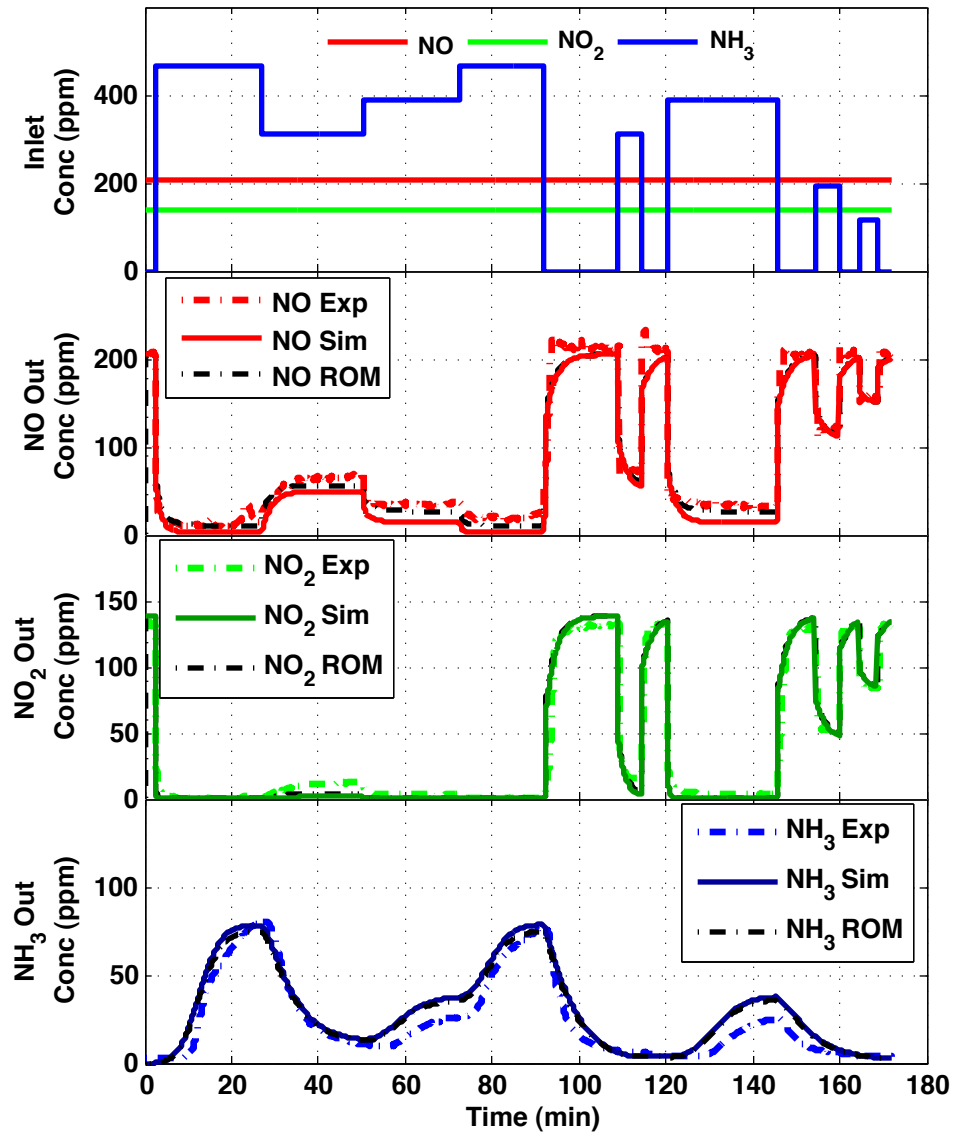


**Figure 5.9.** Comparison of the reduced order model with the experimental and high fidelity model results for test 8

plot shows the SCR inlet  $NH_3$ ,  $NO$  and  $NO_2$  concentrations. The  $NO$  and  $NO_2$  concentrations are maintained constant for the entire test and the inlet  $NH_3$  concentration is varied by controlling the urea injector located upstream of the SCR to achieve different levels of the  $NH_3/NO_X$  ratio. The second subplot shows the comparison of the SCR outlet  $NO$  concentration. It is observed that the reduced order model follows the experimental measured  $NO$  concentration profile with less than  $\pm 30$  ppm error. The third subplot shows the comparison of the SCR outlet  $NO_2$  concentration. Similar to  $NO$  the reduced order model follows the experimental measured  $NO_2$  concentration profile with less than  $\pm 20$  ppm error. The fourth subplot shows the comparison of the SCR outlet  $NH_3$  concentration. An exhaust sample line model described in reference [[1,64]] was used to simulate the effect of adsorption of the  $NH_3$  in the sample line. The reduced order model follows the experimental measured  $NH_3$  concentration profile with less than  $\pm 48$  ppm error.

5.10 shows a comparison of the SCR outlet  $NO$ ,  $NO_2$  and  $NH_3$  concentration between the experimental and the reduced order model for test point 2. The first subplot shows the SCR inlet  $NO$ ,  $NO_2$  and  $NH_3$  concentrations. The second subplot shows the comparison of the SCR outlet  $NO$  concentration. It is observed that the reduced order model follows the experimental measured  $NO$  concentration profile with less than  $\pm 40$  ppm error. The third subplot shows the comparison of the SCR outlet  $NO_2$  concentration. Similar to  $NO$ , the reduced order model follows the experimental measured  $NO_2$  concentration profile with less than  $\pm 20$  ppm error. The fourth subplot shows the comparison of the SCR outlet  $NH_3$  concentration. The reduced order model follows the experimental measured  $NH_3$  concentration profile with a maximum error of  $\pm 10$  ppm.

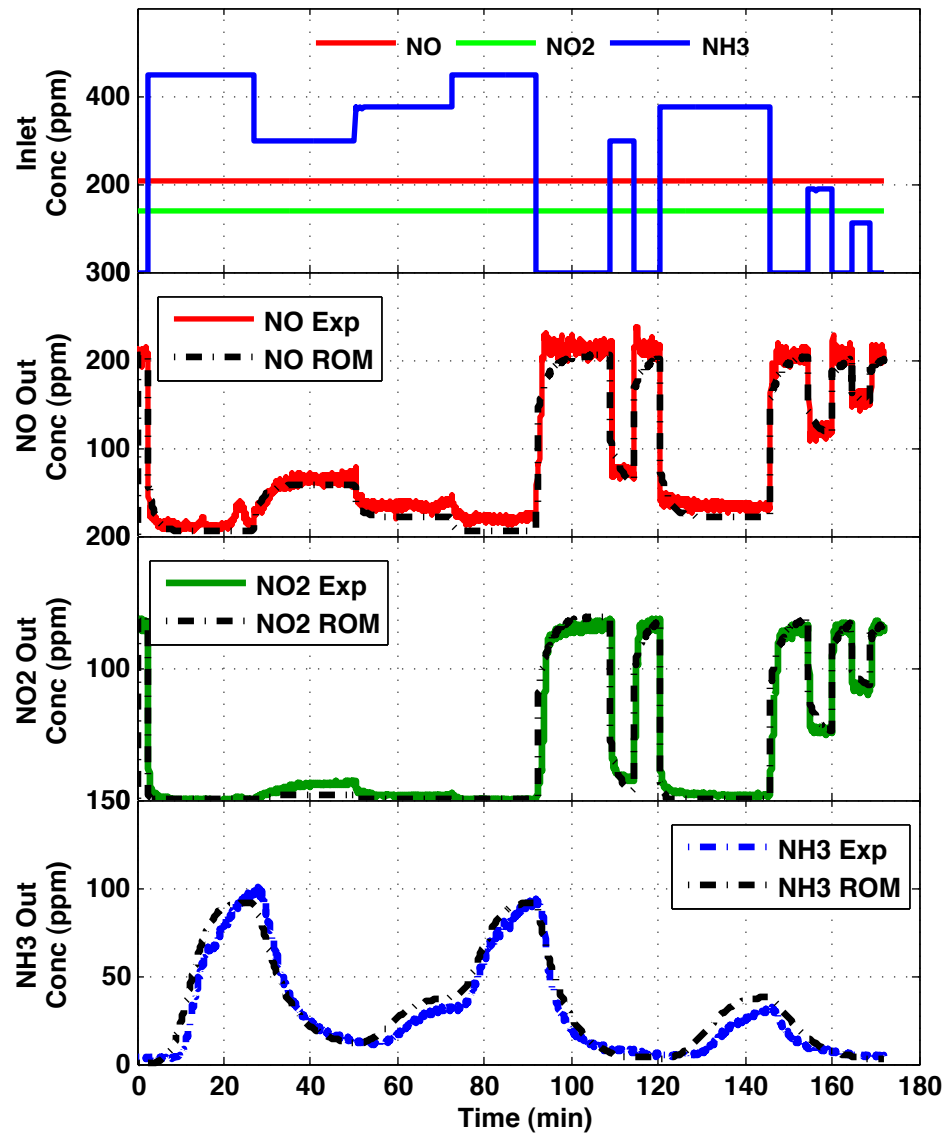


**Figure 5.10.** Comparison of the reduced order model with the experimental and high fidelity model results for test 2.

## **6. EXTENDED KALMAN FILTER (EKF)**

### **ESTIMATOR DEVELOPMENT**

This chapter describes the development of the EKF estimators for the DOC and SCR. To develop the EKF estimator, the reduced order DOC and SCR models described in Chapter 5 were used. An EKF estimator for a typical nonlinear discrete system and the implementation of the EKF strategy on the DOC and SCR reduced order models is described in chapter 2. The DOC and SCR EKF estimators are simulated on the surrogate FTP test described in Chapter 3 and the results are quantified.

#### **6.1 DOC Estimator Development**

An EKF state estimator, based on an 'N' axial element DOC model was developed. To implement the EKF on the DOC reduced order model, the species and energy balance equations were discretized using Euler expansion. The discretized species and energy balance



equations are shown in equations 6.1 and 6.2.

$$C_{i,r} = C_{i,r-1} - \frac{\Delta x}{\epsilon u} R R_i \quad (6.1)$$

$$i = CO, NO, C_3H_6$$

$$T_{r,k} = T_{r,k-1} - \frac{\rho u c_p}{\rho_s c_s + \rho c_v} \frac{\Delta t}{\Delta x} (T_{r,k} - T_{r-1,k}) + \frac{A_g \Delta t}{(\rho_s c_s + \rho c_v)(1 - \epsilon)} \sum_{i=CO}^{C_3H_6} \frac{\Delta h_i R R_i}{MW_i} \quad (6.2)$$

The states vector for the discrete system was defined as:

$$\vec{x}_k = \begin{Bmatrix} T_{1,k} \\ T_{2,k} \\ \cdot \\ \cdot \\ T_{r-1,k} \\ T_{r,k} \end{Bmatrix} \quad (6.3)$$

The process noise( $\vec{w}_k$ ) was neglected and the covariance matrix ( $R_k$ ) for the observation noise( $\vec{v}_k$ ) was constructed using a standard deviation of 0.1. To estimate the covariance matrix  $P_k^-$  the the jacobian  $F_k$  was calculated by differentiating equation 6.3.

## 6.2 DOC Estimator Simulation

The DOC estimator was simulated on active regeneration and transient data. The test setup, test matrix and the details of the testing are explained in the Experimental setup section of Chapter 3. The parameters needed for the estimator and their measurement

location and source of measurement is shown in Figure 6.1. The estimator uses the inlet mass flow rate, temperature, pressure,  $CO$ ,  $NO$ ,  $NO_2$ ,  $C_3H_6$  and  $O_2$  concentrations from the ECU maps along with the upstream  $NO_X$  and temperature measurements to estimate the  $CO$ ,  $NO$ ,  $NO_2$ ,  $C_3H_6$  and temperature states in the catalyst. For the results shown here, the number of axial elements in both the model and the estimator were fixed at  $N=15$ . The DOC state estimator and reduced order model use the same set of species balance and energy balance equations.

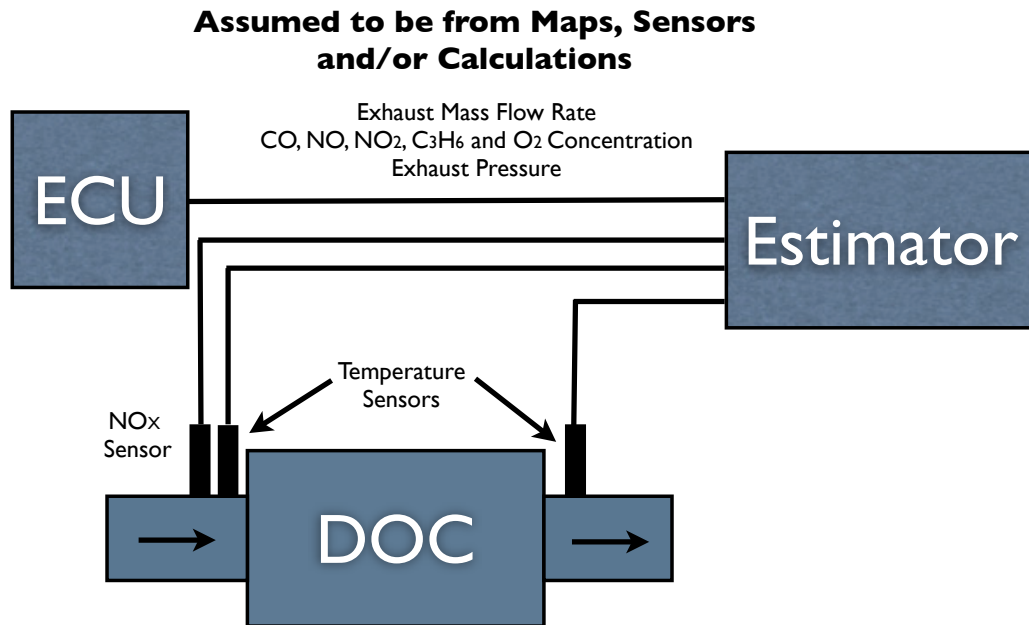


**Figure 6.1.** Schematic showing the inputs to the estimator from the sensors and ECU maps

### 6.2.1 Active Regeneration Test Case Simulation

The estimation goal is to compute  $NO$ ,  $NO_2$  and  $C_3H_6$  concentrations within the DOC during active regeneration of the CPF when the DOC inlet HC concentrations are between

9000 to 16000  $\text{ppm}_C$  and the temperature increase through the DOC is  $200 - 300^\circ\text{C}$ . Hence a test case representative of the active regeneration condition was used to simulate the estimator. A test case was constructed using an inlet mass flow rate of 0.95 kg/s, inlet temperature of  $300^\circ\text{C}$  and inlet concentrations of 434 ppm  $\text{NO}$ , 24 ppm  $\text{NO}_2$ , 53 ppm  $\text{CO}$  and 4500 ppm of  $\text{C}_3\text{H}_6$ . Along with these inputs, the estimator uses the downstream DOC temperature sensor measurement to estimate the states in the DOC. A simulated temperature sensor measurement was constructed using the DOC outlet temperature from the reduced order model. Figure 6.2 shows the simulated temperature sensor measurement with added Gaussian noise.

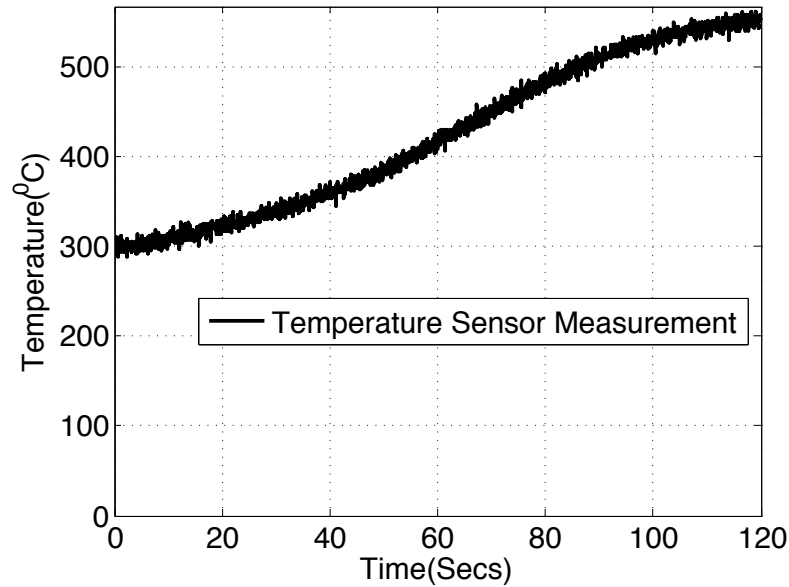


**Figure 6.2.** Simulated temperature sensor measurement with Gaussian noise for test case

The pre exponential factor for  $\text{HC}$  oxidation used in the estimator is 10% higher than the model. With 10% high pre exponential the initial temperature estimate of the estimator is higher than the model simulated DOC outlet temperature. The estimator uses the temperature signal generated using DOC reduced order model (Figure 6.2) and corrects the

estimated temperature. Figure 6.3 shows the comparison between the simulated and estimated hydrocarbon concentration and temperature at the 10<sup>th</sup> axial element of the DOC. The 10<sup>th</sup> element was selected to illustrate the ability of the estimator to predict concentrations and temperatures inside the DOC. In the following figures, simulated concentrations are plotted as a continuous line and the estimated concentrations are plotted with ‘+’ symbols. The estimated hydrocarbon concentration closely follows the simulated hydrocarbon concentration with the maximum error of less than 1.5%. In Figure 6.3, the estimated temperature follows the simulated temperature with the maximum error of less than 0.5%.

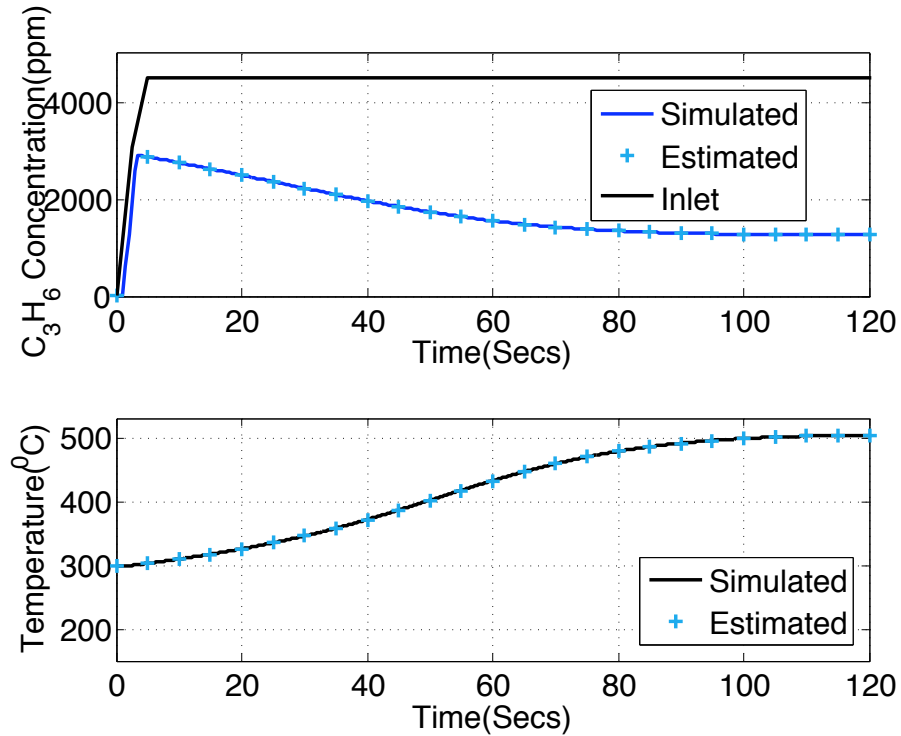


**Figure 6.3.** DOC inlet hydrocarbon concentration and a comparison between the simulated and estimated HC concentration and temperature at the 10<sup>th</sup> element

## 6.2.2 FTP Transient Cycle Simulation

The performance of the DOC estimator was also evaluated using a engine run with a surrogate FTP cycle. The surrogate FTP test [53] is a simplified FTP cycle which recreates the transients similar to that in an FTP cycle as explained in Chapter 3. For the estimator, the constants identified with the reduced order model were used to simulate the test . The performance of the estimator in open and closed loop is compared. When operated in open loop the estimator does not use the DOC outlet temperature measurement and performs as a DOC model. When operated in closed loop the estimator uses the DOC outlet temperature to correct the temperatures in the DOC.

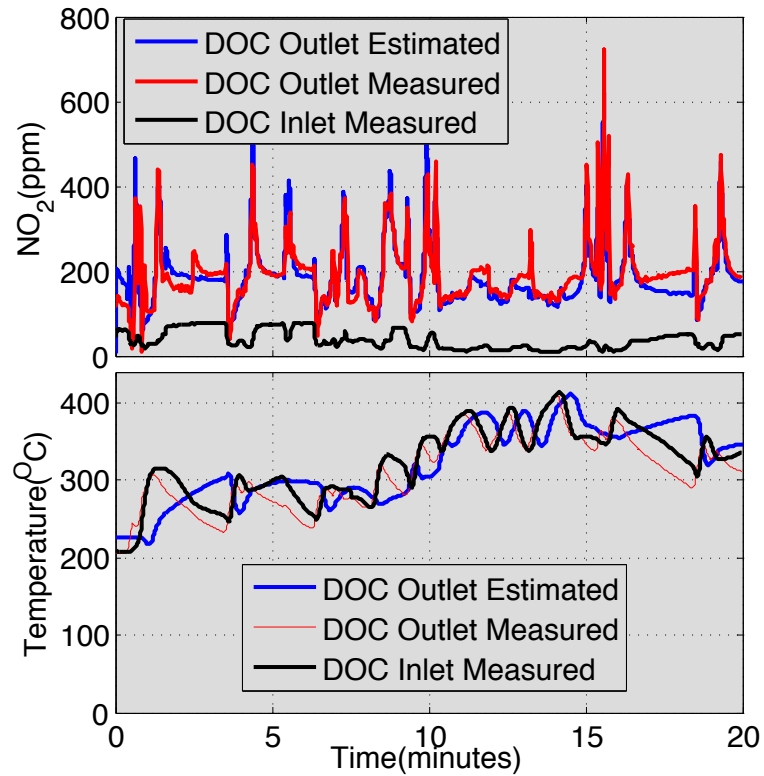


**Figure 6.4.** Comparison of the DOC outlet  $NO_2$  concentrations and temperatures with the estimator in open loop for the FTP cycle

Figure 6.4 shows the comparison of the DOC outlet  $NO_2$  concentrations and the outlet temperature for the surrogate FTP data. The estimator was operated in open loop by setting the optimal Kalman gain to zero. From the figure it can be observed that the estimator DOC outlet temperature does not follow the measured DOC outlet temperature. The temperature has a maximum error of 51%. The error in the temperatures translates to large errors (maximum of 50%) in the estimated DOC outlet  $NO_2/NO_X$  ratio. Clearly there is a need to operate in the closed loop.

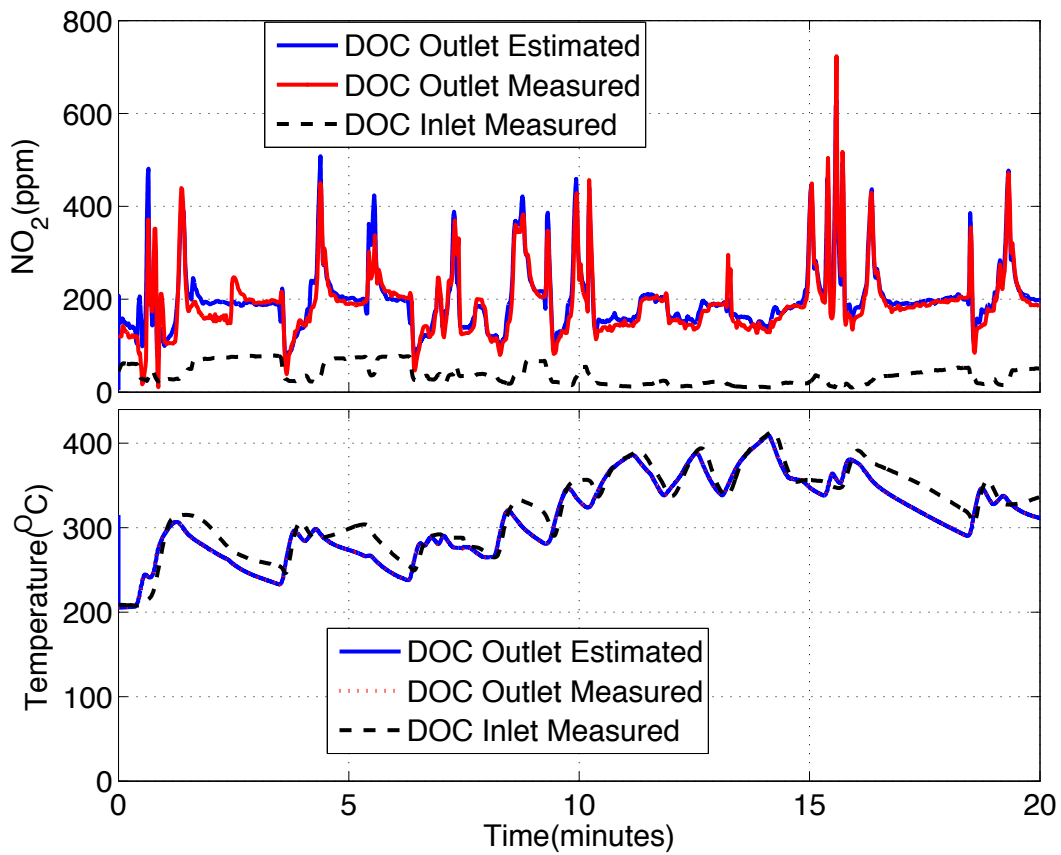


**Figure 6.5.** Comparison of the DOC outlet  $NO_2$  concentrations and temperatures with the estimator in closed loop for the FTP cycle

Figure 6.5 shows the comparison of the DOC  $NO_2$  concentrations for a closed loop

estimator. The DOC outlet temperature closely follows the response of the measured DOC outlet temperature with less than 0.1% error. With the accurate temperature estimate, the estimator agrees with the measured DOC outlet  $NO_2$  concentrations for most parts of the test with a maximum error of 26% and a typical error of less than 20 *ppm*.

Simulation of the high fidelity model on the surrogate FTP test showed that the heat transfer to ambient is important to predict the DOC outlet temperature. Eliminating the heat transfer to ambient in the reduced order model introduced errors in the transient temperature response of the DOC observed in the open loop simulation. In the closed loop simulation the estimator accounts the absence of heat transfer to ambient and reduces the error in the temperature.

### 6.3 SCR Estimator Development

The reduced order SCR model was used as the basis to implement the EKF estimation strategy. The estimator consist of the  $NH_3$  coverage fraction on site 1 an site 2 as the states and the concentration of  $NH_3$  ,  $NO$  ,  $NO_2$  and  $N_2O$  are outputs calculated based on the states. To implement the EKF estimation strategy, SCR the states for the SCR system is defined as:

$$\vec{x}_k = \begin{Bmatrix} \theta_{1,k} \\ \theta_{2,k} \\ \cdot \\ \cdot \\ \theta_{r-1,k} \\ \theta_{r,k} \end{Bmatrix} \quad (6.4)$$

To calculate the Jacobian matrix the relationship of  $\theta_1$  and  $\theta_2$  with  $NH_3$ ,  $NO$  and  $NO_2$  concentration was used. The details of the Jacobian matrix calculation is found in Appendix C. To implement an EKF on the SCR reduced order model, the process noise ( $w_k$ ) was neglected and a standard deviation of 0.1 was used to construct the covariance matrix ( $R_k$ ). Figure 6.6 shows a schematic of the SCR estimator with all the inputs needed. The SCR estimator uses the exhaust mass flow rate,  $NH_3$ ,  $NO$ ,  $NO_2$  and  $O_2$  concentrations from the engine maps along with the temperature and  $NO_X$  sensor upstream (or  $NO_X$  out of the CPF from a model) of the SCR and  $NH_3$  and/or  $NO_X$  sensor downstream of the SCR to estimate the states of the SCR. Figure 6.6 shows a schematic of the state estimator along with the inputs needed.

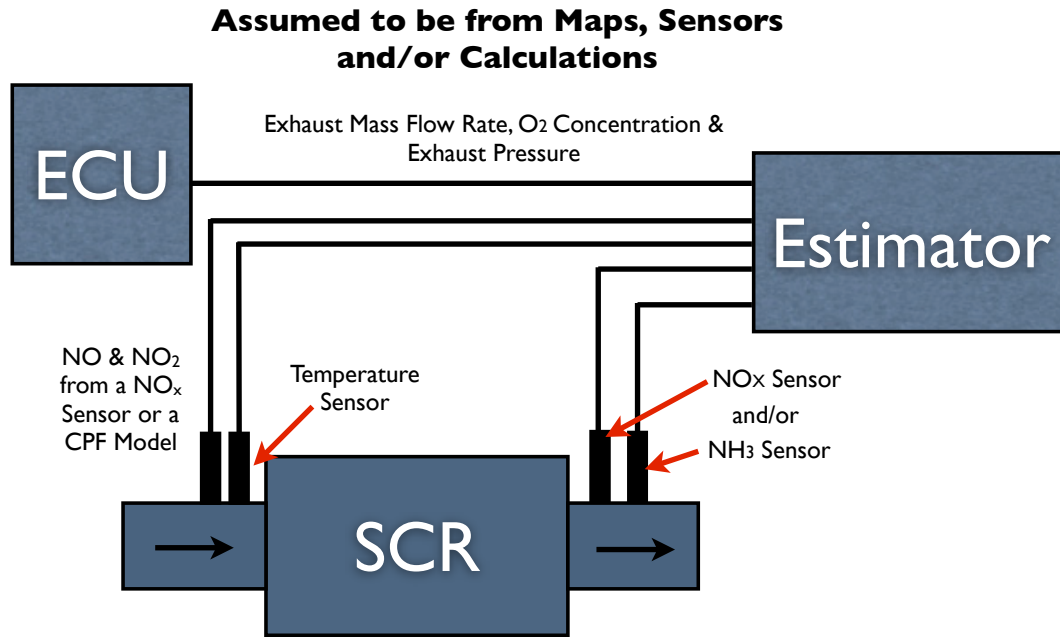


**Figure 6.6.** Schematic of the inputs to the SCR state estimator with the sensors downstream of the SCR

The model for the  $NO_X$  and  $NH_3$  sensors were developed using the experimental



measured concentrations of  $NO$ ,  $NO_2$  and  $NH_3$ . The model for the  $NO_X$  sensor was developed based on the  $NO_X$  sensor model described in reference[70]. The equation 6.5 describes the  $NO_X$  sensor model.

$$NO_X \text{ sensor} = a_0 + a_1 * NO + a_2 * NO_2 + a_3 * NH_3 \quad (6.5)$$

The constants  $a_0$ ,  $a_1$ ,  $a_2$  and  $a_3$  were identified using the surrogate FTP data described in chapter 3. More detailed description of the model and the calibration procedure is described in Appendix A. The  $NH_3$  sensor model is similar to the  $NO_X$  sensor model and is described in reference[1] and equation 6.6.

$$NH_3 \text{ sensor} = b_0 + b_1 * NO + b_2 * NO_2 + b_3 * NH_3 \quad (6.6)$$

$NH_3$  sensor sensitivity to  $NO$  and  $NO_2$  was found to be zero. Hence the constants  $b_0$ ,  $b_1$  and  $b_2$  were set to zero. The constant  $b_3$  was found to be 1.17.

## 6.4 SCR Estimator Simulation and the Effect of $NO_X$ and $NH_3$ Sensors on State Estimation Quality

The performance of the SCR estimator was evaluated using engine data from the surrogate FTP cycle and three different SCR outlet sensor configurations:  $NO_X$  only,  $NH_3$  only and both  $NO_X$  and  $NH_3$ . The surrogate FTP test [1,64] is a simplified FTP cycle which recreates the transients similar to that in an FTP cycle as explained in Chapter 3. For the estimator, the constants identified with the reduced order model were used to simulate the

test. The  $NO_X$  and  $NH_3$  sensor signals along with the measured inputs to the SCR were used as estimator model inputs.

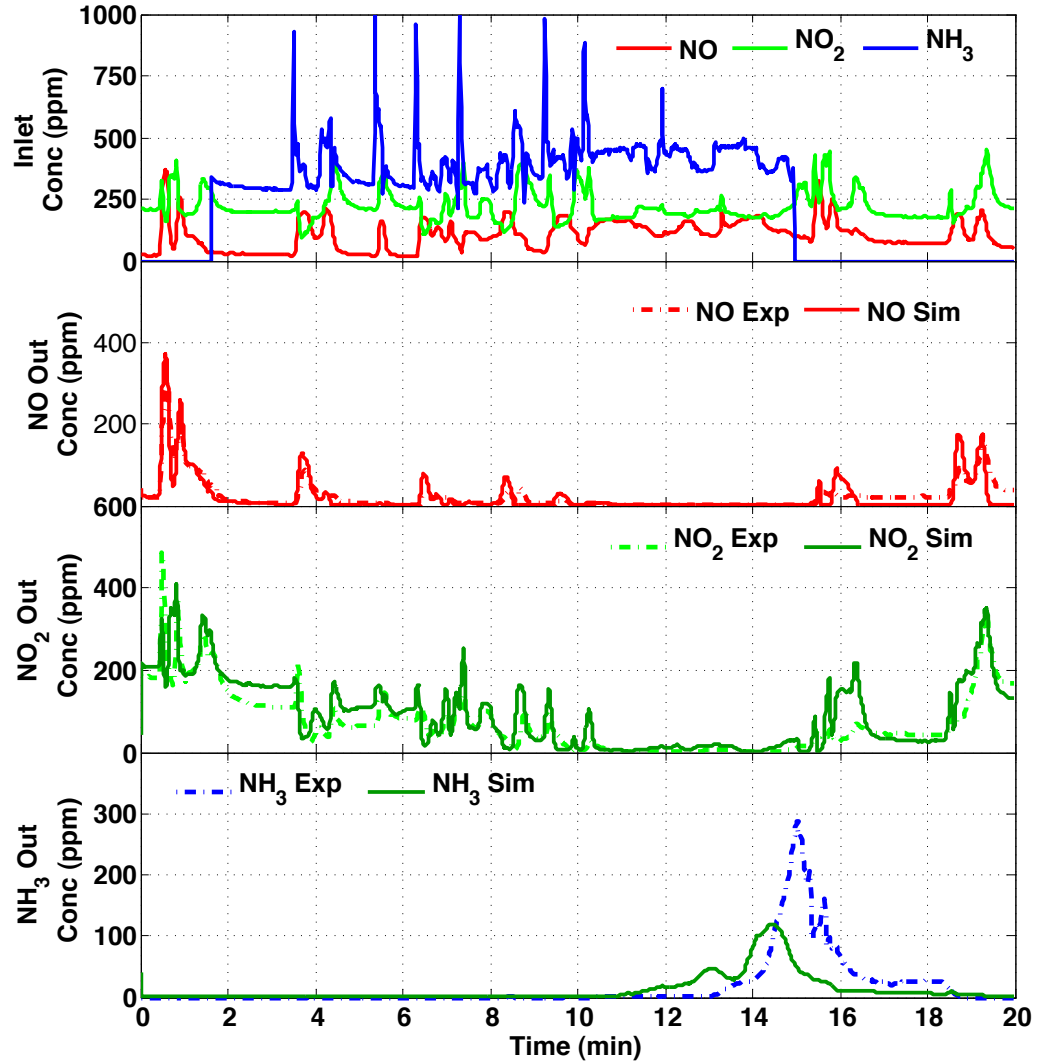


**Figure 6.7.** Comparison of the measured and estimated SCR outlet  $NO$  and  $NO_2$  concentrations and  $NH_3$  sensor signal for the FTP cycle with the estimator in open loop - without any sensors downstream of the SCR

Figure 6.7 shows a comparison of the SCR outlet  $NO$  and  $NO_2$  concentrations and  $NH_3$  sensor signal with the estimator in open loop. The estimator was operated in open

loop by setting the optimal Kalman gain to zero (the estimator does not use either the  $NO_X$  or  $NH_3$  sensor measurements). The SCR outlet  $NH_3$  sensor signal predicted by the estimator is lower than the measured value with the maximum error of  $\pm 226$  ppm and the fit for SCR outlet  $NO$  and  $NO_2$  concentration has a maximum error of  $\pm 150$  ppm.

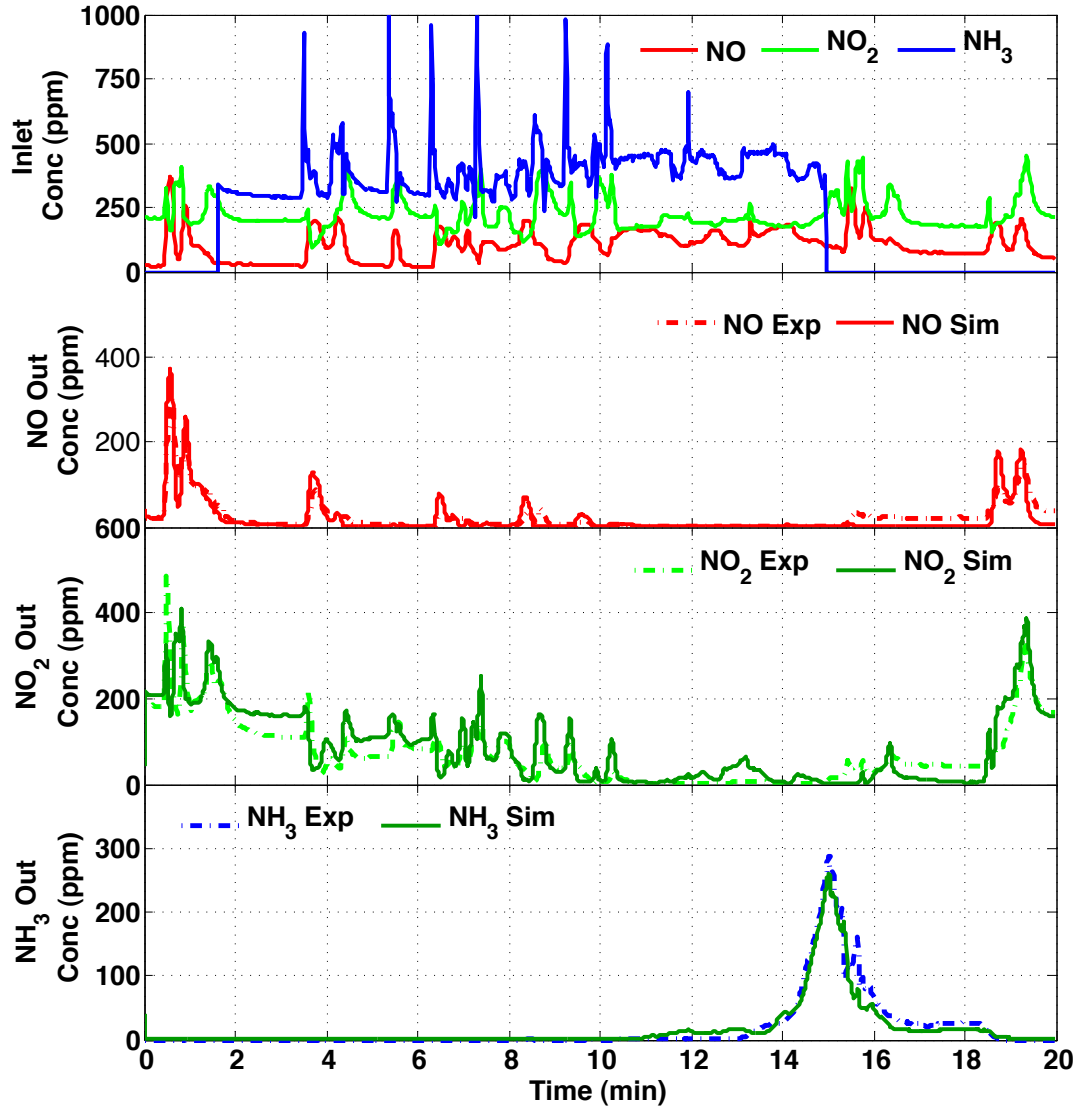


**Figure 6.8.** Comparison of the measured and estimated SCR outlet  $NO$  and  $NO_2$  concentrations and  $NH_3$  sensor signal for the FTP cycle with the estimator in closed loop - with both  $NO_X$  and  $NH_3$  sensor downstream of the SCR

The estimator was operated in closed loop and Figure 6.8 shows a comparison of the SCR outlet  $NO$  and  $NO_2$  concentrations and  $NH_3$  sensor signal. From the figure it can be observed that the estimator in closed loop simulates the SCR outlet  $NH_3$  sensor with a maximum error of  $\pm 24 \text{ ppm}$ . To reduce the error in the  $NO_X$  and  $NH_3$  sensor signals, the estimator changes the  $NH_3$  storage states. The open loop simulation of the estimator shows that the SCR estimator does not simulate the  $NH_3$  desorption accurately. When operated in closed loop, the estimator uses the sensor measurements to correct the  $NH_3$  desorption such that the error in the SCR outlet  $NO_X$  and  $NH_3$  sensors are reduced.

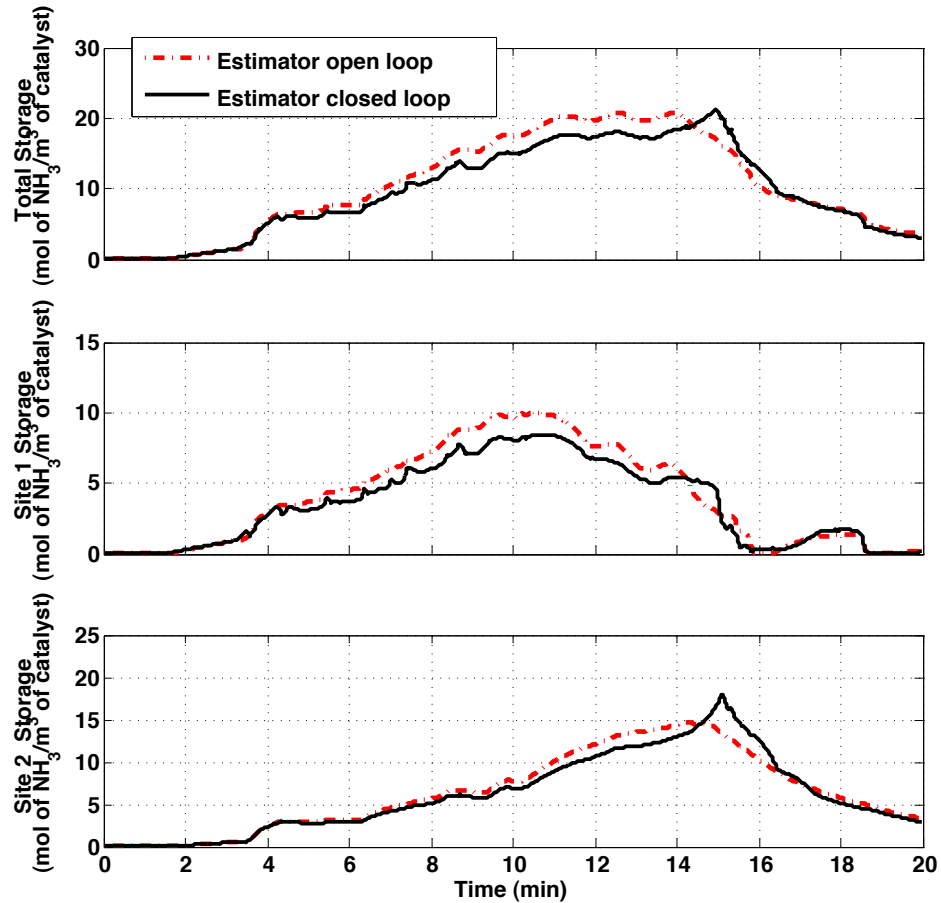


**Figure 6.9.** Comparison of the  $NH_3$  storage between an open loop and closed loop estimator for the FTP cycle - with both  $NO_X$  and  $NH_3$  sensor downstream.

Figure 6.9 shows a comparison of the  $NH_3$  storage estimate from the open loop and closed loop estimator. The figure shows the  $NH_3$  storage plotted as a function of time. The first subplot shows the total stored  $NH_3$  and the second and third subplot shows the  $NH_3$  stored for site 1 and site 2. The plot shows that the estimated  $NH_3$  storage is similar to that of the reduced order model. With the improved  $NH_3$  storage estimate, the estimator reduced the error in the  $NO$   $NO_2$  and  $NH_3$  concentrations at the SCR outlet.

With the improved estimate of the  $NH_3$  storage the error in the  $NO$  and  $NO_2$  concentration is reduced from  $\pm 150 \text{ ppm}$  to  $\pm 75 \text{ ppm}$  and the error in  $NH_3$  concentration is reduced from  $\pm 226 \text{ ppm}$  to  $\pm 24 \text{ ppm}$ .

#### 6.4.1 Effect of $NO_X$ and $NH_3$ Sensors on State Estimator

The objective of this part of the study is to evaluate the effect of sensors on the state estimation quality. Based on the available sensors there are three possible sensor combinations that can be used for the SCR state estimator at the outlet of the SCR. The possible sensor combinations are:

1. Both  $NH_3$  and  $NO_X$  sensors.
2.  $NO_X$  sensor only.
3.  $NH_3$  sensor only.

Figure 6.8 showed the results from case 1, with both  $NH_3$  and  $NO_X$  sensors at the SCR outlet. With both  $NH_3$  and  $NO_X$  sensors at the SCR outlet, the error in the SCR outlet  $NH_3$  sensor is less than  $\pm 26 \text{ ppm}$ .

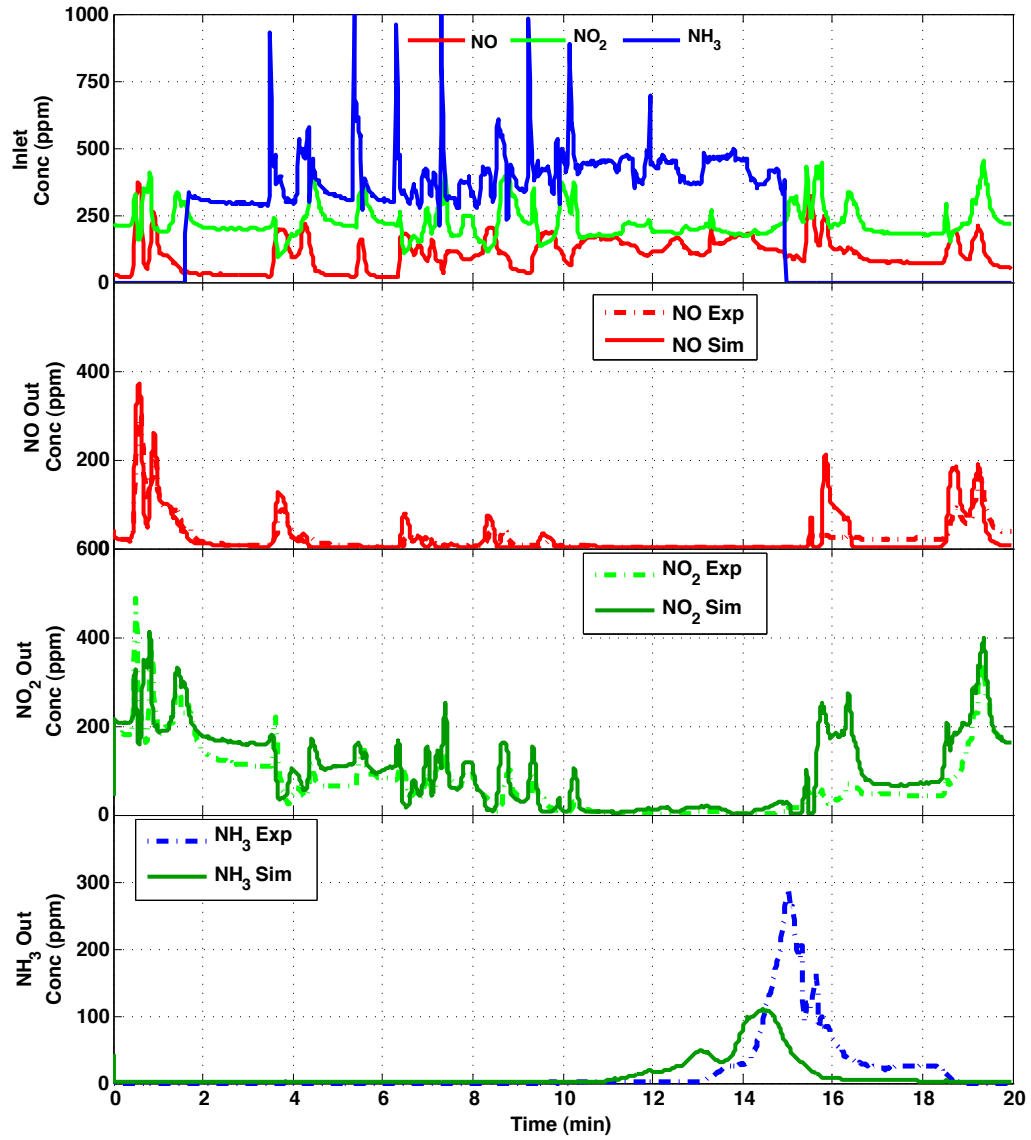


**Figure 6.10.** Comparison of the measured and estimated SCR outlet  $NO$  and  $NO_2$  concentrations and  $NH_3$  sensor signal for the FTP cycle - with just  $NO_X$  sensor downstream.

Figure 6.10 shows the plot of SCR outlet  $NO$ ,  $NO_2$  concentrations and  $NH_3$  sensor signal for case 2 where the estimator uses only the  $NO_X$  sensor at the SCR outlet. The plot shows that with just the  $NO_X$  sensor downstream of SCR, the maximum error in the esti-

mate of the  $NH_3$  sensor signal of  $\pm 216$  ppm which is seven times the error observed in case 1. The maximum errors are as follows  $NO$  concentration  $\pm 177$  ppm,  $NO_2$  concentration  $\pm 192$  ppm and  $NH_3$  sensor signal  $\pm 216$  ppm.

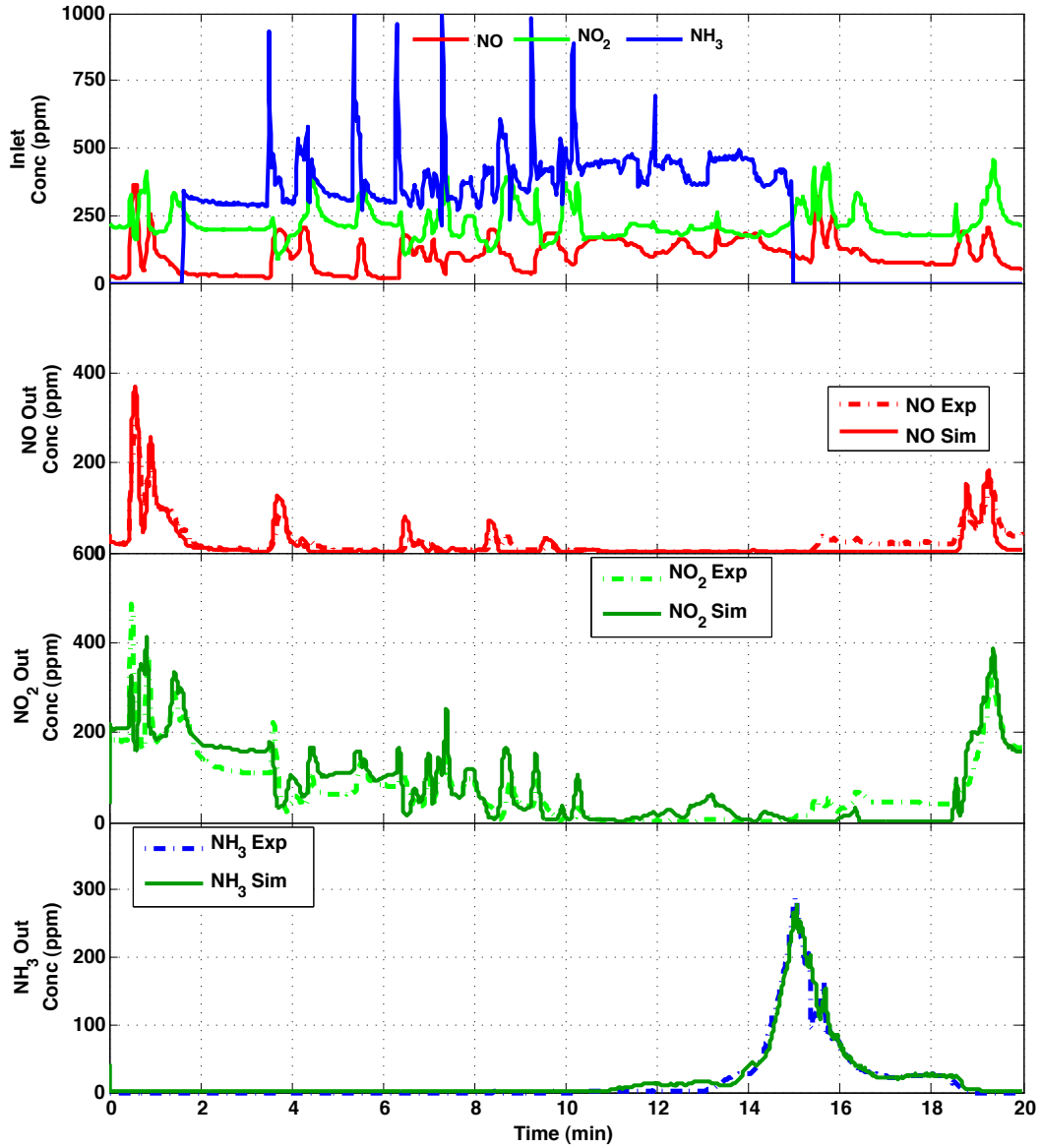


**Figure 6.11.** Comparison of the measured and estimated SCR outlet  $NO$  and  $NO_2$  concentrations and  $NH_3$  sensor signal for the FTP cycle - with just  $NH_3$  sensor downstream.

Figure 6.11 shows the plot of SCR outlet  $NO$ ,  $NO_2$  concentrations and  $NH_3$  sensor signal for case 3 where the estimator uses only the  $NH_3$  sensor at the SCR outlet. The plot shows that with just the  $NH_3$  sensor downstream of SCR, the maximum error in the estimate of the  $NH_3$  sensor signal is  $\pm 40$  ppm which is higher than case 1 but lower than case 2. The maximum error in the  $NO$  concentration is  $\pm 72$  ppm and the  $NO_2$  concentration is  $\pm 125$  ppm.

**Table 6.1**

Maximum errors and the standard deviation of the errors between the measured and estimated SCR outlet concentrations with  $NO_X$  sensor,  $NH_3$  sensor and both  $NO_X$  and  $NH_3$  sensors for the surrogate FTP cycle.

<b>Sensors</b>	<b>Maximum Error(ppm)</b>			<b>Standard Deviation (ppm)</b>		
	$NO_X$	$NH_3$	$NO_X$ and $NH_3$	$NO_X$	$NH_3$	$NO_X$ and $NH_3$
<b>Error <math>NO</math></b>	177	72	75	27	19	20
<b>Error <math>NO_2</math></b>	193	125	80	46	40	33
<b>Error <math>NH_3</math></b>	216	76	24	38	8	5

Table 6.1 shows the tabulated values of the maximum errors in the  $NO$ ,  $NO_2$  concentrations and  $NH_3$  sensor signal along with standard deviation in the errors for the three sensor combinations of  $NO_X$  sensor only,  $NH_3$  sensor only and both  $NO_X$  and  $NH_3$  sensors. The case with the just the  $NO_X$  sensor at the SCR outlet has the maximum errors in  $NO$ ,  $NO_2$  concentrations and  $NH_3$  sensor signal and the case with both  $NO_X$  and  $NH_3$  sensors at the SCR outlet has the least error and the case with just the  $NH_3$  sensor has errors in the middle. The standard deviation in the errors is maximum for  $NO_X$  sensor only situation and minimum for both the  $NO_X$  and  $NH_3$  sensor case.

The possible reason for the poor performance of the  $NO_X$  sensor only case is the presence of the  $NH_3$  in the exhaust after 12 minutes.  $NO_X$  sensor model results in Appendix A also show that the  $NO_X$  sensor model does not perform well in presence of the  $NH_3$



in the exhaust. So to further evaluate the performance of the sensors the test is separated to two sections: no  $NH_3$  at the SCR outlet and  $NH_3$  at the SCR outlet. Table 6.2 shows the comparison of the maximum errors and the standard deviation in the error when the test is divided to two sections. The table shows that for the 0 – 12 minutes section of the test the maximum and standard deviation of the errors in  $NO$  and  $NO_2$  concentrations between the  $NO_X$  and  $NH_3$  sensor only cases are the same, but the  $NH_3$  sensor only case has maximum error of  $15ppm$  in  $NH_3$  sensor signal compared to  $44ppm$  for the  $NO_X$  sensor only case. In the  $NH_3$  sensor case even though the estimator is correcting the storage based on the  $NH_3$  sensor measurement, the magnitude of the corrections are small and do not affect the  $NO$  and  $NO_2$  conversion across the SCR. But with the information from the  $NH_3$  sensor the estimator does reduce the error in  $NH_3$  concentration to  $15ppm$ . This can be observed in Table 6.2 where the  $NO_X$  sensor and  $NH_3$  sensor cases both have the same maximum error and standard deviation in the error in the  $NO$  and  $NO_2$  concentrations. The results between 12 – 20 minutes show that the maximum and standard deviation of the errors in  $NO$ ,  $NO_2$  concentrations and  $NH_3$  sensor signal for the  $NO_X$  sensor only case is higher than the  $NH_3$  sensor only and both  $NH_3$  and  $NO_X$  sensor case. Based on the results it can be concluded that the under lower  $NH_3$  slip conditions both  $NO_X$  and  $NH_3$  sensor performance is similar and cross sensitivity of the  $NO_X$  sensor to  $NH_3$  at higher  $NH_3$  concentrations is responsible for the higher errors in the  $NO_X$  sensor only case.

**Table 6.2**

Maximum errors and the standard deviation of the errors between the measured and estimated SCR outlet concentrations with  $NO_X$  sensor,  $NH_3$  sensor and both  $NO_X$  and  $NH_3$  sensors for the surrogate FTP cycle for two sections of the test

0-12 minutes						
	Maximum Error(ppm)			Standard Deviation of Error(ppm)		
	$NO_X$ Sensor	$NH_3$ Sensor	$NH_3$ and $NO_X$ sensor	$NO_X$ Sensor	$NH_3$ Sensor	$NH_3$ and $NO_X$ sensor
$NO$	76	76	75	19	19	19
$NO_2$	135	135	80	40	40	35
$NH_3$	44	15	0.35	3	3	3

12-20 minutes						
	Maximum Error(ppm)			Standard Deviation of Error(ppm)		
	$NO_X$ Sensor	$NH_3$ Sensor	$NH_3$ and $NO_X$ sensor	$NO_X$ Sensor	$NH_3$ Sensor	$NH_3$ and $NO_X$ sensor
$NO$	177	61	36	27	17	19
$NO_2$	193	84	104	45	35	30
$NH_3$	216	82	25	34	13	7

## 7. SUMMARY AND CONCLUSIONS

The DOC high fidelity model was developed to simulate the DOC during steady-state and active regeneration conditions. The DOC model simulates the oxidation of  $CO$ ,  $NO$  and  $HC$  across the DOC. The DOC model simulates the gas and surface phase, mass and energy balance equations, which are limited by the mass and heat transfer coefficients. The DOC model was simulated to the steady state test data for three space velocities and active regeneration data with different DOC inlet  $HC$  concentrations. The model is unable to match the  $CO$  production during active regeneration due to the absence of a  $CO$  production reaction in the model. The kinetic parameters for the  $CO$ ,  $NO$  and  $HC$  oxidation reactions were identified. The inhibition factors associated with  $HC$  oxidized were needed to simulate the experimental data from the active regeneration experiments. The DOC model was simulated on the transient surrogate FTP test. To simulate the DOC model on the transient surrogate FTP test, the heat transfer to ambient was necessary in order to simulate the outlet temperature. The model results shows higher  $HC$  concentration at the DOC outlet during the transient test compared to the experimental data. To simulate the DOC on the aged DOC data, the pre exponential factor for  $NO$  oxidation was reduced to 78% lower. A procedure to calibrate the DOC model was developed and is described.

DOC reduced order was developed based on the high fidelity model. The assumptions

used in the model reduction resulted in the elimination of the heat and mass transfer coefficients from the differential equations. The DOC reduced order model simulates the oxidation of  $CO$ ,  $NO$  and  $HC$  in the exhaust. The reduced order model was simulated on the steady state and active regeneration data. The results showed that including the inhibition effect of  $NO$  on the oxidation reactions is sufficient to simulate the experimentally observed  $CO$ ,  $NO$  and  $HC$  conversion efficiencies.

The DOC estimator was developed by applying EKF state estimation strategy to the DOC reduced order model. The DOC estimator uses the DOC inlet  $CO$ ,  $NO$ ,  $NO_2$  and  $HC$  concentrations, DOC inlet temperature, mass flow rate, inlet pressure and the DOC outlet temperature to estimate the concentrations of  $CO$ ,  $NO$ ,  $NO_2$  and  $HC$  and the temperatures in the DOC. The DOC estimator was simulated on the surrogate FTP test. The errors in the estimator performance with and without the DOC outlet temperature measurements were quantified.

An SCR reduced order model was derived from the SCR high fidelity model [1]. The SCR reduced order model simulates the  $NH_3$  storage and  $NO_X$  reduction reactions. The SCR reduced order model was simulated on the steady state engine data and compared to the high fidelity model and the experimental data. The results from the simulation were quantified in terms of error in the SCR outlet  $NO$ ,  $NO_2$  and  $NH_3$  concentrations.

The SCR reduced order model was used to develop an EKF estimator for the SCR. The EKF estimator uses the SCR inlet  $NO$ ,  $NO_2$ ,  $O_2$  and  $NH_3$  concentrations, temperature, exhaust mass flow rate and pressure along with the  $NO_X$  and/or  $NH_3$  sensor at the SCR outlet to estimate the  $NH_3$  storage and  $NO$ ,  $NO_2$  and  $NH_3$  concentrations in the SCR. The SCR estimator was simulated on the surrogate FTP data. The estimator is able to correct for the  $NH_3$  concentration measured at the SCR outlet and estimate the  $NO$ ,  $NO_2$ ,  $NH_3$

and  $NH_3$  storage states of the SCR. The effect of the  $NO_X$  and  $NH_3$  sensors on the state estimation quality were quantified in terms of the maximum error and standard deviation in the SCR outlet concentrations.

## 7.1 DOC Estimation

Based on the results of simulating the DOC high fidelity model, reduced order model and estimator on the experimental data the following conclusions can be made:

1. The DOC high fidelity and reduced order model is able to simulate the experimental  $HC$ ,  $CO$  and  $NO$  conversion across the DOC during steady state and active regeneration conditions.
2. To simulate the DOC outlet temperature,  $\frac{NO_2}{NO_X}$  ratio and  $CO$  concentration the transient cycle, heat transfer to the ambient was added.
3. The results for aged data high fidelity model simulation shows that reactions in an aged DOC have activation energies similar to the degreened DOC, but the pre exponential factors are 78% lower for the  $NO$  oxidation reaction.
4. The reduced order DOC model simulation results show that the effect of order reduction on  $HC$ ,  $CO$  and  $NO$  conversion is not significant.
5. The DOC estimator simulation on active regeneration data shows that it is possible to estimate the DOC outlet  $HC$  concentration with a temperature measurement at the DOC outlet.

6. The results from simulating the closed loop estimator simulation on the surrogate FTP cycle shows that the DOC estimator is able to reduce the error in temperatures to less than 0.1%.
7. The improved temperature estimate from the closed loop estimator results in a reduced error (maximum error reduced from 50% to 26%) in the  $NO_2$  concentration estimate compared to the open loop estimator on the surrogate FTP cycle test.

## 7.2 SCR Estimation

Based on the results of simulating the SCR high fidelity model, reduced order model and estimator on the experimental data, the following conclusions can be made:

1. The reduced order SCR model agrees with the experimental and high fidelity model  $NO$ ,  $NO_2$  and  $NH_3$  concentrations at the SCR outlet within  $\pm 40$  ppm for  $NO$  and  $NO_2$  and  $\pm 10$  ppm for  $NH_3$ .
2. The closed loop estimator using a  $NO_X$  and  $NH_3$  sensor downstream is able to provide an accurate estimate of the  $NO$ ,  $NO_2$ ,  $NH_3$  and  $NH_3$  storage in the SCR with less than  $\pm 80$  ppm error in  $NO$ ,  $NO_2$  and  $NH_3$  concentrations.
3. With  $NH_3$  and  $NO_X$  sensors at the SCR outlet, the estimator is able to estimate the  $NH_3$  concentration at the SCR outlet with a maximum error of 24 ppm. With only a  $NO_X$  sensor at the SCR outlet, the estimator has 9 times higher error in the estimated  $NH_3$  concentration at the SCR outlet compared to the  $NH_3$  and  $NO_X$  sensor combination with a maximum error of 216 ppm. With just the  $NH_3$  sensor at

the SCR outlet, the estimator is able to estimate the  $NH_3$  concentrations at the SCR outlet with a maximum error of 76 ppm. The  $NH_3$  sensor improves the ability of the SCR EKF estimator to estimate  $NH_3$  storage.

4. Under lower  $NH_3$  slip conditions both  $NO_X$  and  $NH_3$  sensor performance is similar and cross sensitivity of the  $NO_X$  sensor to  $NH_3$  at higher  $NH_3$  concentrations is responsible for the higher errors in the  $NO_X$  sensor only case.

## REFERENCES

- (1) X. Song, *A SCR Model Based on Reactor and Engine Experimental Studies for a Cu-zeolite Catalyst*. PhD thesis, Michigan Technological University, 2013.
- (2) <http://www.dieselnet.com/standards/us/hd.php>, *Heavy-Duty Truck and Bus Engines-Emission Standards*. The Internet: Diesel Net, 2012.
- (3) E. P. Agency, *Greenhouse Gas Emissions Standards and Fuel Efficiency Standards for Medium- and Heavy-Duty Engines and Vehicles*. Federal Register, September 15, 2011.
- (4) <http://www.dieselnet.com/standards/us/obd.php>, *Emission Standards: United States-On-Board Diagnostics*. Diesel Net, 2012.
- (5) R. H. Dabhoiwala, J. H. Johnson, J. D. Naber, and S. T. Bagley, “Experimental and Modeling Results Comparing Two Diesel Oxidation Catalyst - Catalyzed Particulate Filter Systems,” *SAE Technical Paper*, vol. 2008-01-0484, 2008.
- (6) Ronny Allansson and Philip G. Blakeman and Barry J. Cooper and Howard Hess and Peter J. Silcock and Andrew P. Walker, “Optimising the Low Temperature Performance and Regeneration Efficiency of the Continuously Regenerating Diesel Partic-



- ulate Filter (CR-DPF) System,” *SAE Technical Paper*, vol. 2002-01-0428, pp. doi: 10.4271/2002-01-0428, 2002.
- (7) S. Mueller and W. Troeger, “Diagnostic and Control Systems for Automotive Power Electronics,” *SAE Technical Paper*, vol. 2001-01-0075, 2001.
  - (8) Q. Song and G. Zhu, “Model-based Closed-loop Control of Urea SCR Exhaust Aftertreatment System for Diesel Engine,” *SAE Technical Paper*, vol. 2002-01-0287, 2002.
  - (9) R. Stobart, “Control Oriented Models for Exhaust Gas Aftertreatment; A Review and Prospects,” *SAE Technical Paper*, vol. 2003-01-1004, 2003.
  - (10) C. M. Schlar, C. H. Onder, H. P. Geering, and M. Elsener, “Control-Oriented Model of an SCR Catalytic Converter System,” *SAE Technical Paper*, vol. 2004-01-0153, 2004.
  - (11) L. Hofmann, K. Rusch, S. Fischer, and B. Lemire, “Onboard Emissions Monitoring on a HD Truck with an SCR System Using  $NO_X$  Sensors,” *SAE Technical Paper*, vol. 2004-01-1290, 2004.
  - (12) J. N. Chi and H. F. M. Dacosta, “Modeling and Control of a Urea-SCR Aftertreatment System,” *SAE Technical Paper*, vol. 2005-01-0966, 2005.
  - (13) J. Nebergall, E. Hagen, and J. Owen, “Selective Catalytic Reduction On-Board Diagnostics: Past and Future Challenges,” *SAE Technical Paper*, vol. 2005-01-3603, 2005.
  - (14) F. Willems, R. Cloudt, E. van den Eijnden, M. van Genderen, R. Verbeek, B. de Jager, W. Boomsma, and I. van den Heuvel, “Is Closed-Loop SCR Control Required to Meet Future Emission Targets?,” *SAE Technical Paper*, vol. 2007-01-1574, 2007.

- (15) D. Y. Wang, S. Yao, M. Shost, J.-H. Yoo, D. Cabush, D. Racine, R. Cloudt, and F. Willems, "Ammonia Sensor for Closed-Loop SCR Control," *SAE Technical Paper*, vol. 2008-01-0919, 2008.
- (16) M. Devarakonda, G. G. Parker, J. H. Johnson, and V. Strots, "Model-Based Estimation and Control System Development in a Urea-SCR Aftertreatment System," *SAE Int. J. Fuels Lubr*, vol. 2008-01-1324, pp. doi: 10.4271/2008-01-1324, 2008.
- (17) J. N. Chi, "Control Challenges for Optimal NO<sub>x</sub> Conversion Efficiency from SCR Aftertreatment Systems," *SAE Technical Paper*, vol. 2009-01-0905, 2009.
- (18) A. Herman, M.-C. Wu, D. Cabush, and M. Shost, "Model Based Control of SCR Dosing and OBD Strategies with Feedback from  $NH_3$  Sensors," *SAE Technical Paper*, vol. 2009-01-0911, 2009.
- (19) C. Ong, A. Annaswamy, I. V. Kolmanovsky, P. Laing, and D. Reed, "An Adaptive Proportional Integral Control of a Urea Selective Catalytic Reduction System based on System Identification Models," *SAE Technical Paper*, vol. 2010-01-1174, 2009.
- (20) G. J. Bartley, C. J. Chadwell, T. M. Kostek, and R. Zhan, "SCR Deactivation Kinetics for Model-Based Control and Accelerated Aging Applications," *SAE Technical Paper*, vol. 2012-01-1077, 2012.
- (21) A. Frobert, S. Raux, Y. Creff, and E. Jeudy, "About Cross-Sensitivities of NO<sub>x</sub> Sensors in SCR Operation," *SAE Technical Paper*, vol. 2013-01-1512, 2013.
- (22) H. Na, D. Reed, A. Annaswamy, P. M. Laing, and I. Kolmanovsky, "Control-oriented Reduced-order Models for Urea Selective Catalytic Reduction Systems Using a Physics-based Approach," *SAE Technical Paper*, vol. 2011-01-1326, pp. doi: 10.4271/2011-01-1326, 2011.

- (23) M. F. Hsieh and J. Wang, “An Extended Kalman Filter for Ammonia Coverage Ratio and Capacity Estimations in the Application of Diesel Engine SCR Control and Onboard Diagnosis,” *American Control Conference*, Marriott Waterfront, Baltimore, MD, USA, 2010.
- (24) M. F. Hsieh and J. Wang, “An Extended Kalman Filter for  $NO_X$  Sensor Cross Sensitivity Elimination in Selective Catalytic Reduction Applications,” *American Control Conference*, Marriott Waterfront, Baltimore, MD, USA, 2010.
- (25) M.-F. Hsieh, *Control of Diesel Engine Urea Selective Catalytic Reduction Systems*. PhD thesis, The Ohio State University, 2010.
- (26) K. Irani, W. Epling, and R. Blint, “Effect of Hydrocarbon Species on NO Oxidation over Diesel Oxidation Catalysts,” *Applied Catalysis B: Environmental*, vol. 92, pp. 422–428, 2009.
- (27) C. Henry, N. Currier, N. Ottinger, and A. Yezerets, “Decoupling the Interactions of Hydrocarbons and Oxides of Nitrogen Over Diesel Oxidation Catalysts,” *SAE Technical Paper*, vol. 2011-01-1137, pp. doi: 10.427/2011–01–1137, 2011.
- (28) H. S. Surenahalli, K. C. Premchand, J. H. Johnson, and G. G. Parker, “Modeling Study of Active Regeneration of a Catalyzed Particulate Filter Using One-Dimensional DOC and CPF Models,” *SAE Technical Paper*, vol. 2011-01-1242, pp. doi:10.427/2011–01–1242, 2011.
- (29) H. S. Surenahalli, “A Modeling Study of a Diesel Oxidation Catalyst and Catalyzed Particulate Filter During Loading and Active Regeneration,” Master’s thesis, Michigan Technological University, 2010.

- (30) M. Zheng and S. Banerjee, “Diesel oxidation catalyst and particulate filter modeling in active D Flow configurations,” *Applied Thermal Engineering*, vol. 29, Issues 14&15, pp. 3021–3035, October 2009.
- (31) T. C. Watling, M. Ahmadinejad, M. ?u?uianu, Åsa Johansson, and M. A. Paterson, “Development and Validation of a Pt-Pd Diesel Oxidation Catalyst Model,” *SAE Technical Paper*, vol. 2011-01-1286, 2012.
- (32) F. Lafossas, Y. Matsuda, A. Mohammadi, A. Morishima, M. Inoue, M. Kalogirou, G. Koltsakis, and Z. Samaras, “Calibration and Validation of a Diesel Oxidation Catalyst Model: from Synthetic Gas Testing to Driving Cycle Applications,” *SAE Technical Paper*, vol. 2011-01-1244, 2011.
- (33) M. N. Devarakonda, *Dynamic Modeling, Simulation and Development of Model-Based Control Strategies in a Urea-SCR Aftertreatment System in Heavy Duty Diesel Engines*. PhD thesis, Michigan Technological University, 2007.
- (34) S. B. Deland, “Development and Parameter Identification of An Iron-Zeolite SCR Catalyst Model Using Reactor Data,” Master’s thesis, Michigan Technological University, 2010.
- (35) A. Herman, M.-C. Wu, D. Cabush, and M. Shost, “ Model Based Control of SCR Dosing and OBD Strategies with Feedback from NH<sub>3</sub> Sensors,” *SAE Int. J. Fuels Lubr.* 2(1), vol. SAE Technical Paper, 2009-01-0911, pp. 375–385, 2009.
- (36) R. Zhan, Y. Huang, and M. Khair, “Methodologies to Control DPF Uncontrolled Regenerations,” *SAE Technical Paper*, vol. 2006-01-1090, 2006.
- (37) M. Bouchez and J. B. Dementhon, “Strategies for the Control of Particulate Trap Regeneration,” *SAE Technical Paper*, vol. 2000-01-0472, 2000.

- (38) N. Singh, J. Johnson, G. Parker, and Song-LinYang, "Vehicle Engine Aftertreatment System Simulation (VEASS) Model: Application to a Controls Design Strategy for Active Regeneration of a Catalyzed Particulate Filter," *SAE Technical Paper*, vol. 2005-01-0970, 2005.
- (39) N. Birkby, S. Beesley, A. Hatton, and H. El-Khatib, "The Development and Testing of an Active Particulate Regeneration System Using Model Based Control," *SAE Technical Paper*, vol. 2006-01-3258, 2006.
- (40) N. Nagar, X. He, V. Iyengar, N. Acharya, A. Kalinowski, A. Kotrba, T. Gardner, and A. Yetkin, "Real Time Implementation of DOC-DPF Models on a Production-Intent ECU for Controls and Diagnostics of a PM Emission Control System," *SAE Int. J. Commer. Veh.* 2(2):, vol. 2009-01-2904, pp. 222–233, 2010.
- (41) R. Sutjiono, P. Tayal, K. Zhou, and P. Meckl, "Real-Time On-Board Indirect Light-Off Temperature Estimation as a Detection Technique of Diesel Oxidation Catalyst Effectiveness Level," *SAE Technical Paper*, vol. 2013-01-1517, 2013.
- (42) J. N. Chi and H. F. M. Dacosta, "Modeling and Control of a Urea-SCR Aftertreatment System," *SAE Technical Paper*, vol. 2005-01-0966, 2005.
- (43) M. Devarakonda, G. G. Parker, J. H. Johnson, and V. Strots, "Adequacy of Reduced Order Models for Model-Based Control in a Urea-SCR Aftertreatment System," *SAE Technical Paper*, vol. 2008-01-0617, 2008.
- (44) J. Cho, J. Lee, S. Kim, S. Bang, J. I. Chun, J. W. Kang, and S. Yoo, "A Development of Urea Solution Injection Quantity Decision Logic for SCR System," *SAE Technical Paper*, vol. 2013-01-1069, 2013.

- (45) A. Herman, M.-C. Wu, D. Cabush, and M. Shost, "Model Based Control of SCR Dosing and OBD Strategies with Feedback from NH<sub>3</sub> Sensors," *SAE Int. J. Fuels Lubr.* 2(1), vol. 2009-01-0911, pp. 375–385, 2009.
- (46) L. de Oliveira Costa and F. M. Rossin, "Optimizing the On Board Diagnostic System (OBD) to Monitor for Reduction of the SCR Catalyst Conversion Efficiency using the NO<sub>x</sub> Sensor," *SAE Technical Paper*, vol. 2010-36-0198, 2010.
- (47) B. Hollauf, B. BreitschŁdel, T. Sacher, and H. HŁlser, "Highest NO<sub>x</sub> Conversion in SCR Catalysts through Model Based Control," *SAE Technical Paper*, vol. 2011-26-0042, 2011.
- (48) M. A. Mallouh, M. Al-Marouf, B. Surgenor, and B. Peppley, "Effect of Control Strategy on the Performance of a Fuel Cell Hybrid Electric Auto Rickshaw," *SAE Technical Paper*, vol. 2011-01-1174, 2011.
- (49) T. L. McKinley and A. G. Alleyne, "A Switched, Controls-Oriented SCR Catalyst Model Using On-Line Eigenvalue Estimation," *SAE Technical Paper*, vol. 2009-01-1284, 2009.
- (50) A. Stevens, Y. Sun, J. Lian, M. Devarakonda, and G. Parker, "Optimal SCR Control Using Data-Driven Models," *SAE Technical Paper*, vol. 2013-01-1573, 2013.
- (51) B. L. Kumari, K. P. Raju, V. Chandan, R. S. Krishna, and V. Rao, "Application Of Extended Kalman Filter For A Free Falling Body Towards Earth," *International Journal of Advanced Computer Science and Applications*, vol. 2 No. 4, 2011.
- (52) D. Simon, *Optimal State Estimation: Kalman, H Infinity, and Nonlinear Approaches*. John Wiley and Sons, 2006.

- (53) X. Song, H. Surenahalli, J. Naber, J. Johnson, and G. Parker, “Experimental and Modeling Study of a Diesel Oxidation Catalyst (DOC) under Transient and CPF Active Regeneration Conditions,” *SAE Technical Paper*, vol. 2013-01-1046, 2013.
- (54) D. Chatterjee, T. Burkhardt, T. Rappe, A. G§thenke, and M. Weibel., “Numerical Simulation of DOC+DPF+SCR Systems: DOC Influence on SCR Performance,” *SAE Technical Paper*, vol. 2008-01-0867, 2008.
- (55) G. Koltsakis, O. Haralampous, C. Dardiotis, and Z. Samaras, “Performance of Catalyzed Particulate Filters without Upstream Oxidation Catalyst,” *SAE Technical Paper*, vol. 2005-01-0952, 2005.
- (56) J. C. C. Se H. Oh, “Transients of Monolithic Catalytic Converters: Response to step Changes in Feedstream Temperature as Related to Controlling Automobile Emissions,” *Industrial & Engineering Chemistry Product Research and Development*, vol. 21, pp. 29–37, 1982.
- (57) S. E. Voltz, C. R. Morgan, D. Liederman, and S. Jacob, “Kinetic Study of Carbon Monoxide and Propylene Oxidation on Platinum Catalysts,” *Eng. Chem. Prod. Res. Dev.*, vol. 12, 1973.
- (58) K. Premchand, J. Johnson, S. Yang, and A. Triana, “A Study of the Filtration and Oxidation Characteristics of a Diesel Oxidation Catalyst and a Catalyzed Particulate Filter,” *SAE Technical Paper*, vol. 2007-01-1123, 2007.
- (59) T. McKinley and A. Alleyne, “A Urea Decomposition Modeling Framework for SCR Systems,” *SAE Int. J. Fuels Lubr. 2(1)*, vol. 2009-01-1269, pp. 612–626, 2009.
- (60) S. Sluder, C. J. Storey, S. Lewis, and L. Lewis, “Low Temperature Urea Decomposition and SCR Performance,” *SAE Technical Paper*, vol. 2005-01-1858, 2005.

- (61) A. Grossale, I. Nova, E. Tronconi, and D. C. . M. Weibel, " $NH_3$   $NO$  /  $NO_2$  SCR for Diesel Exhausts Aftertreatment: Reactivity, Mechanism and Kinetic Modelling of Commercial Fe- and Cu-Promoted Zeolite Catalysts," *Topics in Catalysis*, vol. 52, pp. 1837–1841, 2009.
- (62) K. Narayanaswamy and Y. He, "Modeling of Copper-Zeolite and Iron-Zeolite Selective Catalytic Reduction (SCR) Catalysts at Steady State and Transient Conditions," *SAE Technical Paper*, vol. 2008-01-0615, 2008.
- (63) X. Song, J. Naber, J. Johnson, G. Parker, and J. Pihl, "A Modeling Study of SCR Reaction Kinetics from Reactor Experiments," *SAE Technical Paper*, vol. 2013-01-1576, 2013.
- (64) X. Song, J. Naber, J. Johnson, and G. Parker, "An Experimental and Modeling Study of Reaction Kinetics for a Cu-Zeolite SCR Catalyst Based on Engine Experiments," *SAE Technical Paper*, vol. 2013-01-1054, 2013.
- (65) I. Hamada, Y. Kato, N. Imada, and H. Kikkawa, "A Unique Titania-Based SCR  $NO_x$  Catalyst for Diesel Exhaust Emission Control," *SAE Technical Paper*, vol. 2005-01-1859, 2005.
- (66) K. Kamasamudram, N. Currier, T. Szailer, and A. Yezerets, "Why Cu- and Fe-Zeolite SCR Catalysts Behave Differently At Low Temperatures," *SAE Int. J. Fuels Lubr. 3(1)*, vol. 2010-01-1182, pp. 664–672, 2010.
- (67) E. T. Massimo Colombo, Isabella Nova, "A comparative study of the  $NH_3$ -SCR reactions over a Cu-zeolite and a Fe-zeolite catalyst," *Catalysis Today*, vol. 151, pp. 223–230, 19 June 2010.



- (68) M. Castagnola, J. Caserta, S. Chatterjee, and H. Chen, "Engine Performance of Cu- and Fe-Based SCR Emission Control Systems for Heavy Duty Diesel Applications," *SAE Technical Paper*, vol. 2011-01-1329, 2011.
- (69) I. Nova, C. Ciardelli, E. Tronconi, D. Chatterjee, and B. Bandl-Konrad, " $NH_3$  - SCR of NO over a V-based catalyst: Low-T redox kinetics with  $NH_3$  inhibition," *AIChE Journal*, vol. 52, p. 3222 to 3233, September 2006.
- (70) V. U. James C. Peyton Jones and M. Geveci, "Smart Sensing and Decomposition of  $NO_X$  and  $NH_3$  Components from Production  $NO_X$  Sensor Signals," *SAE Technical Paper*, vol. 2011-01-1157, 2011.

# APPENDIX A. $NH_3$ CONCENTRATION CALCULATION FROM DEF INJECTOR FLOWRATE

The SCR inlet  $NH_3$  cannot be measured directly measured due to partial decomposition of urea and the limitations of the mass spectrometer. Hence the SCR inlet  $NH_3$  concentrations are estimated using the DEF injector flow rate, urea properties and the exhaust flow rate. DEF is an aqueous solution consisting of 32.5% urea blended with 67.5% of deionized water by weight. The SCR inlet  $NH_3$  concentration is calculated using the equation A.1.

$$NH_3(ppm) = \frac{NH_3 \text{ molar flowrate (kmol/s)}}{\text{exhaust molar flowrate (kmol/s)}} \quad (A.1)$$

The molar flow rate of  $NH_3$  is calculated with equation A.2, using the DEF flow rate, density of DEF and the molecular weight of the urea.

$$NH_3 \text{ molar flowrate (kmol/s)} = \frac{\text{DEF mass flowrate (kg/s)}_{Act} * \rho_{DEF,Act} * 0.325 * 2}{MW_{Urea}} \quad (A.2)$$

The exhaust molar flow rate is calculated with equation A.2 using the exhaust mass flow rate, the exhaust gas density and the molecular weight of exhaust.

$$\text{Exhaust molar flowrate (kmol/s)} = \frac{\text{Exhaust mass flowrate (kg/s)}_{Act} * \rho_{Exh,Act}}{MW_{Exh,Act}} \quad (\text{A.3})$$

## APPENDIX B. $NO_X$ SENSOR MODEL

The  $NO_X$  sensor model was developed based on the model described in reference [70]. The model is an algebraic equation with sensitivities to  $NO$ ,  $NO_2$  and  $NH_3$  and is described using equation B.1

$$NO_X \text{ sensor} = a_0 + a_1 * NO + a_2 * NO_2 + a_3 * NH_3 \quad (B.1)$$

The parameters  $a_1$ ,  $a_2$  and  $a_3$  in the model are constants which define the sensitivity of  $NO_X$  sensor to  $NO$ ,  $NO_2$  and  $NH_3$  in the exhaust. To identify these parameters the data from the surrogate FTP test was used. Figure B.1 shows the fit of the  $NO_X$  sensor model to the experimental data. The first subplot shows the experimental SCR outlet concentrations of  $NO$ ,  $NO_2$  and  $NH_3$  in *ppm* at the SCR outlet against time along the x axis. The second subplot shows the experimentally measured  $NO_X$  sensor measurement and the simulated  $NO_X$  sensor measurement from the  $NO_X$  sensor model in equation B.1. The  $NO_X$  sensor model follows the experimental  $NO_X$  sensor measurement generally with less than  $\pm 20$  *ppm* error and a maximum error of  $\pm 116$  *ppm* at 40 *secs*. The constants  $a_0$ ,  $a_1$ ,  $a_2$  and  $a_3$  for the model are tabulated in table B.1. The magnitude of the parameter  $a_0$  was very small compared to the other parameters in equation B.1 and was set to zero.

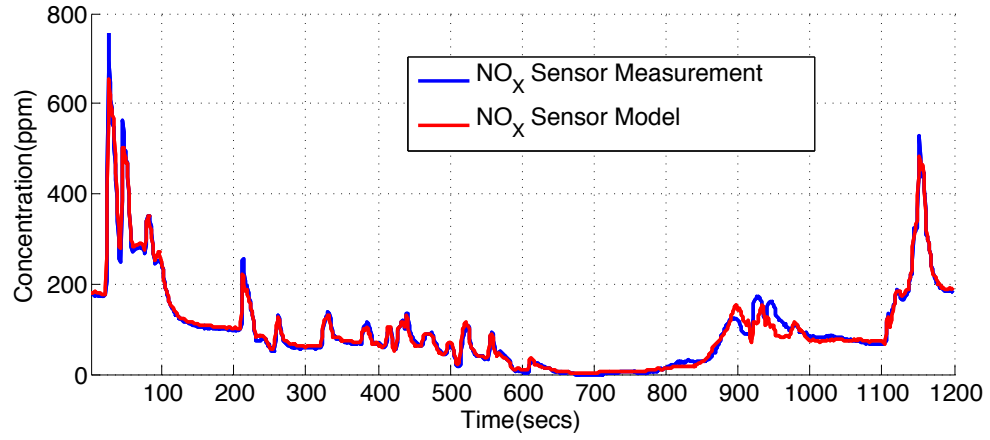
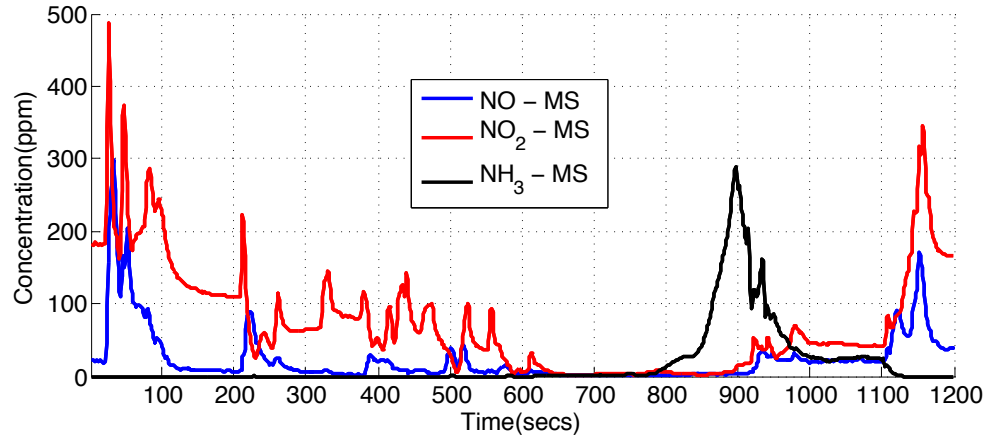


**Figure B.1.** Comparison of the  $NO_X$  sensor model with the  $NO_X$  sensor measurement

**Table B.1**  
Kinetic parameters used to simulate steady state conditions

Parameter	Value
$a_0$	0
$a_1$	1.23
$a_2$	0.85
$a_3$	0.49

# APPENDIX C. SCR JACOBIAN

## CALCULATIONS

One of the requirements for the EKF estimator is that the differential equations that describe the nonlinear system must be differentiable. The differentiability property of the system equations are used to calculate the state transition matrix for the EKF estimator. Hence calculating the Jacobian matrix for the system is an important calculation in the EKF estimator development. For the SCR EKF estimator developed in this study, the states for the estimator are the  $NH_3$  storage on site 1 and site 2 for each axial element. The differential equations 5.4 and 5.5 in Chapter 5 describe the mass balance for the  $NH_3$  storage states. The mass balance equations represented as functions for an SCR with 2 axial elements are tabulated in Table C.1.

**Table C.1**  
States and outputs of an SCR with 2 axial elements

<i>Inlet</i>	<i>Axial Element1</i> ( $x_1$ )	<i>Axial Element2</i> ( $x_2$ )
	$\theta_{1(x_1)}(NH_3 \text{ in}, NO \text{ in}, NO_2 \text{ in}, T, t)$	$\theta_{1(x_2)}(NH_3 \text{ } x_1, NO \text{ } x_1, NO_2 \text{ } x_1, T, t)$
	$\theta_{2(x_1)}(NH_3 \text{ in}, T, t)$	$\theta_{2(x_2)}(NH_3 \text{ } x_1, T, t)$
$NH_3 \text{ in}$	$NH_3 \text{ } (x_1)(NH_3 \text{ in}, \theta_{1(x_1)}, \theta_{2(x_1)}, T)$	$NH_3 \text{ } (x_2)(NH_3 \text{ } x_1, \theta_{1(x_2)}, \theta_{2(x_2)}, T)$
$NO \text{ in}$	$NO \text{ } (x_1)(NO \text{ in}, NO_2 \text{ in}, \theta_{1(x_1)}, T)$	$NO \text{ } (x_2)(NO \text{ } x_1, NO_2 \text{ } x_1, \theta_{1(x_2)}, T)$
$NO_2 \text{ in}$	$NO_2 \text{ } (x_1)(NO_2 \text{ in}, NO \text{ in}, \theta_{1(x_1)}, T)$	$NO_2 \text{ } (x_2)(NO \text{ } x_1, NO_2 \text{ } x_1, \theta_{1(x_2)}, T)$

The  $NH_3$  storage of site 1 in the first element is a function of the inlet  $NH_3$  ,  $NO$  and  $NO_2$  concentrations, temperature, and the  $NH_3$  storage from previous time. Similarly the  $NH_3$  storage of site 2 in the first element is a function of the inlet  $NH_3$  concentration, temperature and the  $NH_3$  storage from previous time. The  $NH_3$  concentration is a function of the inlet  $NH_3$  concentration,  $NH_3$  storage in site 1 and site 2 and temperature. The  $NO$  and  $NO_2$  concentrations are functions of inlet  $NO$  and  $NO_2$  concentrations,  $NH_3$  storage in site 1 and temperature. For the second axial element the  $NH_3$  storage and  $NO$  ,  $NO_2$  and  $NH_3$  concentrations are functions of the concentrations at axial element number 1 and the  $NH_3$  storage at axial element 2.

If we observe the functions for the  $NH_3$  storage states for element 1 and 2, the differential equations appear to be not differentiable with respect to states. This would mean that  $NH_3$  storage for the second element would be unobservable with respect to  $NH_3$  storage in element 1. However the observability can be established by using the output equations for  $NH_3$  ,  $NO$  and  $NO_2$  . For the second axial element the  $NH_3$  storage for site 1 and 2 can be made differentiable by using chain rule and exploiting the relationship between storage and  $NH_3$  ,  $NO$  and  $NO_2$  concentrations as shown from equation C.1 to C.4.

$$\frac{\partial \theta_{1(x_2)}}{\partial \theta_{1(x_1)}} = \frac{\partial \theta_{1(x_2)}}{\partial NH_3(x_1)} * \frac{\partial NH_3(x_1)}{\partial \theta_{1(x_1)}} + \frac{\partial \theta_{1(x_2)}}{\partial NO(x_1)} * \frac{\partial NO(x_1)}{\partial \theta_{1(x_1)}} + \frac{\partial \theta_{1(x_2)}}{\partial NO_2(x_1)} * \frac{\partial NO_2(x_1)}{\partial \theta_{1(x_1)}} \quad (C.1)$$

$$\frac{\partial \theta_{1(x_2)}}{\partial \theta_{2(x_1)}} = \frac{\partial \theta_{1(x_2)}}{\partial NH_3(x_1)} * \frac{\partial NH_3(x_1)}{\partial \theta_{2(x_1)}} \quad (C.2)$$

$$\frac{\partial \theta_{2(x_2)}}{\partial \theta_{2(x_1)}} = \frac{\partial \theta_{2(x_2)}}{\partial N H_3(x_1)} * \frac{\partial N H_3(x_1)}{\partial \theta_{2(x_1)}} \quad (\text{C.3})$$

$$\frac{\partial \theta_{2(x_2)}}{\partial \theta_{1(x_1)}} = \frac{\partial \theta_{2(x_2)}}{\partial N H_3(x_1)} * \frac{\partial N H_3(x_1)}{\partial \theta_{1(x_1)}} \quad (\text{C.4})$$